

Growth and electronic structure of single-layered transition metal dichalcogenides

Maciej Dendzik

Department of Physics and Astronomy
Aarhus University, Denmark

Ph.D. Thesis

September, 2016

Abstract

The discovery of graphene has opened a novel research direction focused on the properties of 2D materials. Transition metal dichalcogenides (TMDCs) were quickly identified as important materials due to the great variety of electronic properties that they manifest – properties that are markedly different from graphene’s. For example, semiconducting TMDCs undergo an indirect-direct band gap transition when thinned to a single layer (SL); this results in greatly enhanced photoluminescence, making those materials attractive for applications in optoelectronics. Furthermore, metallic TMDCs can host charge density wave (CDW) and superconducting (SC) phases, which are fundamental for understanding condensed matter physics. Nevertheless, the synthesis of high-quality SL TMDCs still remains challenging.

In this thesis we present epitaxial growth methods developed in our group to obtain large-area, high-quality SL TMDCs. We demonstrate the synthesis of SL MoS₂, WS₂ and TaS₂ on Au(111), Ag(111) and graphene on SiC. The morphology and crystal structure of the synthesized materials is characterized by scanning tunneling microscopy (STM) and low-energy electron diffraction (LEED). The electronic structure of SL TMDCs is directly studied with angle-resolved photoemission spectroscopy (ARPES) and x-ray photoelectron spectroscopy (XPS) techniques. Experimental results are compared with density-functional theory calculations (DFT), both for a free-standing layer and for a layer adsorbed on a metallic substrate.

The electron energy dispersion of semiconducting MoS₂ synthesized on Au(111) is found to be affected by the substrate interaction. The bands in the center of surface Brillouin zone (SBZ) are found to be strongly hybridized with Au *d*-bands. Nevertheless, the dispersion around corners of the SBZ remains largely unaffected and exhibits a sizeable spin-splitting. We find that in WS₂ substitution of Mo with heavier W atoms leads to enlarging of this effect and simultaneously reduces the hole effective mass.

We further study substrate effects by investigations of SL TMDCs grown on graphene/SiC and on Ag(111). We find only a weak interaction between SL MoS₂ and graphene, which leads to a quasi-freestanding band structure, but also to the coexistence of multiple rotational domains. Measurements of SL WS₂ on Ag(111), on the other hand, reveals formation of interesting in-gap states which make WS₂ metallic.

Low-temperature STM studies reveal suppression of CDWs in SL TaS₂/Au(111). We attribute this effect to substantial doping originating from the substrate. Recent theoretical calculations suggest that doping might be caused by band hybridization, rather than charge transfer through the interface.

Last but not least, we study the effect of the well-known herringbone reconstruction on the electronic structure of Au(111). We find the Fermi contours to be strongly modified, but only for measurements taken in higher order SBZs. We propose a simple structural model which explains the observations.

Resumé

Opdagelsen af grafen har åbnet en ny forskningsretning, som fokuserer på 2D materialers egenskaber. Overgangsmetal dichalcogenider (TMDC'er) blev hurtigt identificeret som værende vigtige materialer takket være den bredde vifte af elektroniske egenskaber, som de kan udvise – egenskaber som vel at mærke afviger markant fra grafens. Eksempelvis undergår halvledende TMDC'er en overgang fra et indirekte båndgab til et direkte båndgab, når deres tykkelse mindskes til et enkelt lag (SL). Dette medfører kraftigt forøget fotoluminescens, hvilket gør disse materialer meget attraktive til brug i optoelektronik. Desuden kan metalliske TMDC'er have ladningsdensitet bølge (CDW) og superledende (SC) faser, som er af fundamental vigtighed for forståelsen af faststof fysik. Det til trods er syntesen af højkvalitets SL TMDC'er stadig en væsentlig udfordring i feltet.

I denne afhandling præsenterer vi epitaksial syntese metoder, som vi har udviklet med henblik på at opnå store flader af højkvalitets SL TMDC'er. Vi fremviser synteser af SL MoS₂, WS₂ og TaS₂ på substrater af Au(111), Ag(111) og grafen på SiC. Morfologien og krystalstrukturen af de fremstillede materialer karakteriseres ved brug af scanning tunnelering mikroskopi (STM) og lavenergi elektron diffraktion (LEED). Den elektroniske struktur af SL TMDC'er bliver undersøgt direkte ved hjælp af vinkelopløst fotoemissionsspektroskopi (ARPES) og røntgen fotoelektron spektroskopi (XPS) eksperimenter. Eksperimentelt opnåede resultater sammenlignes med densitetsfunktionalteori (DFT) beregninger for både fritstående lag og materialer adsorberet på et metallisk substrat.

Det vises, at den elektroniske energidispersion af halvledende MoS₂ syntetiseret på Au(111) påvirkes af substratinteraktionen. Båndene i den centrale del af overflade Brillouin zonen (SBZ) hybridiserer kraftigt med *d*-bånd fra Au substratet. Alligevel forbliver energidispersionen omkring hjørnerne af SBZ'en praktisk taget uforandret og udviser en betragtelig spinsplitting. Vi har desuden eftervist, at WS₂, hvor Mo erstattes med W atomer, udviser denne effekt i en forstærket grad og samtidig har en reduceret effektiv hul masse.

Vi har studeret substrateffekter i dybden ved at undersøge SL TMDC'er syntetiseret på grafen/SiC og på Ag(111). Vi ser kun en svag interaktion imellem SL MoS₂ og grafen, hvilket medfører en kvasi-fritstående båndstruktur samt sameksistensen af flere rotationelle domæner. Målinger af SL WS₂ på Ag(111) afslører imidlertid dannelsen af interessante tilstande i båndgabets, som gør WS₂ metallisk.

Lavtemperatur STM studier afslører en undertrykkelse af CDW'er i SL TaS₂/Au(111). Vi tilskriver denne effekt til betydelig doping med ophav i substratet. Teoretiske beregninger har for nyligt indikeret, at doping kan være forårsaget af båndhybridisering fremfor en ladningsoverførsel igennem grænsefladen.

Slutteligt studerer vi effekten af den velkendte sildebensrekonstruktion på den elektroniske struktur af Au(111). Vi ser, at Fermi konturerne modificeres kraftigt forudsat, at målingerne foretages i højere ordens SBZ'er. Vi foreslår en simpel struktural model, som forklarer disse observationer.

Preface

The research presented in this dissertation was conducted from November 2013 to September 2016. The official enrolment into the PhD program at the Aarhus Graduate School of Science was accepted from October 2013. The work was performed under the supervision of Professor Philip Hofmann, Department of Physics and Astronomy, Interdisciplinary Nanoscience Centre, Aarhus University, 8000 Aarhus C, Denmark.

This thesis has been submitted to the Faculty of Science and Technology at Aarhus University in order to fulfill the requirements for obtaining a Ph.D. degree in Physics. The majority of the work has been carried out at the SGM3 beamline for angle-resolved photoemission on ASTRID2 at the Institute for Storage Ring Facilities in Aarhus (ISA). The initial sample preparation was performed in the group headed by Professor Jeppe Vang Lauritsen (Interdisciplinary Nanoscience Centre, Aarhus University). In addition, I spent a considerable amount of time at the international synchrotron facilities, in particular the i3 beamline at Max-Lab.

Acknowledgments

During the past three years, I had a great pleasure and a privilege to work with many amazing people, who influenced me not only on the professional, but also on the personal level. I am deeply grateful to all the people mentioned below.

I would like to thank my supervisor Philip Hofmann for giving me the opportunity to join his group, for guidance, excellent scientific discussions and freedom to pursue my ideas. I really appreciate that Philip's office was always open for me.

I am thankful to all the past and present members of the Philip's group. Special thanks to Marco Bianchi, who introduced me to the UHV world and has been a great mentor throughout those years. I am grateful to: Charlotte Sanders for all great discussions we had, not only on the scientific matter; Jill Miwa for her positive attitude and for being the nicest person I have ever met; Antonija Grubisic Čabo for her sense of humor and many laughs, both inside and outside the lab; Fabian Arnold for being a great roommate during the conferences and external beamtimes; Arlette Sohanfo Ngankeu for being always ready to help, even in the middle of the night; Søren Ulstrup for sharing with me his ARPES know-how; Matteo Michiardi for great fun at beamtimes and for being a good friend.

I would like to thank all the people I had a pleasure to collaborate with: Albert Bruix Fusté, Bjørk Hammer, Alexander Khajetoorians, Andreas Eich, Federico Mazzola, Justin Wells, Simon Cooil, Signe Grønberg, Jeppe Lauritsen, Jonathon Riley, Liam Collins-McIntyre, Lewis Bawden, Philip King, Craig Polley, Mats Leandersson and Balasubramanian Thiagarajan.

I am indebted to all the beamline scientists working at ISA for their support and for giving us the best possible working conditions.

I would like to express my sincere gratitude to my parents Zbyszek and Dorota, my girlfriend Ania, and my close friends Mariusz and Maciek for their constant personal support and reminding me that science is not the only thing in the world.

Maciej Dendzik

30.09.2016

Aarhus, Denmark



List of publications

Publications relevant for the thesis

18. M. Dendzik, M. Bianchi, M. Michiardi, C. E. Sanders and P. Hofmann, *Reconstruction-induced trefoil knot Fermi contour of Au(111)*, submitted.
17. A. Bruix, J. A. Miwa, N. Hauptmann, D. Wegner, S. Ulstrup, S. S. Grønberg, C. E. Sanders, M. Dendzik, A. G. Čabo, M. Bianchi, J. V. Lauritsen, A. A. Khajetoorians, B. Hammer, and P. Hofmann, *Single-layer MoS₂ on Au(111): band gap renormalization and substrate interaction*, **Physical Review B**, 93, 165422, (2016).
16. C. E. Sanders, M. Dendzik, A. S. Ngankeu, A. Eich, A. Bruix, M. Bianchi, J. A. Miwa, B. Hammer, A. A. Khajetoorians, and P. Hofmann, *Crystalline and electronic structure of single-layer TaS₂*, **Physical Review B (Rapid Communications)**, 94, 081404, (2016).
15. M. Dendzik, M. Michiardi, C. Sanders, M. Bianchi, J. A. Miwa, S. S. Grønberg, J. V. Lauritsen, A. Bruix, B. Hammer, and P. Hofmann, *Growth and electronic structure of epitaxial single-layer WS₂ on Au(111)*, **Physical Review B**, 92, 245442, (2015).
14. S. S. Grønberg, S. Ulstrup, M. Bianchi, M. Dendzik, C. E. Sanders, J. V. Lauritsen, P. Hofmann, and J. A. Miwa, *Synthesis of Epitaxial Single-Layer MoS₂ on Au(111)*, **Langmuir**, 31, 9700, (2015).
13. J. A. Miwa, M. Dendzik, S. S. Grønberg, M. Bianchi, J. V. Lauritsen, P. Hofmann, and S. Ulstrup, *Van der Waals Epitaxy of Two-Dimensional MoS₂-Graphene Heterostructures in Ultrahigh Vacuum*, **ACS Nano**, 9, 6502, (2015).
12. J. A. Miwa, S. Ulstrup, S. G. Sørensen, M. Dendzik, A. G. Čabo, M. Bianchi, J. V. Lauritsen, and P. Hofmann, *Electronic Structure of Epitaxial Single-Layer MoS₂*, **Physical Review Letters**, 114, 046802, (2015).

Other publications

11. J. Jørgensen, A. G. Čabo, R. Balog, L. Kyhl, M. Groves, A. Cassidy, M. Bianchi, M. Dendzik, M. Arman, L. Lammich, J. Pascual, J. Knudsen, B. Hammer, P. Hofmann and L. Hornekaer, *Symmetry Driven Band Gap Engineering in Hydrogen Functionalized Graphene*, submitted.
10. S. Ulstrup, A. G. Čabo, D. Biswas, J. M. Riley, M. Dendzik, C. E. Sanders, M. Bianchi, C. Cacho, D. Matselyukh, R. T. Chapman, E. Springate, P. D. C. King, J. A. Miwa and P. Hofmann, *Spin and Valley Control of Free Carriers in Single-Layer WS₂*, submitted.

9. A. Eich, N. Rollfing, F. Arnold, C. E. Sanders, P. R. Ewen, M. Bianchi, M. Dendzik, M. Michiardi, J.-L. Mi, M. Bremholm, D. Wegner, P. Hofmann and A. A. Khajetoorians, *Absence of superconductivity in ultrathin layers of FeSe synthesised on a topological insulator*, **Physical Review B**, in press.
8. S. Ulstrup, A. G. Čabo, J. A. Miwa, J. M. Riley, S. S. Grønborg, J. C. Johannsen, C. Cacho, O. Alexander, R. T. Chapman, E. Springate, M. Bianchi, M. Dendzik, J. V. Lauritsen, P. D. C. King, and P. Hofmann, *Ultrafast Band Structure Control of a Two-Dimensional Heterostructure*, **ACS Nano**, 10, 6315, (2016).
7. L. Koefoed, M. Kongsfelt, S. Ulstrup, A. G. Čabo, A. Cassidy, P. R. Whelan, M. Bianchi, M. Dendzik, F. Pizzocchero, B. Jørgensen, P. Bøggild, L. Hornekær, P. Hofmann, S. U. Pedersen, and K. Daasbjerg, *Facile electrochemical transfer of large-area single crystal epitaxial graphene from Ir(111)*, **Journal of Physics D: Applied Physics**, 48, 115306, (2015).
6. M. Michiardi, M. Bianchi, M. Dendzik, J. A. Miwa, M. Hoesch, T. K. Kim, P. Matzen, J. Mi, M. Bremholm, B. B. Iversen, and P. Hofmann, *Strongly anisotropic spin-orbit splitting in a two-dimensional electron gas*, **Physical Review B**, 91, 035445, (2015).
5. J. M. Riley, F. Mazzola, M. Dendzik, M. Michiardi, T. Takayama, L. Bawden, C. Granerød, M. Leandersson, T. Balasubramanian, M. Hoesch, T. K. Kim, H. Takagi, W. Meevasana, P. Hofmann, M. S. Bahramy, J. W. Wells, and P. D. C. King, *Direct observation of spin-polarized bulk bands in an inversion-symmetric semiconductor*, **Nature Physics**, 10, 835, (2014).
4. M. Dendzik, A. Kulik, F. Benedetti, P. E. Marszalek, and G. Dietler, *A single-molecule stretching method for lateral and normal AFM lever calibration*, **Nanotechnology**, 24, 365703, (2013).
3. J. Nizioł, M. Dendzik, M. Sitarz, E. Hebda, J. Pielichowski, J. Łojewska, A. Rogulska, and M. Bakasse, *Thermal annealing effect on physical properties of DNA-CTMA thin films*, **Optical Materials**, 36, 36, (2013).
2. X.-G. Zhu, M. Stensgaard, L. Barreto, W. S. e. Silva, S. Ulstrup, M. Michiardi, M. Bianchi, M. Dendzik, and P. Hofmann, *Three Dirac points on the (110) surface of the topological insulator $Bi_{1-x}Sb_x$* , **New Journal of Physics**, 15, 103011, (2013).
1. M. Dendzik, A. Terfort, and P. Cyganik, *Odd-Even Effect in the Polymorphism of Self-Assembled Monolayers of Biphenyl-Substituted Alkaneselenolates on Au(111)*, **The Journal of Physical Chemistry C**, 116, 19535, (2012).

Contents

Abstract	3
Resumé	5
Preface	7
Acknowledgments	9
List of publications	11
Contents	14
1 Introduction	15
1.1 2D materials	15
1.2 Bulk transition metal dichalcogenides	16
1.3 Molybdenum and tungsten dichalcogenides	17
1.4 Tantalum dichalcogenides	21
1.5 Thesis outline	22
2 Experimental techniques	23
2.1 Angle-resolved photoemission spectroscopy	23
2.1.1 Photoemission	23
2.1.2 Spectral function	24
2.1.3 Photoemission from core-levels	26
2.1.4 Acquisition and analysis of ARPES spectra	29
2.2 Experimental setup	31
2.2.1 ASTRID2 and SGM3 beamline	31
2.2.2 End station	32
2.3 Structural investigation techniques	33
2.3.1 Scanning-tunneling microscopy	33
2.3.2 Low-energy electron diffraction	35
3 Surface reconstruction effects on the Au substrate	37
3.1 Herringbone reconstruction of Au(111)	37
3.2 Trefoil knot Fermi contour	38
3.3 Oblique unit cell model of the surface	44
4 Synthesis of single-layered transition metal dichalcogenides	51
4.1 General growth procedure	51
4.2 MoS ₂ on Au(111)	52
4.3 MoS ₂ on graphene/SiC	57
4.4 WS ₂ on Au(111) and Ag(111)	59
4.5 TaS ₂ on Au(111)	65

5	Electronic structure of single-layered transition metal dichalcogenides	69
5.1	SL MoS ₂ on Au(111)	69
5.1.1	ARPES characterization	69
5.1.2	DFT calculations	74
5.2	MoS ₂ -graphene heterostructure	79
5.3	SL WS ₂	83
5.3.1	Semiconducting SL WS ₂ on Au(111)	83
5.3.2	Metallic SL WS ₂ on Ag(111)	89
5.4	Suppression of CDW in SL TaS ₂ on Au(111)	92
6	Summary	97
	Bibliography	99

Chapter 1

Introduction

The aim of this introductory chapter is to establish a general context for the work presented in the thesis. Firstly, the historical background of research in the field of 2D materials is presented. Secondly, the group of transition metal dichalcogenides (TMDCs) is briefly overviewed. Finally, the ending sections of this chapter are devoted to the structure and properties of semiconducting and metallic TMDCs.

1.1 2D materials

For many years, it was believed that 2D crystalline materials cannot exist at finite temperatures due to the divergence of fluctuations, destroying the long-range order. This viewpoint was supported by great authorities in physics, such as Peierls [1], Landau [2] and Mermin [3], which paradoxically slowed down research progress in the field. It was much later realized that those theoretical predictions strictly apply only for infinite crystals. In addition, a rippled structure can permit stability in 2D materials [4, 5].

Today, the most famous 2D material is single-layered graphite, called graphene. The first theoretical calculations of graphene's electronic structure dates back to 1947 [6]. The signatures of graphene flakes were identified in low-energy electron diffraction (LEED) and Auger spectroscopy experiments on single crystals of platinum [7, 8] and nickel [9] two decades later. Initially, graphene was treated merely as an unwanted contamination originating from the carbon segregation during crystal cleaning procedures. The true advent of graphene research took place in 2004, when Novoselov and Geim used scotch tape to mechanically exfoliate single layers from bulk graphite crystals. Despite initial rejection, their work was eventually published [10] and led to a huge scientific interest. Graphene turned out to be a fertile ground for studying exotic physical phenomena such as a wide variety of quantum Hall effects (QHEs) [11–14] and the Klein paradox [15–18]. Moreover, investigations of graphene have been motivated by application-desired properties, such as extraordinary mechanical strength and electrical conductivity [19, 20]. Highlighting the importance of Novoselov and Geim's work, the Nobel Prize in Physics was awarded to them in 2010 [21], just six years after their initial publication.

Soon after the first exfoliation of graphene, it was realized that other layered materials can be isolated in a similar way. NbSe₂ and MoS₂ were among the first materials, apart from graphene, to be isolated in the single-layer limit [22]. Those materials are members of a large group of compounds, called transition metal dichalcogenides (TMDCs), which exhibit a wide range of electronic properties [23]. This means that with a substitution of a transition metal in TMDC, one can engineer the band structure to some extent. Some of the properties of TMDCs are complementary to graphene's. For example, it is challenging to open a sizable

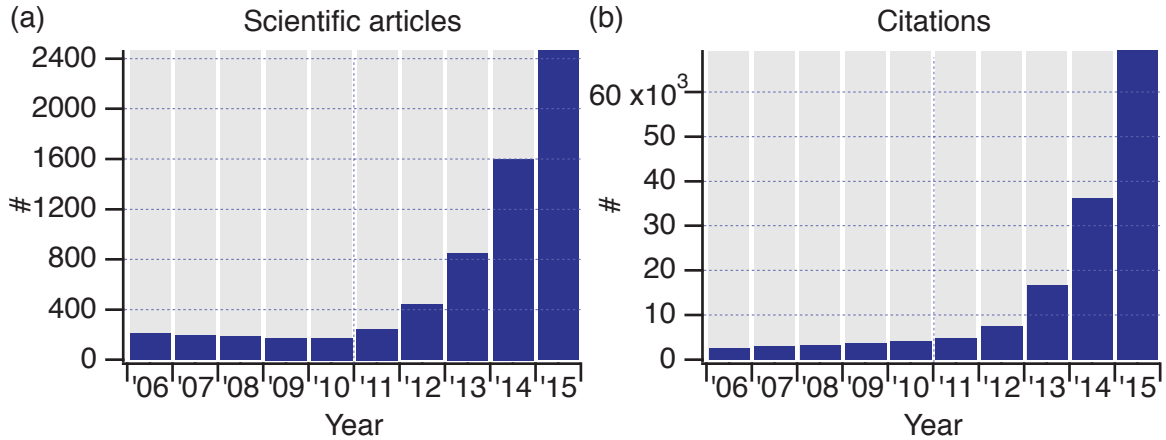


Figure 1.1: (a) The number of scientific publications issued over the last decade containing “MoS₂” in the topic. (b) Number of citations of the articles in (a) per year. Search done using the Thomson Reuters ISI Web of Knowledge database [38].

bandgap in graphene [24, 25], while SL MoS₂ is an intrinsic semiconductor [26]. Furthermore, the spin-orbit coupling (SOC) is negligible in graphene, as it is composed exclusively of light carbon atoms, but in case of a heavy-atom TMDC like WS₂, the large SOC leads to a significant splitting of both valence and conduction bands, making it an attractive graphene-analog for use in spintronics [27].

Large scientific interest in studying 2D TMDCs was sparked in 2010 with the observation of an indirect-direct band gap transition that occurs when a MoS₂ crystal is thinned to a SL [26, 28]. Since then, the number of articles published in the field of TMDCs has been almost doubling every year, as can be seen in Fig. 1.1. Probably the most studied SL TMDCs, to date, are molybdenum dichalcogenides, which are attractive materials for electronic applications such as transistors [29, 30], diodes [31], photoemitting devices [32], solar cells [33] and memristors [34]. In case of the tungsten dichalcogenides, much stronger spin-orbit coupling is expected than in the case of the Mo-based analogues, and the properties just enumerated should thus be more stable at room temperature [27, 35, 36]. Finally, metallic TMDCs have recently received considerable attention due to the observation of both superconductivity (SC) and charge density wave (CDW) in SL NbSe₂ [37].

Many proposed approaches to characterizing the electronic properties of SL TMDCs, as well as many potential applications, require large area and high quality samples. The present work introduces methods for the epitaxial growth of MoS₂, WS₂ and TaS₂ on Au(111), Ag(111) and graphene/SiC. The growth and structure are studied by scanning tunneling microscopy (STM), low energy electron diffraction (LEED) and core-level spectroscopy. The high quality of SL TMDCs obtained in this procedure permits an investigation of the electronic structure by angle-resolved photoemission spectroscopy (ARPES). Obtained results suggest that similar growth methods can also be applied for the synthesis of other SL TMDCs.

1.2 Bulk transition metal dichalcogenides

The properties of 2D TMDCs are inherited from their 3D parents to a large extent, so it is insightful to start a discussion with an overview of the well-known bulk TMDCs. An excellent review covering this topic can be found in Ref. [23]. There exist about 100 TMDCs, out of which

around 40 have a layered structure (see Fig. 1.2). Layered TMDCs consist of a layer of transition metal atoms (M) sandwiched between two layers of chalcogens (X), forming a MX_2 compound. While the intralayer M-X bonds are predominantly covalent, the interactions between MX_2 sandwiches are only of the van der Waals type, which makes them easy to cleave and makes intercalation easy between adjacent layers.

The metal atoms provide four electrons for the bonds with the two chalcogens, which leads to oxidation states of +4 for M and -2 for X. The lone pair of X electrons terminates the surface, making MX_2 stable and chemically rather inert. The coordination of the transition metal inside MX_2 can be either trigonal prismatic (H) or octahedral (T). In bulk, different stacking orders can be realized; the most common ones are presented in the inset of Fig. 1.2. Usually, the most stable polymorph is found to consist of two 180° rotated layers of the trigonal prismatic MX_2 , and this is commonly called the 2H phase (digit indicates the number of MX_2 layers inside a unit cell). Apart from the common AB stacking sequence present in the 2H phase, also ABC order can be realized (3R phase). Finally, some of the TMDCs can crystallize in metastable phases, in which the coordination of X atom is different than trigonal prismatic. These include both the octahedral (1T) and the distorted octahedral (1T') phases.

The plethora of transition metals forming layered TMDCs, combined with their polymorphism, results in a wide range of possible electronic properties. While most of layered TMDCs are semiconductors in the 2H phase (groups 4,6,7,9,10), group 5 dichalcogenides are metals hosting SC and CDW states [39, 40]. Semimetallic MoTe_2 and WTe_2 are quite interesting, as those materials are predicted to be previously over-looked type II Weyl semimetals [41, 42]. Furthermore the largest to date non-saturating magnetoresistance was observed for WTe_2 crystals [43, 44].

Molybdenum and tungsten dichalcogenides have been extensively studied, and used in industrial applications, such as high-temperature dry lubricants, and catalysis. In the metastable 1T phase those materials are metallic. However, 2H crystals are indirect band gap semiconductors with a gap of ca. 1.3 eV. Drastic changes in the electronic properties can be achieved by extracting a single layer of these materials. This results in a semiconductor with a direct band gap in the visible-light spectrum, having promising applications for optoelectronics.

Prototypical systems of semiconducting (MoS_2 and WS_2), as well as metallic (TaS_2), materials has been chosen for the studies described in this thesis. The following sections are devoted to the theoretical predictions describing those materials in a single layer limit. For the sake of brevity, the 1H prefix is dropped, except where it has been necessary to contrast that structural phase with others (e.g., 1T or 1T').

1.3 Molybdenum and tungsten dichalcogenides

SL MoS_2 forms a honeycomb lattice with the lattice constant of ca. 3.15 \AA and the thickness of 6.5 \AA . Although the interaction between the SLs is quite weak in bulk, interlayer coupling has an influence on the electronic structure. This can be seen in Fig. 1.3. For the single layer case, the valence band maximum (VBM) and conduction band minimum (CBM) are situated at \bar{K} points of the hexagonal surface Brillouin zone (SBZ). When the second layer is added on top, extended nature of Mo d_z^2 orbitals results in a splitting of the bands at $\bar{\Gamma}$. Consequently, the VBM shifts to $\bar{\Gamma}$, making a double layer an indirect band gap semiconductor. Addition of further layers results in the shift of CBM into the middle point of the $\bar{\Gamma}$ - \bar{K} line, due to interactions of S p_z and Mo d_z^2 orbitals. Change of the band gap character has a tremendous effect on the

Figure 1.2 shows a periodic table where elements forming layered transition metal dichalcogenides (TMDCs) are highlighted. The legend indicates that M represents a transition metal and X represents a chalcogen. The inset diagrams illustrate the coordination environments: trigonal prismatic (H) and octahedral (T), and three common polymorphs: 2H, 1T, and 3R. The periodic table highlights elements as follows: Ti, V, Cr, Mn, Fe, Co, Ni, Cu, Zn, Ga, Ge, As, Se, Br, Kr, Rb, Sr, Y, Zr, Nb, Mo, Tc, Ru, Rh, Pd, Ag, Cd, In, Sn, Sb, Te, I, Xe, Cs, Ba, La-Lu, Hf, Ta, W, Re, Os, Ir, Pt, Au, Hg, Tl, Pb, Bi, Po, At, Rn, Fr, Ra, Ac-Lr, Rf, Db, Sg, Bh, Hs, Mt, Ds, Rg, Cn, Uut, Fl, Uup, Lv, Uus, Uuo. Chalcogens (S, Se, Te) are highlighted in yellow, and transition metals are highlighted in various other colors.

Figure 1.2: Periodic table with elements forming layered TMDCs indicated by colors. Chalcogens are marked with yellow, while transition metals with the other colors. The inset shows two types of coordination: trigonal prismatic (H) and octahedral (T), together with three most common polymorphs. Corresponding unit cells are marked with lines. After [23].

photoluminescence (PL). Quantum yield of the MoS₂ photoluminescence was found to be two (four) orders of magnitude larger for a single layer than for a double layer (bulk) [28].

Since all the interesting electronic transport effects are governed by the electron dispersion close to the Fermi level, it is insightful to study the band dispersion around VBM and CBM in detail. At \bar{K} , the main orbital contribution to the overall dispersion originates from Mo *d* orbitals. In a simple two-band model, which preserves the C_{3h} symmetry of the system, basis functions for conduction ψ_c and valence ψ_v bands are given by:

$$|\psi_c\rangle = |d_{z^2}\rangle, \quad |\psi_v^\tau\rangle = \frac{1}{\sqrt{2}}(|d_{x^2-y^2}\rangle + i\tau |d_{xy}\rangle), \quad (1.1)$$

where $\tau = \pm 1$ is the valley index. The valence band wave functions $|\psi_v^\pm\rangle$ are related to each other with the time-reversal operation. To first order in \mathbf{k} (measured from $\pm\bar{K}$) and without SOC, the $\mathbf{k} \cdot \mathbf{p}$ two-band Hamiltonian conserving the symmetry of the system is given by the massive Dirac fermion model [45]:

$$H = at(\tau k_x \sigma_x + k_y \sigma_y) + \frac{\Delta}{2} \sigma_z, \quad (1.2)$$

where a is the lattice constant, t is the hopping integral and σ denotes Pauli matrices in the basis given by Eq. 1.1. The τ dependence in the Hamiltonian leads to the valley contrast in the orbital magnetic moment m and the Berry curvature Ω [46], which enables the realization of valley polarization using electromagnetic fields. For instance, an in-plane electric field gives rise to the valley Hall effect [47], in analogy to the spin Hall effect. The valley dependence in m enables coupling of the valley pseudo-spin to the magnetic field, which enables the control and detection of valley polarization. This, theoretically, permits the use of the valley index in information processing technology [48]. Furthermore, the valley contrasting m is a source of the valley-dependent selection rules for circularly polarized light, which enables selective population of a given valley by choice of light polarization (Fig. 1.4(c)). Large k -space separation between the valleys provides a protection from intervalley scattering and results in a conservation of the valley index during the radiative recombination process [49]. It should be noted that these

properties are intrinsic solely to the lack of inversion symmetry; graphene with the staggered sublattices also exhibits valley physics [50].

An important difference between SL MoS₂ and graphene is a large SOC in the former. SOC leads to the spin-split bands, as presented in Fig. 1.4(a)-(b). This is a consequence of the inversion symmetry breaking, in resemblance to the Dresselhaus spin-splitting [51]. In a simple picture, electrons have a higher density of states close to the Mo atoms, which induces a dipole moment within the unit cell. Due to the mirror symmetry in the metal plane, the dipole needs to lie in this plane and induce spin-polarization in the normal direction. The time-reversal symmetry requires the opposite spin-polarization for \bar{K} and \bar{K}' . The SOC contribution can be approximated as the intra-atomic $\mathbf{L} \cdot \mathbf{S}$ coupling, which translate into H_{SOC} Hamiltonian [45]:

$$H_{\text{SOC}} = \lambda\tau\frac{1}{2}(\sigma_z - \mathbb{1})s_z, \quad (1.3)$$

where 2λ is the valence band splitting at \bar{K} and s_z is the Pauli spin matrix. This means that the spin configuration is locked to the given valley. Consequently, a spin can be selectively excited using the valley optical rules. This protects both spin and valley polarizations, as any spin-flipping transition requires flipping spin and valley simultaneously. Indeed, PL measurements indicate long lifetimes (ps range) of valley excitons [52]. The presented system seems to be ideal to study the internal quantum degrees of freedom (qDoF) such as spin, valley pseudospin and their interactions.

Although Eq. 1.3 suggests that the spin-splitting is induced only in the VB, density functional theorem calculations (DFT) suggest a small splitting in the CB as well [53]. This effect can be understood as a competition between the first-order contribution from chalcogen atom orbitals and the second-order contribution from Mo orbitals [53]. The asymmetry of VB and CB spin-splittings enables excitation of a given spin within the valley by choosing appropriate photon energy (see 1.4(c)). Further corrections to the modeled band structure reveal anisotropy of the VBM and CBM, giving rise to the characteristic trigonal warping of the constant energy contours [54]. This effect is not directly connected to the SOC, as it is also present in graphene [55].

The fundamental physics for WS₂ (as well as for WSe₂ and MoSe₂) is very similar to that of MoS₂. However, much larger overall effects are predicted in the case of tungsten dichalcogenides, as SOC is $\propto Z^4$. The spin-split energy difference of VBM (CBM) is as high as 420 meV (32 meV) for WS₂ in comparison to 145 meV(3 meV) for MoS₂, as shown in Figs. 1.4(a)-(b). A notable difference between the two materials is expected around the conduction band minimum [56]. As previously mentioned, this effect can be modeled as the competition of two effects, which results in the same spin orientation for VBM and CBM in MoS₂ and the opposite in WS₂. Also, in MoS₂ the spin-split CBM has a lower effective mass than its spin-partner, which results in band crossings around \bar{K} . This is not the case for WS₂, where bands stay clearly separated, as shown in the insets of Fig. 1.4. Naively, the strong spin-orbit splitting of the bands can also be expected to result in an increased band curvature near the top of the valence band and hence to the reduced effective mass; and indeed, WS₂ is predicted to be the best material among all of the TMDCs for a transistor channel, due to its low effective hole mass [53, 57, 58]. Finally, larger spin-splitting should make the spin physics effects more stable at room temperature [27, 35, 36], which is important for future industrial applications.

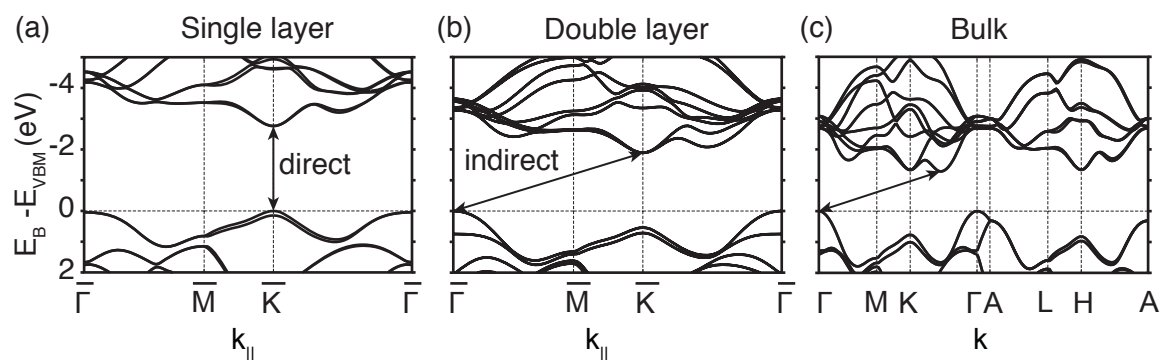


Figure 1.3: DFT calculations illustrating the evolution of MoS₂ band structure for a single layer (a), a double layer (b) and bulk. After [59].

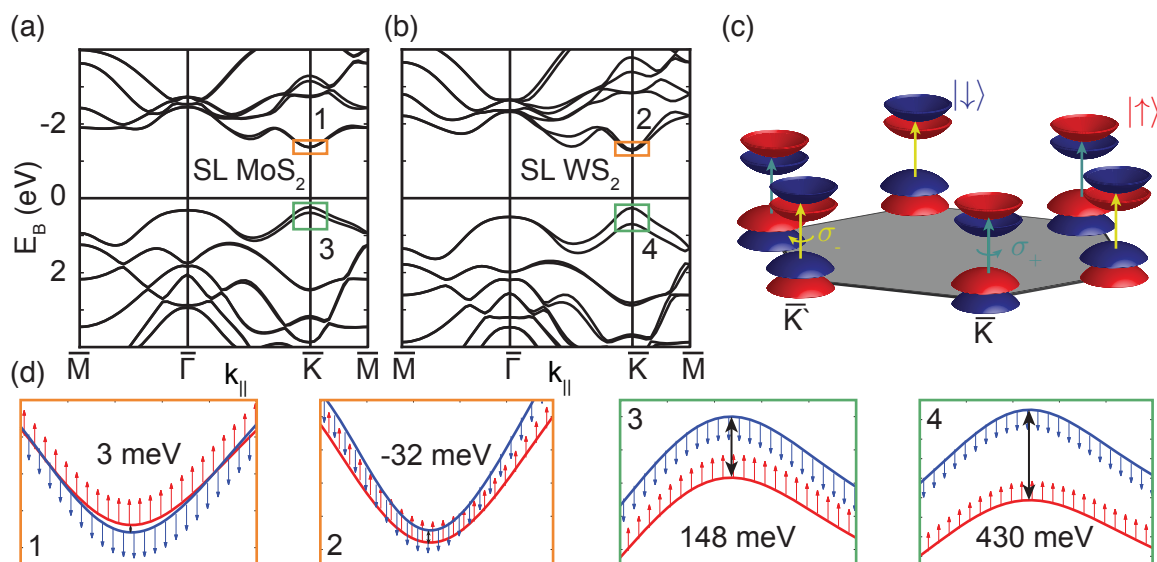


Figure 1.4: DFT calculations of electronic band structures of SL MoS₂ (a) and SL WS₂ (b). Insets shows the dispersion around VBM and CBM, with spin directions indicated by arrows. Insets reprinted after [53]. (c) A schematic of valley-dependent optical selection rules enabling population of a given valley.

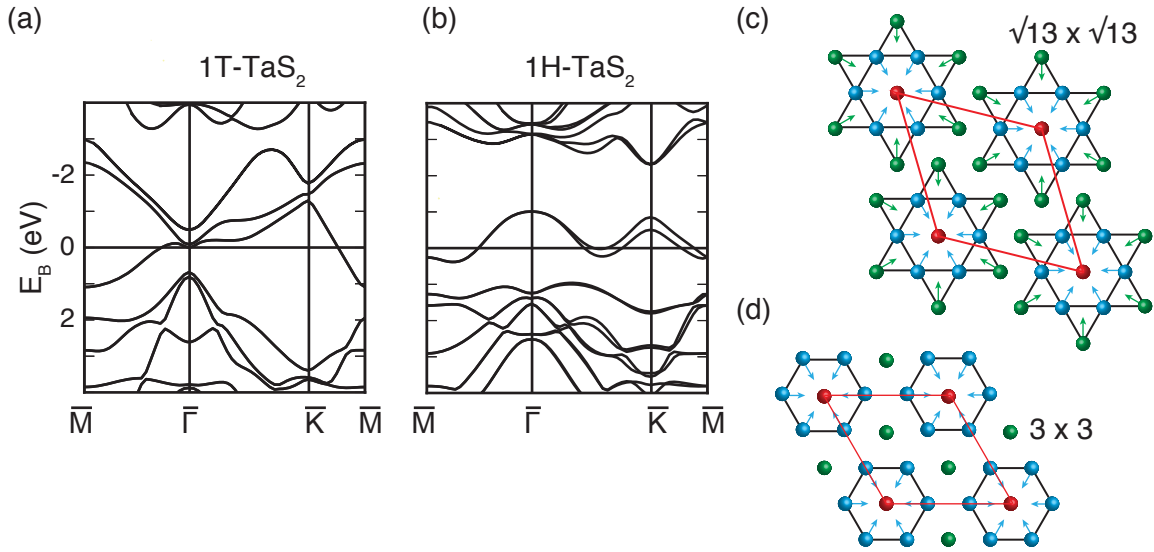


Figure 1.5: DFT calculations of electronic band structure of (a) 1T-TaS₂ and (b) 1H-TaS₂. (c-d) Ball and stick models of CDW superstructure $\sqrt{13} \times \sqrt{13}$ and 3×3 , respectively. Colors mark inequivalent Ta atoms and arrows show the direction of translation.

1.4 Tantalum dichalcogenides

The TMDCs of group 5 exhibit a metallic character at high temperature due to the presence of an unpaired electron in d orbitals. However, these materials are prone to electron instabilities at low temperatures, leading to metal-insulator transition with the onset of a charge density wave (CDW) state. Bulk TaS₂ has been a prototypical system for CDW studies due to the presence of multiple CDW phases, persisting even at room temperature. 1T-TaS₂ at temperatures higher than 543 K is metallic and undistorted. Upon cooling, it transforms into the incommensurate phase down to 347 K, nearly commensurate down to 183 K and commensurate ($\sqrt{13} \times \sqrt{13}$) for lower temperatures (Fig 1.5(c)). After heating the sample from the commensurate phase, an additional triclinic phase occurs and the whole phase diagram shows a hysteresis with respect to the temperature [60]. In case of 2H-TaS₂, there is only one CDW phase (3×3) observed [61], with the onset transition temperature of 75 K (Fig 1.5(d)). Although those materials has been studied for the last three decades, the exact mechanism causing the lattice distortions is still largely unknown. Several mechanisms have been proposed, such as Fermi surface nesting [62], electron-phonon interaction [63] and Van Hove singularities in the density of states [64], but the conclusive determination has not been reached.

Interestingly, indications of CDW competition with low-temperature superconductivity (<1 K) has been found for 2H-TaS₂ [39]. On the other hand, CDW seems to coexist with superconductivity in the 1T phase [65]. Little is it known about how all these interesting phenomena behave in the 2D limit. Quite recently, it was shown that both CDW and SC are realized in SL NbSe₂ [37]. In this case, the temperature of CDW formation was intact in the 2D limit while the SC transition temperature was significantly reduced. Lack of experimental results in the field was the main motivation for studying metallic SL TMDCs in this work.

1.5 Thesis outline

Chapter 2 presents the experimental techniques used in this thesis. The emphasis is placed on angle-resolved photoemission spectroscopy (ARPES), x-ray photoelectron spectroscopy (XPS), and the underlying physical principles. Further, the experimental setup and the SGM3 end-station is described. Finally, scanning tunneling microscopy (STM) and low-energy electron diffraction (LEED) techniques are briefly discussed.

Chapter 3 is devoted to reconstruction-induced Fermi contour modifications that were observed on Au(111). ARPES measurements in the first and higher order surface Brillouin zone (SBZ) are compared. A simple structural model is proposed to account for the unexpected observations.

Chapter 4 introduces methods of the SL TMDCs' synthesis. The morphology and crystal structure of the grown films is studied using STM and LEED techniques. Further, the changes in the SL TaS₂/Au(111) morphology due to different synthesis methods are discussed.

Chapter 5 explores the electronic band structure of SL TMDCs. ARPES results of SLs MoS₂, WS₂ and TaS₂ grown on Au(111), Ag(111) and graphene on SiC are shown. The obtained results are compared to the density-functional theory (DFT) calculations. The substrate-induced effects are discussed in detail. Finally, low-temperature STM/STS results, which reveal the suppression of CDW in SL TaS₂/Au(111), are presented and discussed.

Chapter 2

Experimental techniques

The main focus of this chapter is angle-resolved photoemission spectroscopy (ARPES), as the main experimental technique applied for studying the electronic band structure of SL TMDCs. The underlying physics associated with ARPES and the specifications of the experimental setup are discussed. Also, a very brief overview of the complementary techniques of x-ray photoelectron spectroscopy (XPS), scanning-tunneling microscopy (STM) and low-energy electron diffraction (LEED) is given.

2.1 Angle-resolved photoemission spectroscopy

ARPES is a widely used method of the solid state science, which enables to measure the electronic structure of a material in the direct way. Information about occupied electronic states of the investigated material can be deduced from energy and angle distributions of photoelectrons generated through the photoelectric effect [66, 67]. Furthermore, ARPES technique can be used to study many-body interactions such as the electron-phonon coupling or electron correlations.

This section describes the underlying physics of ARPES in depth suitable for understanding results of this thesis. Further information about the technique can be found in the vast literature covering this topic [68–71]. Description of the experimental setup realization is presented in Section 2.2.

2.1.1 Photoemission

Photoemission is the process of emitting electrons due to the interaction with incoming photons. The explanation of the photoelectric effect was a milestone in quantum mechanics and led to the Nobel Prize in Physics for Albert Einstein. The same principle is employed for ARPES measurements, during which one illuminates a sample with a beam of photons and analyze the energy-momentum distribution of the excited photoelectrons $I(\vartheta, \varphi, E_k)$. The phenomenological three-step model of photoemission provides an intuitive picture of the process (Fig. 2.1).

In the first step, an electron is excited to the final state by interaction with a photon. Energy conservation demands that the kinetic energy of photoelectron E_k satisfies:

$$E_k = h\nu - E_{\text{bin}} - \Phi, \quad (2.1)$$

where $h\nu$ is the photon energy, E_{bin} is the binding energy of the initial state and Φ is the work function of a material. Typical values of Φ stay in the range of 4-5.5 eV. Above equation shows

that the photon energy needs to be at least greater than Φ for photoemission to occur. UV light in the range of 5-100 eV is typically employed for ARPES measurements. Using light in the x-ray regime (typically 0.1-2 keV) enables to excite electrons from non-dispersing core-levels of an atom. X-ray photoelectron spectroscopy (XPS) provides valuable information about the chemical composition and atomic environments found in the studied material.

In the second step, the excited electron travels to the surface, occasionally being scattered. For UV light used for ARPES, the electron inelastic mean free path (IMFP) inside a crystal follows approximately the universal curve and has values of only couple of ångströms. This means that only electrons close to the surface are effectively probed. The inelastically scattered electrons contribute to the background in the observed spectrum. Electrons excited with x-rays have substantially longer IMFP, which translates into the bulk-sensitivity of XPS measurements.

In the third step, the electron refracts at the surface as it leaves the material. The final state wave function needs to match a free-electron state in the vacuum. UV photons carry a negligible momentum in comparison to that of electrons in a crystal, so emission momentum is imparted by the lattice and comes in multiples of the reciprocal lattice vectors \mathbf{G} . Optical transitions in a crystal can be described as vertical transitions in the reduced-zone scheme ($\mathbf{k}_f = \mathbf{k}_i$), but it is useful to describe the photoemission process in the extended-zone scheme ($\mathbf{k}_f = \mathbf{k}_i + \mathbf{G}$), as illustrated in Fig. 2.1(b). Furthermore, the surface gives a boundary condition that breaks the translation symmetry in the perpendicular direction (\mathbf{k}_\perp), so only the parallel component (\mathbf{k}_\parallel) is conserved during this step (Fig. 2.1(c)).

In order to extract information about the crystal momentum of electrons, one can measure the out-coming polar (ϑ) and azimuthal (φ) distributions of the photoelectrons. Assuming the free-electron dispersion in vacuum for the final state and neglecting the momentum of a photon, one can derive:

$$\mathbf{k}_{\parallel,i} = \mathbf{k}_{\parallel,f} = \sqrt{\frac{2m_e E_k}{\hbar^2}} \sin \varphi (\hat{\mathbf{x}} \cos \vartheta + \hat{\mathbf{y}} \sin \vartheta). \quad (2.2)$$

Information concerning the k_z dispersion can be indirectly obtained by changing the photon energy ($h\nu \propto k^2 = k_\parallel^2 + k_z^2$) and modeling the surface as a potential step barrier. However, for 2D electrons found in SL TMDCs this is irrelevant and Eqs. 2.1-2.2 constitute the recipe for the transformation $I(\vartheta, \varphi, E_k) \rightarrow I(\mathbf{k}_\parallel, E_{\text{bin}})$, which, in the first approximation, can be regarded as the measured electronic band structure.

2.1.2 Spectral function

A photoelectron leaving a sample creates a photohole, which perturbs the remaining system. The many-body system will try to fill the empty state through the interactions between electrons and the lattice. This will have an effect on the observed line-shape of ARPES spectra. In order to extract quantitative information about the many-body interactions, one can model the remaining $(N - 1)$ -body system as a quasiparticle and perform the perturbation calculus.

The N -electron wave function before and after photoemission $\psi_{i,f}^N$ can be factored into the single-particle wave function of the photoelectron $\psi_{i,f}^{\mathbf{k}}$ and the remaining photohole $(N - 1)$ -body system $\psi_{i,f}^{N-1}$:

$$\psi_{i,f}^N = A \psi_{i,f}^{\mathbf{k}} \psi_{i,f}^{N-1}, \quad (2.3)$$

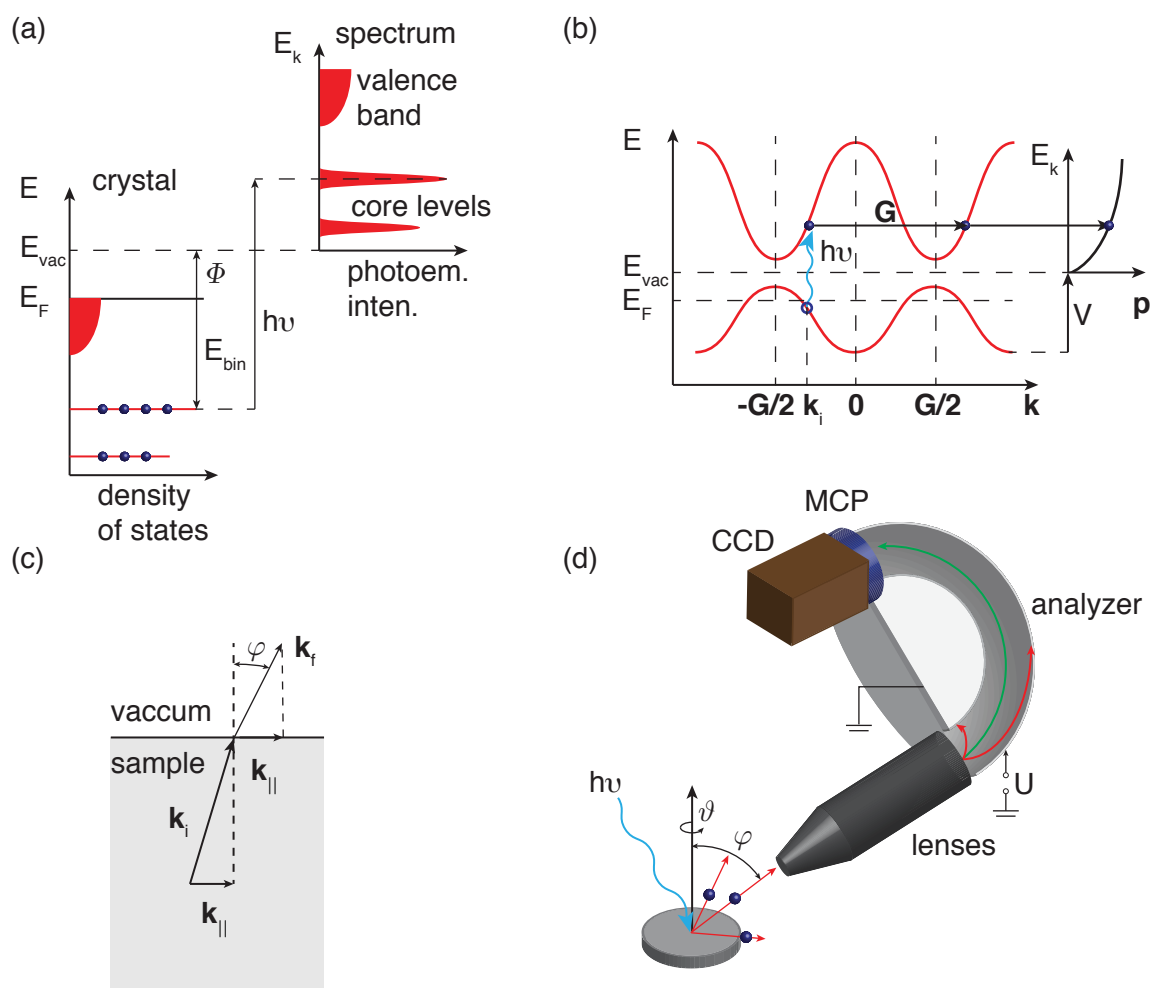


Figure 2.1: (a) The energy scheme for the photoemission process [71]. An electron in a solid (blue sphere) is excited by a photon with the energy $h\nu$. The observed kinetic energy of the photoelectron depends on the excitation energy, the binding energy and the work function of the material. (b) The kinematic diagram of the photoemission process within the three step model [71]. An electron from the valence band is excited with the direct optical transition. The momentum supplied by the lattice enables matching of the wave function with a free-electron final state in the vacuum. The surface is modeled by the potential step V . (c) Refraction of the photoelectron at the surface. (d) A schematic of a typical experimental realization of ARPES. Electrons emitted from an azimuthal (ϑ) and a polar (φ) angle are focused by electrostatic lenses onto the entrance slit of the analyzer. The electric field between two hemispheres enables one to discriminate electrons with a given kinetic energy. A multichannel plate (MCP) multiply the number of filtered electrons which further hit a fluorescence screen. A charge-coupled device (CCD) captures the produced image.

where A stands for an antisymmetric operator used to satisfy the Pauli principle. The above factorization is valid under the assumption that the photoelectron is removed from the system without the interaction with the rest of electrons (sudden approximation) [71]. The light-matter interaction is described with the Hamiltonian H_{int} :

$$H_{\text{int}} = \frac{e}{2m_e c} (\mathbf{A} \cdot \mathbf{p} + \mathbf{p} \cdot \mathbf{A}), \quad (2.4)$$

where \mathbf{A} is the electromagnetic vector potential and \mathbf{p} is the electronic momentum operator. Application of the Fermi's golden rule yields the rate of optical transitions ω_{if} :

$$\omega_{if} = \frac{2\pi}{\hbar} |\langle \psi_f^N | H_{\text{int}} | \psi_i^N \rangle|^2 \delta(E_f^N - E_i^N - \hbar\omega) = \frac{2\pi}{\hbar} |M_{if}^{\mathbf{k}}|^2 |\langle \psi_m^{N-1} | \psi_i^{N-1} \rangle|^2 \delta(E_k + E_m^{N-1} - E_i^N - \hbar\omega), \quad (2.5)$$

where term $|\langle \psi_m^{N-1} | \psi_i^{N-1} \rangle|^2$ is the density of probability that the photohole is left in the excited state m and $M_{if}^{\mathbf{k}}$ is the single-particle matrix elements holding the information about the electron-photon interaction. The photoemission intensity observed in ARPES is then proportional to the sum over all possible transitions, which after the inclusion of the Fermi-Dirac distribution f_{FD} gives:

$$I(\mathbf{k}, E_k) \propto f_{\text{FD}}(E_k) \sum_{i,f} |M_{if}^{\mathbf{k}}|^2 \mathcal{A}(\mathbf{k}, E_k), \quad (2.6)$$

where the photohole spectral function is given by:

$$\mathcal{A}(\mathbf{k}, E_k) = \sum_m |\langle \psi_m^{N-1} | \psi_i^{N-1} \rangle|^2 \delta(E_k + E_m^{N-1} - E_i^N - \hbar\omega). \quad (2.7)$$

Above discussion shows that the ARPES intensity provides information about the photohole spectral function. It is worth noting that this intensity is modulated by the matrix elements describing the light-matter interaction, which depends on the polarization and the energy of the incoming photons. The matrix elements effects can even cause a complete suppression of the ARPES signal [70].

A particularly appealing formulation of the spectral function can be found by employing the Green's function formalism. This approach leads to the spectral function given by:

$$\mathcal{A}(\mathbf{k}, \omega) = \frac{\pi^{-1} |\Sigma''(\mathbf{k}, \omega)|}{(\hbar\omega - \epsilon(\mathbf{k}) - \Sigma'(\mathbf{k}, \omega))^2 + \Sigma''(\mathbf{k}, \omega)^2}, \quad (2.8)$$

where $\hbar\omega$ is the binding energy, $\epsilon(\mathbf{k})$ is the single-particle dispersion, $\Sigma'(\mathbf{k}, \omega)$ and $\Sigma''(\mathbf{k}, \omega)$ are the real and imaginary parts of the electronic self-energy, respectively. The electronic self-energy describes the propagation of electrons in a solid analogously to the complex index of refraction for light. Σ' describes how the band velocity v changes and Σ'' reflects the finite quasiparticle lifetime due many-body effects. Eq. 2.8 indicates that constant-energy cuts through the spectral-function, usually referred to as the momentum distribution curves (MDCs), are Lorentzians. For a simple 1D linear dispersion $\epsilon(k) = \hbar vk$, the Lorentzian is peaked around $k_0 = \omega/v - \Sigma'/(\hbar v)$ and has a full width at half maximum FWHM = $|2\Sigma''/(\hbar v)|$. Lorentzian profiles of MDCs are valid under the assumption that there is no k -dependence in the self-energy.

2.1.3 Photoemission from core-levels

Although XPS is closely related to ARPES, photoemission from core-levels requires an additional discussion. A fundamental difference between ARPES and XPS signals is lack of the momentum

dispersion in the latter case. Binding energies of observed XPS peaks are characteristic for given elements. Also, the energy difference of spin-split components for a given peak are well-known, which can facilitate the peak assignment procedure. A careful analysis of the obtained spectrum enables one to obtain a detailed chemical composition of a sample, including even a very small (ppm range) amount of contamination. Furthermore, a local environment of a photo-emitting atom influences the position and profile of the corresponding spectral line. This can be utilized to study structural phase transitions or changes in the electronic structure due to the interactions with atoms nearby (substrate, intercalants or adsorbants). A splitting of main components can indicate non-equivalent atomic positions in a crystal (e.g., surface reconstruction). CDW phases can also be identified based on XPS spectra [72].

A complete description of all the processes accompanying photoemission from the core-levels is quite complex. Firstly, apart from photoelectron peaks, also Auger peaks are present in the XPS spectrum. These can easily be identified as observed kinetic energies of Auger electrons are independent on the photon energy. Secondly, electrons with sufficient kinetic energies can excite collective oscillations of an electron gas (bulk or surface plasmons). Those excitations can be both intrinsic and extrinsic in nature and are manifested in the spectrum as satellite peaks at the lower kinetic energy side. Further, outgoing electrons can excite valence band electrons into higher energy states. As a consequence energies of photoelectrons are reduced and shake-up satellites emerge a couple eV lower than the main line. The valence band electrons can be even completely ejected by the interaction with photoelectrons, resulting in shake-off features broadening core-level peaks or contributing to the inelastic background. Finally, in case of a high electronic density at the Fermi level, the conduction band electrons can be excited over the Fermi edge due to the interaction with the core-hole. In a simple picture, creation of a core-hole can be treated as the instantaneous switching-on a strong local potential. Due to a wide spectrum of energetic excitations available to conduction electrons, this loss is quasi-continuous, in contrast to the majority of discrete features discussed above, and leads to an asymmetric profile of the XPS signal.

In practice, XPS lines are usually fitted with different profiles depending on the investigated system. A basic profile is given by a Lorentzian, where the natural line width ΔE_0 is related to the lifetime of the core-hole with the uncertainty principle. A small contribution of the temperature-dependent lattice vibrations and an instrumental resolution can be included by convolving the profile with the Gaussian function. In case of metals with a high electron concentration at the Fermi level, asymmetric line shapes are employed such as the function proposed by Doniach and Šunjić (DS) [73]:

$$I_{DS}(E_b) = \frac{\Gamma(1 - \alpha_{DS}) \cos\left(\frac{1}{2}\pi\alpha_{DS} + (1 - \alpha_{DS}) \arctan\left(\frac{2(E_b - E_b^0)}{\Delta E_0}\right)\right)}{[(E_b - E_b^0)^2 + (\frac{1}{2}\Delta E_0)^2]^{\frac{1}{2}(1 - \alpha_{DS})}}, \quad (2.9)$$

where $\Gamma(x)$ stands for the Euler function, $\alpha_{DS} \in [0; 0.5]$ is the asymmetry factor, E_b^0 is the binding energy of the respective core-level and ΔE_0 is full width at half maximum of the corresponding natural (Lorentzian) line. For $\alpha_{DS} = 0$ I_{DS} reduces to a simple Lorentzian, which correspond to lack of interactions with conduction electrons. The DS profile describes relatively well the photoemission signal observed for many elements, but its usage is hindered by being divergent. This means that usually one needs to introduce an arbitrary cut-off energy to extract the area. To deal with this problem, a very similar profile was proposed by Mahan [74], which is convergent. Also, more specific peak functions based on the joint density of states were developed in order to study metallic TMDCs [75]. Examples of XPS line shapes are plotted in Fig 2.2(a).

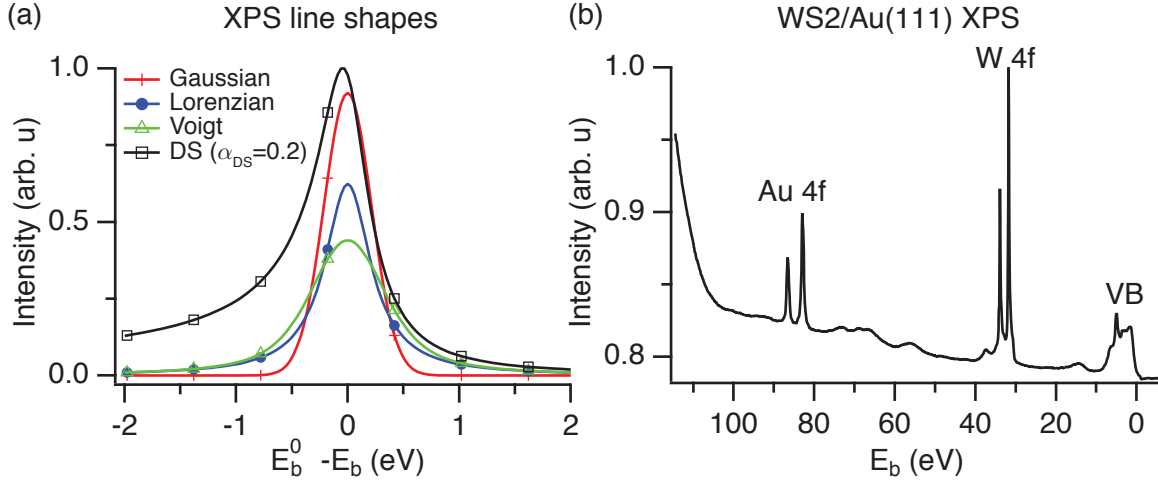


Figure 2.2: (a) Line shapes commonly used for XPS fitting. FWHMs of Gaussian and Lorentzian is set to 0.5 eV and both of those profiles have the same area. The Voigt profile is a convolution of both those peaks. The asymmetric DS profile is calculated for $\alpha_{DS} = 0.2$ with $\Delta E_0 = 0.5$ eV. (b) The survey XPS spectrum for SL WS₂ grown on Au(111). The contributions from W, Au and valence electrons (VB) are indicated on the graph.

Important aspect of the XPS data analysis is an appropriate treatment of the background. The basic type of background function is a line or a small-order polynomial fitted to the arbitrary range on both side of the spectral line. This type of background is expected to result in a larger error than more advanced background functions, but for spectra with high signal-to-noise ratio this error may be tolerable. The most commonly used background function was proposed by Shirley [76]. This semi-empirical approach is based on the assumption that the background is composed of inelastically scattered electrons, whose number is proportional to the number of electrons having a higher kinetic energy. This gives a recursive formula, which can be iterated until the fit converges. Intrinsic flaw of the Shirley background is that it tends to symmetrize the peak profile, which might be inappropriate for the DS function fitting. More physically realistic model based on energy distribution of scattered electrons was developed by Tougaard [77]. This approach, however, make the background in principle element-dependent. Some approximate fitting parameters are available for a wide range of elements [78]. A usage of the Tougaard background usually requires fitting over a large binding energy range around the peak position in order to get a reasonable result, which might be problematic.

Much of valuable information can be extracted from the integral of XPS photoemission intensity A . The contribution from a subshell i of an element X to the total area is given by:

$$A_{Xi} = \int_0^\infty W \sigma_{Xi}(h\nu) \mu_i N_X(z) \exp\left[-\frac{z}{\lambda_X(E_k) \cos(\theta)}\right] dz, \quad (2.10)$$

where z is the distance normal to the surface, W is the experimental factor, $\sigma_{Xi}(h\nu)$ is the total photoionization cross-section, μ_i is the multiplicity of the state i , $N_X(z)$ is the density of atoms X , $\lambda_X(E_k)$ is IMFP and θ is the emission angle. Moreover, the experimental factor W is a function of the light intensity, the analyzed solid angle, the detection transmission function and the angular asymmetry factor. In practice, W is very difficult to accurately determine, but it can be eliminated by taking a reference spectrum. In this work, the coverage of a grown layer of W₂/Au(111) was estimated by taking the ratio between areas of W 4*f* and Au 4*f* peaks (see Fig 2.2(b)) for an overview scan). The obtained results were found in good agreement with the analysis performed using STM data of the same sample.

2.1.4 Acquisition and analysis of ARPES spectra

In order to acquire ARPES spectra, several conditions need to be fulfilled. The experiment needs to be conducted under the ultra-high vacuum (UHV) conditions in order to reduce the scattering of photoelectrons. Furthermore, even the small contribution from the Earth's magnetic field can affect the obtained results, so special μ -metal shielding needs to be employed to screen any residual magnetic field. The band mapping using ARPES requires a precise control of the angle between sample and analyzer, which in UHV is challenging from the technical point of view. The studies of SC or CDW usually requires low-temperature measurements, which pose further technical difficulties.

The range of materials which can be studied with ARPES is limited. The sample needs to be somehow conductive, in order to prevent it from the charge accumulation. The effectively probed area depends on the light spot size, which can put some constraints on the size and the homogeneity of a sample. For instance, mechanically exfoliated layers are typically not suitable for ARPES, because of their lack of uniformity.

Finally, a good energy resolution requires the precise control over the energy of light. To fully exploit ARPES potential, one needs to use a variable-energy, highly monochromatic and brilliant light source. This can be achieved by using synchrotron radiation.

A schematic of the typical experimental setup for ARPES measurements is presented in Fig. 2.1(d). In modern setups 2D detectors are usually employed, enabling simultaneous measurements of the kinetic energy and the incoming angle of photoelectrons. In addition, it is possible to map the dispersion in the whole surface Brillouin zone (SBZ) by rotating a sample and stacking together obtained images. The discrimination of the electron's kinetic energy can be performed by a commonly used hemispherical analyzer or by a time-of-flight spectrometer. All of the presented results in this thesis were acquired using the hemispherical SPECS Phoibos 150 analyzer, so the discussion below is focused on this type of instrument.

The electric field between the two hemispheres diverges electrons' trajectories depending on their kinetic energy. This is achieved in the mirror plane of the analyzer, also called the dispersive plane (see Fig. 2.3(a)). Electrons reaching the analyzer's electrostatic lens system are retarded to the pass energy E_p . Two concentric hemispheres with the electrostatic field between act as band-pass filter, so only electrons within a small energy $E_p \pm \Delta E$ can reach the detector. During the experiment, one can control the size of the energy discrimination window by changing E_p as $\Delta E \propto E_p$, whereas the position of the window on the energy scale can be manipulated through the retarding ratio parameter $r = E_k/E_p$. The energy resolution of the analyzer ΔE_A depends on E_p :

$$\Delta E_A = \frac{E_p(S_1 + S_2)}{4R}, \quad (2.11)$$

where S_1 and S_2 stand for entrance and exit slit widths, respectively, and R is the mean radius of the analyzer. In order to achieve the best resolution, one needs to choose a low value of E_p and a narrow slit. This, however, limits the energy range of the acquisition and the number of electrons observed on the detector.

The non-dispersive plane of a hemispherical analyzer is employed for discrimination of the electrons emission angle φ distribution (Fig. 2.3(b)). The acceptance angle $\pm\beta$ can be selected through the different lens system operation mode. By changing the polar angle θ and the α , one can choose an arbitrary cut through the whole emission hemisphere, enabling the band mapping in whole BZ. The transformation into k -space defined in Eq. 2.2 for the angles defined

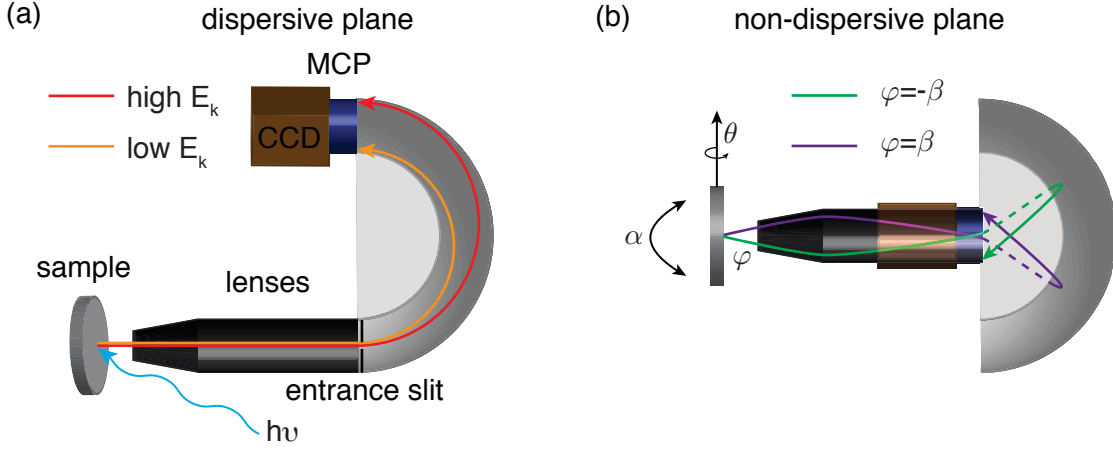


Figure 2.3: (a) The dispersive plane of a hemispherical analyzer. The electric field between the two hemispheres causes deflections of electrons trajectories according to their kinetic energy, which enables the band-pass filtering. (b) The non-dispersive plane of a hemispherical analyzer. The electrons emission angle φ , within the lens mode acceptance angle $\pm\beta$, is projected onto the MCP, enabling the measurement of the angular distribution of incoming electrons. The region of interest in the whole emission hemisphere can be selected by changing the tilt angle α or the polar angle θ .

in Fig. 2.3(b) reads:

$$k_x = \sqrt{\frac{2m_e E_k}{\hbar^2}} (\cos \alpha \sin \varphi - \sin \alpha \cos \theta \cos \varphi), \quad (2.12)$$

$$k_y = \sqrt{\frac{2m_e E_k}{\hbar^2}} \sin \theta \cos \varphi. \quad (2.13)$$

Based on that, the k -resolution Δk_{\parallel} can be approximated by:

$$\Delta k_{\parallel} = \sqrt{\frac{2m_e E_k}{\hbar^2}} \cos \varphi \Delta \varphi. \quad (2.14)$$

The angular resolution $\Delta \varphi$ depends on the chosen lens mode; values of 0.1° can be reached. The k -resolution is a function of the kinetic energy, $\Delta \varphi$ and φ itself. This means that one can easily increase the k -resolution by increasing the emission angle and measuring the dispersion in the higher-order BZ, or by using the low-energy light source. The best achievable k -resolution is lower than 0.01 \AA^{-1} [69]. Apart from the angle-resolved modes, the lens system can be switched to the spatially-resolved mode, where the electrons originating from the small emission angle range are focused on the same place on the detector. This mode of operation is useful for the light-source alignment or XPS.

In order to enhance the signal to noise ratio, a micro-channel plate (MCP) detector is usually employed. Electrons at the end of their travel through the analyzer impinge on the regular array of electron multipliers kept at the high voltage. The avalanche of electrons produced by MCP is mapped on the phosphorous screen. Finally, the image of the photoemission intensity is captured using a CCD camera.

During ARPES measurements some image artifacts are produced, which need to be borne in mind. Spherical aberration, in which electrons having the same kinetic energy can appear to disperse with the emission angle due to the hemispherical geometry of the analyzer; can be compensated by using a curved entrance slit. On the other hand, chromatic aberration, causing energy dispersion lines to be curved, needs also to be properly corrected. In this work correction

for chromatic aberration was made after an image is acquired, using transformation software supplied by SPECS.

Quantitative analysis of ARPES spectra demands taking into account extrinsic effects accompanying the photoemission process such as the Gaussian broadening $G(\Delta\omega, k_{\parallel})$ due to experimental resolution and secondary electron emission constituting the observed background $I_0(\omega)$. This together with Eq. 2.6 gives:

$$I(\omega, \mathbf{k}_{\parallel}) = [\mathcal{A}(\mathbf{k}_{\parallel}, \omega)M(\omega, \mathbf{k}_{\parallel})f_{FD}(\omega)] * G(\Delta\omega, k_{\parallel}) + I_0(\omega), \quad (2.15)$$

where $\Delta\omega$ is the total energy resolution, combining both the light-source and the analyzer's contributions. The cuts of constant energy (MDC) or constant momentum (EDC) are usually fitted using Lorentzian or Voigt profiles on top of a polynomial background. The measured kinetic energy is transformed into the binding energy by finding the position of the Fermi edge and using Eq. 2.1.

2.2 Experimental setup

All of ARPES and XPS measurements relevant to this dissertation, as well as the majority of the growth, was conducted at the newly-built SGM3 endstation (ASTRID2 storage ring, Institute for Storage Ring Facilities, Aarhus University). Some of STM results were obtained as a part of collaboration with the group of Prof. Alexander Khajetoorians (Radboud University). The initial growth of SL MoS₂ was performed in the laboratory of Prof. Jeppe Vang Lauritsen (Aarhus University). The discussion below is restricted only to the SGM3 experimental setup.

2.2.1 ASTRID2 and SGM3 beamline

ASTRID2 [79] is a small electron storage ring with a circumference of ca. 45.7 m, operating at the energy of 580 MeV (see Fig. 2.4(a)). The old synchrotron ASTRID, has been adapted to be a booster ring for ASTRID2. This enables ASTRID2 to be run in the top-up mode. Moreover, the upgrade from ASTRID to ASTRID2 decreased the horizontal emittance from 0.16 mm to 10 nm, resulting in a much smaller beam spot on a sample. The new design of ASTRID2 enables to store up to 200 mA of an electron current. An overview of the ISA facility is presented in Fig. 2.4.

The SGM3 beamline [80] is supplied with the synchrotron radiation by an undulator installed on ASTRID2. An undulator is a device consisting of a movable array of magnets with alternating polarity. Electrons inside an undulator are forced to move in a curved trajectory, which stimulates the emission of highly-collimated and polarized synchrotron radiation. The photon energy can be varied continuously over a wide range by changing the gap between the magnets inside the undulator. The light entering the beamline is focused on the entrance slit (ENS) by the horizontal (HFM) and the vertical (VFM) focusing mirrors (see Fig. 2.4(c)). The selection of the given light energy in the range of 10-150 eV also requires three interchangeable spherical grating mirrors (SGM) together with the exit slit (EXS). The final alignment of the light beam is performed by adjusting the toroidal post focusing mirror (PFM). The spot size on a sample is ca. 200 μm \times 50 μm . The total energy resolution of the beamline depends on the size of EXS, but typically it is better than 10 meV.

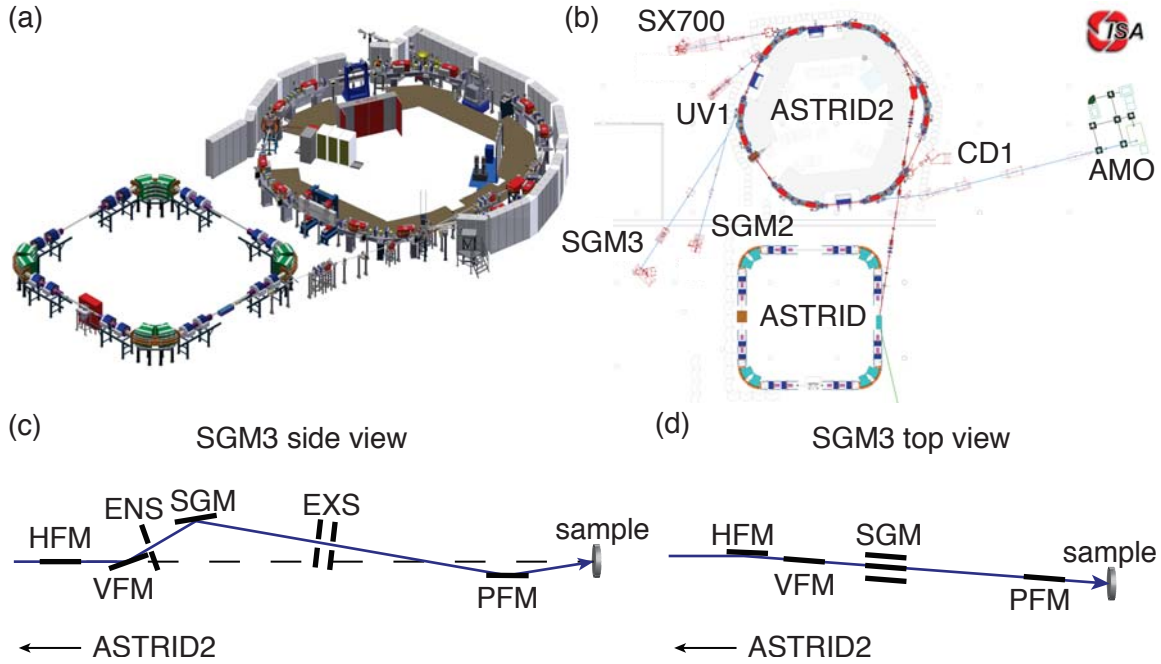


Figure 2.4: (a) A visualization of the ASTRID and ASTRID2 synchrotrons. (b) The beamline arrangement in the ISA facility. (c)-(d) Side and top views on the SGM3 beamline, respectively. See text for a detailed description. Images taken from [81].

2.2.2 End station

A part of the author's Ph.D. project was devoted to setting up the measurement system and, in particular, to developing the dedicated data acquisition software. A schematic of the SGM3 endstation is presented in Fig. 2.5(a). The setup consists of four chambers separated by valves. The small chamber, called load-lock (LL), is used for introducing a sample to the UHV without venting the larger chamber. The preparation chamber (base pressure $2 \cdot 10^{-10}$ mbar) is used for surface treatments of a sample, such as Ne^+ ion sputtering or annealing. It also hosts the STM instrument (Aarhus type) for the surface characterization. The main chamber (base pressure $7 \cdot 10^{-11}$ mbar) is equipped with the LEED unit, the 5-axis manipulator and the hemispherical analyzer. The sample stage is connected to a closed-cycle He cryostat, enabling to cool down a sample to ca. 100 K. Recently, the manipulator has been upgraded to a new design in which all six axes of motion are motorized and the sample stage is cooled by a more powerful He cryostat, which enables reaching the temperature of ca. 50 K on a sample. Readings of the sample's temperature are performed with a K-type thermocouple attached to the back of a crystal. The rotation of the manipulator, communication with the synchrotron and other peripheral devices as well as data acquisition and analysis are done by dedicated software written in the IGOR Pro by the author (Fig. 2.5(b)). This enables to perform automatic measurements to a large extent. The growth of samples is done in the dedicated chamber (base pressure $2 \cdot 10^{-10}$ mbar), using an electron-beam evaporator (EBE-4, SPECS), or Ta filament, and a custom-built H_2S doser. Transportation of samples for external STM measurements was performed using a home-built UHV suitcase, which can be directly attached to the growth chamber. Non-evaporable getter together with battery-powered ion pumping systems make the suitcase portable and convenient to use.

The growth of low-dimensional materials and UHV cleaning of the substrates are quite time-consuming tasks. In order to increase efficiency in cleaning and preparation of substrates, a sep-

arate UHV chamber was also employed for the substrate preparation. This system is equipped with computer-controlled piezoelectric leak valves and silicon evaporators. This enables to sputter and anneal crystals, as well as grow graphene on various substrates, in a fully-automatic way. The software controlling the system was developed in the LabVIEW environment by the author. Further experimental details can be found online [82].

2.3 Structural investigation techniques

During the synthesis of 2D materials, several growth parameters need to be optimized in order to obtain desired results. Techniques such as STM or LEED reveal information about the structure of an investigated system. This knowledge is invaluable in the process of finding the appropriate growth recipe. Also, STM measurements probe the local electronic properties whereas ARPES signal is spatiality-averaged over the area of a light spot, so those two techniques are in some sense complementary. Sections below are devoted to the basic aspects of STM and LEED techniques.

2.3.1 Scanning-tunneling microscopy

The principle of the scanning-tunneling microscopy (STM) operation is based on the electron tunneling phenomenon. When a sharp tip is brought close to a sample, electrons can tunnel through the vacuum barrier between the tip and the surface (Fig. 2.6(a)). Application of the bias voltage between the STM tip and a sample U_t results in the measurable tunneling current I_t , which is a function of the sample-tip distance d :

$$I_t \propto U_t \exp\left(-\frac{\sqrt{8m_e\Phi}}{\hbar}d\right). \quad (2.16)$$

For the typical values of a metal work function the tunneling current decays by ca. one order of magnitude, when the distance increases by 1Å. Thus, electrons effectively tunnel only through single atoms of the STM tip apex, enabling reaching the atomic resolution. The precise movement control of the tip can be obtained by using piezoelectric motors, where the movement is proportional to the applied voltage. Typically in experiments, the tip is raster-scanned over the surface, while the proportional-integral-derivative (PID) feedback loop adjusts sample-tip distance to keep the tunneling current constant. This way the image of the sample's local density of states (LDOS) convolved with the LDOS of the tip is measured. By reversing the sample-tip bias one can probe both occupied and unoccupied states. In the first approximation, one can relate the obtained image to the topography of the surface. An example of an STM image is presented in Fig. 2.6(c).

STM can be used for a variety of applications such as nano-manipulation, tracking adsorption processes or observing chemical reactions at surfaces. The related technique of scanning-tunneling spectroscopy (STS) provides local information about the electronic density of states, by sweeping of the applied voltage while keeping the distance and position constant. However, this requires a precise calibration and a careful analysis of the obtained results.

The tunneling process can be influenced by the chemical composition of the tip and its interactions with the sample. For very small tip-sample distances, chemical forces have a profound effect on the tunneling current. Just before the contact, chemical bonding can be formed which

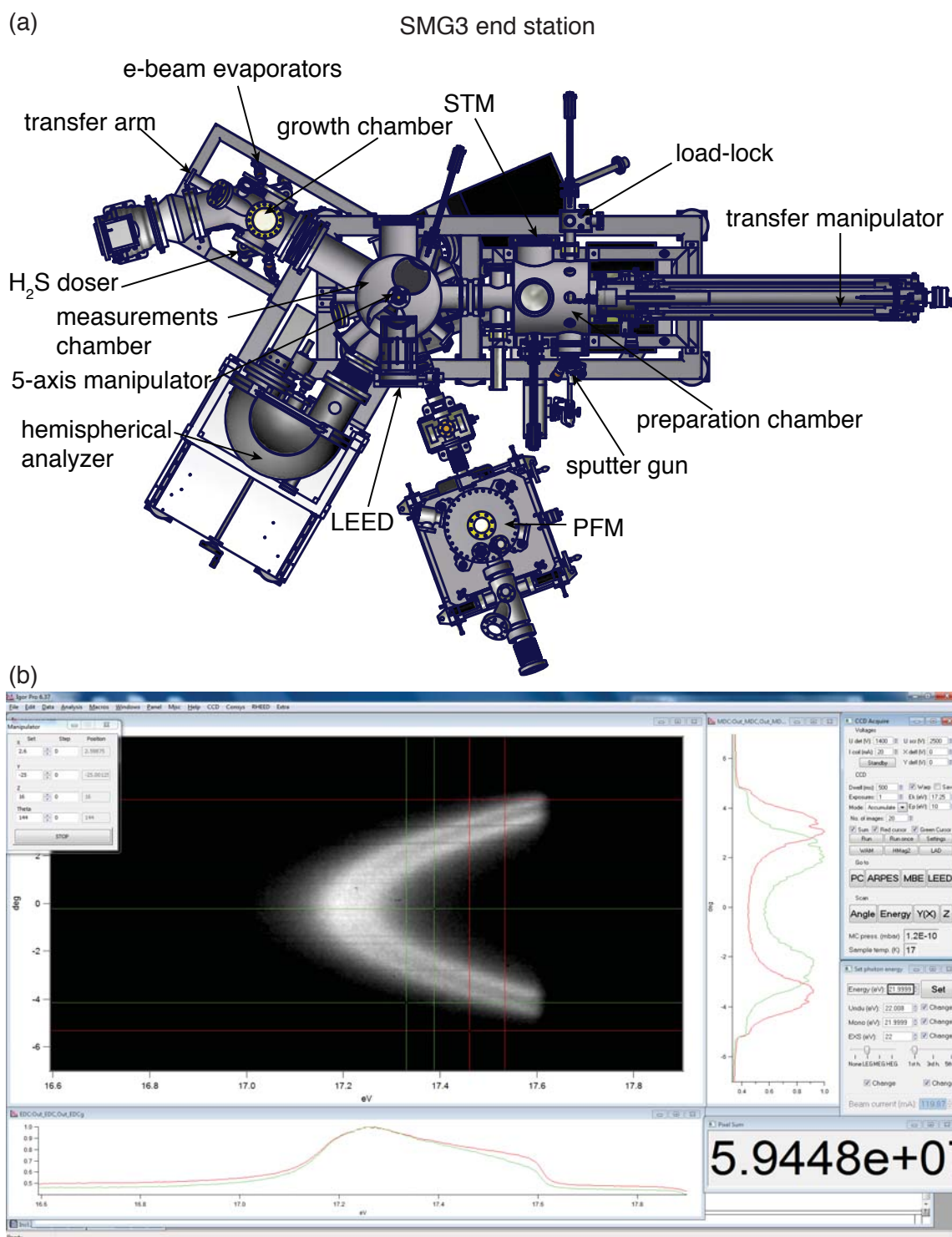


Figure 2.5: (a) A schematic of the SGM3 endstation consisting of four chambers. The load-lock chamber (LL) is used for introducing samples to the system. The preparation chamber is used for preparing the surface (Ne^+ ion sputtering and annealing) and STM measurements. The measurement chamber (MC) hosts the 5-axis manipulator, the LEED unit and the hemispherical analyzer. It is connected with the ASTRID2 synchrotron through the post-focusing mirror (PFM) chamber. Electron-beam evaporators and the H_2S doser are situated in the growth chamber. Transfer of a sample is done by the motorized transfer manipulator and the magnetic transfer arms. (b) A screenshot of the data acquisition software during ARPES measurement of the Au(111) surface state.

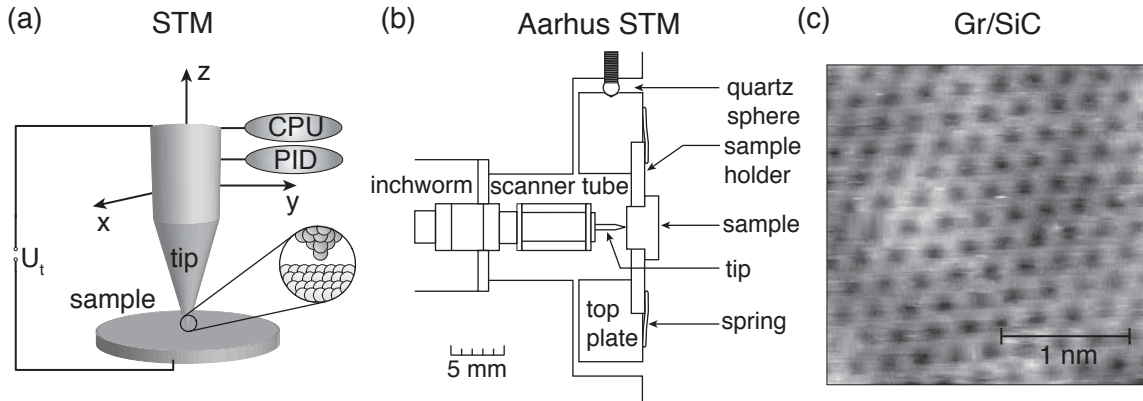


Figure 2.6: (a) A visual representation of the STM technique. (b) The design of the Aarhus STM [83]. (c) STM image of graphene grown on 6H-SiC.

leads to modifications of the surface. Those modifications can be temporary as well as permanent. Moreover, a very high electric field density in the neighborhood of the tip can also perturb the studied system.

In this work the Aarhus STM was used (2.6(b)). It is a very compact design mounted directly on a flange and attached to the UHV chamber. The rough approach of the tip is realized by the inchworm motor consisting of the piezoelectric tube with the three segments of electrodes clamped on a SiC rod. Proper biasing of the segments ensures that the outermost segments clamp/unclamp while the middle section expands/contracts. This enables the movement of the rod in a worm-like manner during the approach. Precise movement during the scanning is provided by the piezoelectric tube. The top plate is insulated both electrically and thermally from the block by three quartz spheres. The sample holder is fixed in place by springs. During measurements, the whole STM is floating on light springs, which greatly decreases the mechanical noise.

It should be noted that the neighboring synchrotron generates some electrical noise issues which cannot be easily resolved. Also, Aarhus STM design is not optimally suited for low-temperature measurements and all of the STM experiments at the SGM3 endstation were performed at room temperature. For that reason, low-temperature STM measurements described in this thesis were performed in the external laboratory, in a collaboration with the group of Prof. Alexander Khajetoorians (Radboud University).

2.3.2 Low-energy electron diffraction

Information about the global surface quality can be obtained using LEED. This technique exploits the electron diffraction phenomenon to gather information about the surface composition, quality and structure. Due to the low energy of the used electrons (10-300 eV), only the region close to the surface is effectively probed.

A typical LEED setup consist of an electron gun, a retarding grid and a fluorescent screen (2.7(a)). The retarding grid is used to focus and filter diffracted electrons, so that only elastically scattered electrons reach the fluorescent screen. For electrons arriving at the sample surface at normal incidence, the Laue condition reads:

$$\Delta \mathbf{k}_{\parallel} = h \mathbf{b}_1 + k \mathbf{b}_2, h, k \in \mathbb{Z}. \quad (2.17)$$

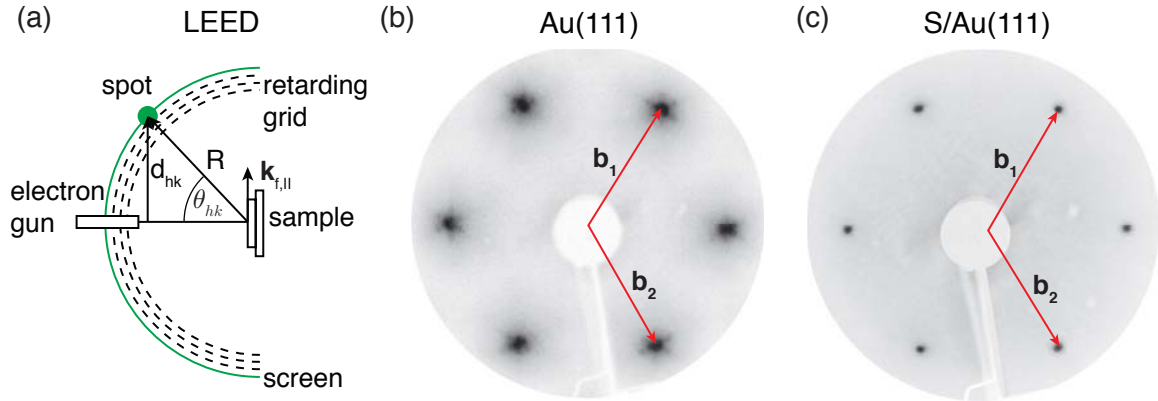


Figure 2.7: (a) A schematic of LEED operation. (b) LEED image of Au(111). Characteristic replica spots are due to the herringbone reconstruction. (c) LEED image of S/Au(111) surface, where sulfur absorption lifts the reconstruction

Thus, the projected distance from the electron gun axis to the spot produced on the fluorescent screen is a simple function of the diffraction angle θ_{hk} and the sample-screen distance R :

$$d_{hk} = R \sin(\theta_{hk}) = R \frac{k_{f,\parallel}}{k_f} = R \sqrt{\frac{\hbar^2}{2m_e E_k}} |h\mathbf{b}_1 + k\mathbf{b}_2|. \quad (2.18)$$

Using the above results, it is possible to assign the obtained LEED pattern to the reciprocal lattice vectors \mathbf{b}_i (Fig. 2.7(c)). One can also distinguish between the contribution from the substrate and from the adlayer in order to obtain the information about their relative orientation or the superstructures such as moiré patterns. A sample's cleanliness can be judged from the observed LEED pattern. For example, clean Au(111) surface reconstructs in the well-known herringbone superstructure [84], which results in the observation of additional spots, as shown in Fig. 2.7(b). A small amount of contamination might result in lifting-off the reconstruction, which changes the observed LEED pattern (Fig. 2.7(c)). Also, adsorbates and defects can cause the incoherent electron diffraction which increases the spot size. Based on such considerations, one can judge the overall quality of the surface. In a more sophisticated approach, the spot intensity is analyzed as a function of the electrons' kinetic energy (I-V). This analysis requires assuming some specific model of the surface and comparing the simulation with the obtained LEED I-V profile.

The LEED technique is especially useful for the structural studies of 2D materials. Due to their atomic thickness, the LEED patterns of such materials consist of spots originating from both the substrate and the epilayer, and this enables a direct comparison of the reciprocal lattice vectors. As the substrate crystal structure is usually well-known, one can estimate the lattice constant of a 2D material with an uncertainty below 1%.

Chapter 3

Surface reconstruction effects on the Au substrate

This chapter focuses on the Au(111) surface, as the main substrate used for the growth of SL TMDCs. The unexpected modifications of the surface electronic structure of Au(111) due to herringbone reconstruction are presented. ARPES measurements performed in the first and higher order SBZs are shown and compared with the simulated spectral functions. Structural models of the herringbone reconstruction are thoroughly discussed.

3.1 Herringbone reconstruction of Au(111)

Au(111) is a quite unique system, as it is the only fcc (111) surface which exhibits a reconstruction at room temperature. The so-called herringbone reconstruction (Fig. 3.1(a)) is a moiré-like pattern, arising from the top-most layer being uniaxially compressed by ca. 4.55%, such that 23 lattice spacings of the top layer fit on 22 lattice spacings of the second layer. This results in a rectangular superstructure unit cell, which is 22 times longer than the original lattice vector in one direction and $\sqrt{3}$ times this lattice vector in the other. The surface atoms occupy FCC, HCP and bridge positions (Fig. 3.1(b)) within the superstructure unit cell. Interestingly, the atomic spacing of the top layer along the $\langle 1\bar{1}0 \rangle$ direction is not constant, but shows a small variations ($\pm 0.1\text{\AA}$) around the mean value (2.75 \AA) (Fig. 3.1(c)). The overall strain on the surface is relaxed by $\pm 120^\circ$ rotation every $\approx 250\text{ \AA}$ [84]. This reconstructed surface hosts a free electron-like surface state [85] that has been intensely studied using angle-resolved photoemission spectroscopy (ARPES) and scanning tunnelling microscopy (STM), revealing phenomena such as spin-orbit splitting of surface states [86–88], quasiparticle interference in the presence of spin-polarised bands [89], surface state lifetimes [90, 91], and lifetimes in spin-split systems [92]. Despite the major surface reconstruction, ARPES data show only very minor effects of the atomic arrangement on the observed surface state dispersion [93] and cross-section [94]. This is hard to reconcile with several indications from STM [95, 96] and theory [97, 98] that the reconstruction has a non-negligible effect on the surface state wave function.

Here we show that the surface reconstruction does indeed have a major influence on the dispersion probed by ARPES, but only on the dispersion measured away from normal emission in a SBZ center corresponding to a higher diffraction order. The uniaxial compression of the lattice directly affects the reciprocal lattice and thus the position of the higher order zone centers. Together with the three rotational domains present on the surface, the measured dispersion turns from a simple parabolic state with a circular Fermi contour to a complex dispersion with constant energy surfaces resembling a trefoil knot. This dominating Fermi contour does

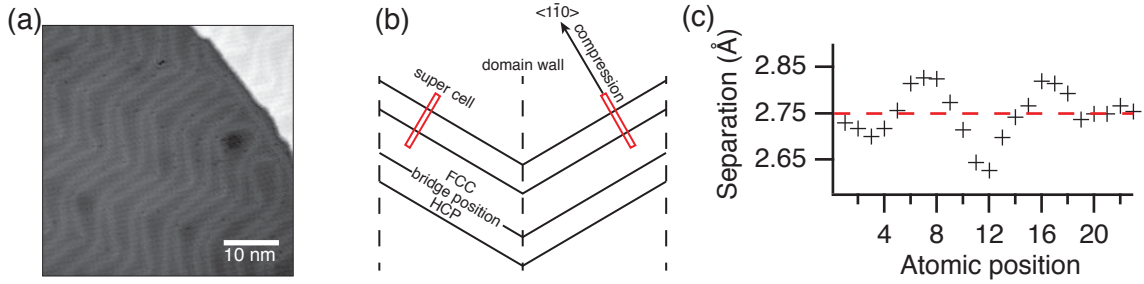


Figure 3.1: (a)-(b) STM image and a schematic of the herringbone reconstruction, respectively. (c) The atomic separation along the compression direction- $\langle 1\bar{1}0 \rangle$. Data taken from Ref. [84].

not simply consist of replicas caused by the overall moiré periodicity but rather by displaced dispersions induced by the local lattice distortion.

3.2 Trefoil knot Fermi contour

ARPES data were taken at the SGM-3 beamline of the synchrotron radiation facility ASTRID2 in Aarhus. The energy and angular resolution were better than 30 meV and 0.2° , respectively. The sample temperature was 100 K. The synchrotron radiation was linearly polarized in the k_y plane; incident direction and electron analyzer enclosed an angle of 50° . Au(111) surface was cleaned by standard methods of sputtering in Ne atmosphere followed by annealing [86, 91]. The cleanliness and presence of the surface reconstruction were corroborated by STM.

Figure 3.2 illustrates the effect of the herringbone reconstruction when ARPES data is taken in a higher order SBZ for two photon energies, 42.5 eV and 61.0 eV. Data taken around normal emission (Fig. 3.2(a)-(c)) show the expected free electron-like dispersion of the state with the two spin-split bands clearly discernible and a Fermi contour consisting of two concentric circles, in excellent agreement with earlier results [86, 91, 92]. Note that the bands are not quite as clearly resolved as in some previous publications, notably in the direction perpendicular to the slit of the electron analyzer (along k_y). This is mostly due to the high photon energy used here, which results in an inferior k -resolution. While the periodicity of the moiré structure in other systems has been observed to lead to weak replicas and band gap openings in ARPES data at low temperature and with low photon energies around normal emission [93], this is not observed here, presumably because these replicas are too weak.

Fig. 3.2(d)-(f) and (g)-(i) show a measurement of the electronic structure around the $\bar{\Gamma}_2$ point in the adjacent SBZ where a much more complex picture emerges. The dominating features are three versions of the original dispersion centred around different points, with Fermi contours forming a trefoil knot of spin-split circles, best seen in Fig. 3.2(d). This results deviates in subtle but important ways from the previously discussed case of replicas induced by the moiré superstructure [93], where one would expect the observation of one dominating dispersion and six very weak replicas. By contrast, the trefoil knot contour can be explained by the local uniaxial compression along $\langle 1\bar{1}0 \rangle$ directions in three domains of the moiré superstructure. In fact, the observed dispersions are not “replicas” in the sense of features resulting from scattering by the moiré periodicity, but rather are the dispersions centred around the first order reciprocal lattice points of different domains. This has the interesting consequence that two of the three dispersions stem from one domain each, in contrast to the domain averaged dispersion around $\bar{\Gamma}_1$.

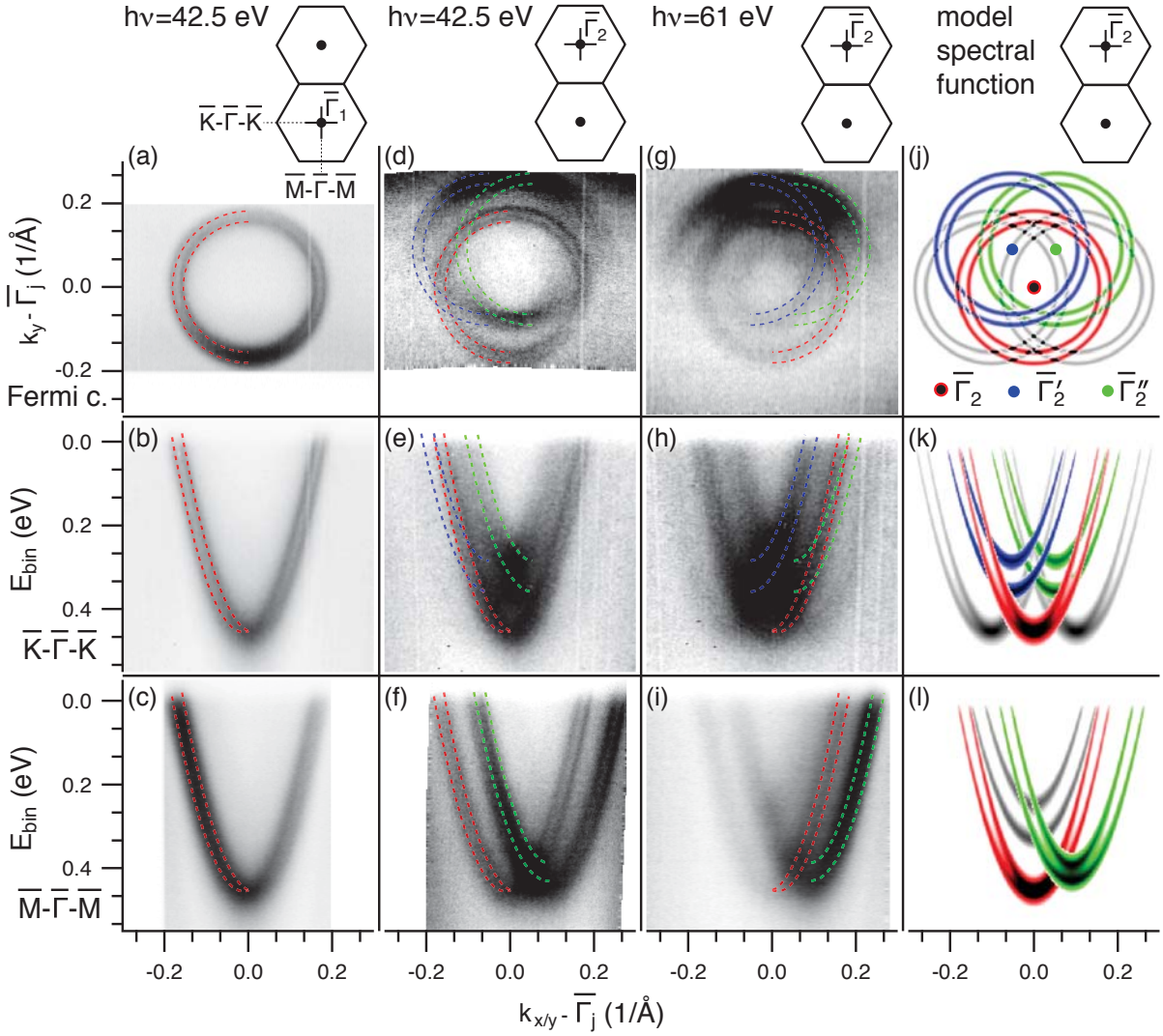


Figure 3.2: Surface electronic structure of Au(111) measured at photon energies of 42.5 eV and 61.0 eV, and calculated by a model spectral function. The photoemission intensity is shown as a function of binding energy and/or crystal momentum (k_x, k_y) along the cuts indicated in the sketches on top of the figure, with zero fixed at $\bar{\Gamma}_1$ for panels (a)-(c) or $\bar{\Gamma}_2$ (d)-(i); dark corresponds to high intensity. Panels (a)-(c) show data taken at normal emission as dispersions through the SBZ center and as constant energy contour at the Fermi energy. Panels (d)-(f) and (g)-(i) show the corresponding data taken around $\bar{\Gamma}_2$, the center of the adjacent SBZ. (j) -(l) Model spectral function around $\bar{\Gamma}_2$ with cuts corresponding to those in panels (a)-(i). The colored branches are centered on the first order reciprocal lattice points of the three domains. The (weaker) grey branches are additional replicas. (see Fig. 3.3). Note that the blue and green bands in (k) and the green band in (l) do not reach to the same high binding energy as the red dispersion because the cut is not taken through their center. The colored dispersions (only symmetrical halves of each pair) are also shown as dashed lines on top of the data in (a)-(i)

The accepted structural model for $22 \times \sqrt{3}$ reconstruction is given in Fig. 3.3(a) [84, 99]. The key to understanding the findings in Fig. 3.2 is not this overall periodicity but the change in the local geometry required to obtain it: As shown in Fig. 3.3(a) and (b), the compression of the first layer leads to a slight distortion of the lattice in this layer (in red) compared to the underlying crystal (in black), giving rise to an oblique lattice in contrast to the underlying hexagonal lattice. The corresponding reciprocal lattices for the first layer and the underlying lattice are given in Fig. 3.3(c).

Due to momentum conservation, the photoemission from solids always involves the lattice-periodic potential and the photoemission cross section connecting a final state at wave vector \mathbf{k}_f with an initial state at $\mathbf{k}_f - \mathbf{b}$ is proportional to Fourier coefficient $|V_{\mathbf{b}}|^2$ of the lattice-periodic potential (\mathbf{b} is a reciprocal lattice vector) [100]. We therefore expect to observe the Au(111) surface state not only around normal emission but around all reciprocal lattice vectors \mathbf{b} with a finite $V_{\mathbf{b}}$. We call these points $\bar{\Gamma}_i$. For the limiting cases of a surface state only located in the first layer (deeper layers), these $\bar{\Gamma}_i$ points would correspond to the red (black) reciprocal lattice points in n Fig. 3.3(c) and one would expect to observe dispersions centered there.

If the surface state wave function follows both the periodicity of the truncated bulk *and* that of the first layer, the $\bar{\Gamma}_i$ points for the combined reciprocal lattice and the corresponding $|V_{\bar{\Gamma}_i}|^2$ can be obtained using the convolution theorem of Fourier transformation [101]. The $|V_{\bar{\Gamma}_i}|^2$ can be assumed to predict the relative intensities from the surface state dispersions. Fig. 3.3(d) shows the position of the $\bar{\Gamma}_i$ points for the three rotational domains of the reconstruction as discussed in Sec. 3.3. The area of the points corresponds to the value of $|V_{\bar{\Gamma}_i}|^2$. The color (RGB) encodes the domain a particular $\bar{\Gamma}_i$ stems from. Black indicates contributions from all the truncated bulk. This simple model predicts the presence of three strong dispersions along with two weak ones. The three intense dispersions are centred on the $\bar{\Gamma}_i$ points of the first layer reciprocal lattice for the three rotational domains on the surface $\bar{\Gamma}_2, \bar{\Gamma}'_2, \bar{\Gamma}''_2$. The weaker dispersions can be considered to be replicas. This prediction is in excellent qualitative agreement with the results in Fig. 3.2. Note that the kinematic diffraction pattern for the surface would be obtained in a similar way and Fig. 3.3(d) is very similar to electron diffraction data from Au(111) [102].

The physical picture leading to the pattern in Fig. 3.3(d) is significantly different from that previously used to account for the replica bands around normal emission. In Ref. [93], such replicas are explained by an interaction of the surface state with the long-range moiré pattern. The expected $\bar{\Gamma}_i$ points for this case can also be calculated, using the large scale moiré structure rather than the nearly equal competing periodicities of first and deeper layers (Sec. 3.3). The resulting $\bar{\Gamma}_i$ points are shown in Fig. 3.3(e) along with their $|V_{\bar{\Gamma}_i}|$. Fig. 3.3(d) and (e) both predict weak replica bands around $\bar{\Gamma}_1$, consistent with the results of Ref. [93]. However, the models are distinctly different for the situation close to $\bar{\Gamma}_2$. For an interaction with a large-scale moiré structure, one would expect to observe six replicas around *every* reciprocal lattice point of the undistorted lattice and the replicas around $\bar{\Gamma}_2$ would be even weaker than those around $\bar{\Gamma}_1$. While the intensity of the six moiré-induced replicas around each original reciprocal lattice point is exactly symmetric in our simple model, this would not strictly need to be so in an ARPES experiment because of k -dependent matrix element variations.

The ARPES results with only three prominent Fermi contours are clearly in much better agreement with the model in Fig. 3.3(d), as are the contours' positions. We perform a more quantitative comparison by constructing a spectral function based on the superposition of dispersions, according to the calculated $\bar{\Gamma}_i$'s in Fig. 3.3(d). The parameters for the dispersion are taken from a fit to the data around normal emission. The result of this is shown in Fig. 3.2(j)-(l) with colors chosen such that the red, blue and green dispersions in the figure correspond to the

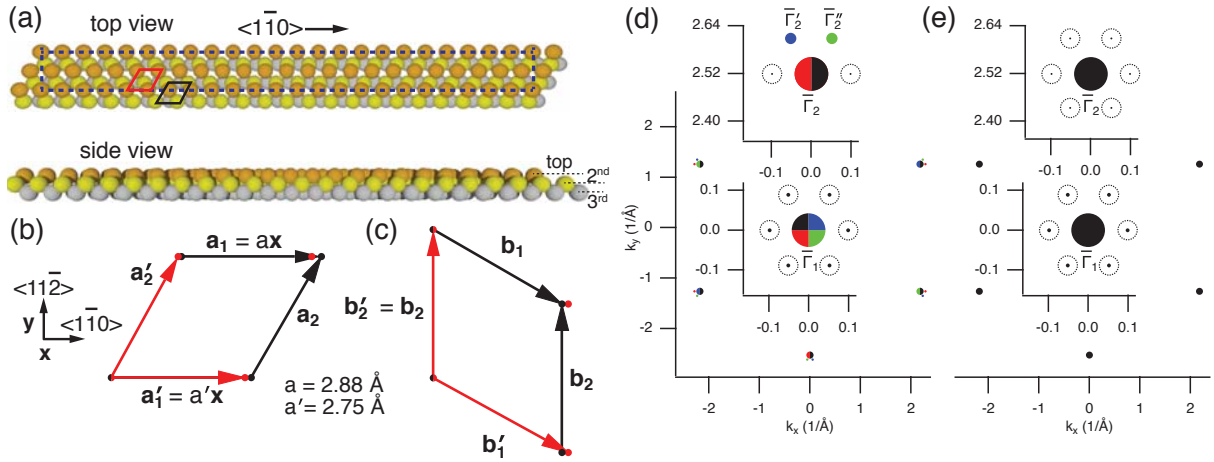


Figure 3.3: (a) Structural model of the Au(111) herringbone reconstruction, showing only one domain. The solid black and red lines give the unit cell of the truncated bulk and the first layer only, respectively. The dashed line denotes the reconstructed unit cell. (b) Relation between the lattice vectors \mathbf{a}_1 , \mathbf{a}_2 of the truncated bulk and the lattice vectors \mathbf{a}'_1 and \mathbf{a}'_2 of the first layer, arising from a uniaxial compression. (c) Corresponding reciprocal lattice vectors. (d) Expected origins of surface state dispersions ($\bar{\Gamma}_i$ points) for three domains with simultaneous periodicities according to the reciprocal lattices in (c). The marker radius is proportional to $|V_{\bar{\Gamma}_i}|$ except for the point around $\bar{\Gamma}_1$ which is scaled down by a factor of 2. Regions around the origin and the first reciprocal lattice point in the vertical direction are magnified in the insets. (e) Corresponding plot for simultaneous periodicities of the truncated bulk (black arrows in (c)) and the overall moiré (Sec. 3.3).

$\bar{\Gamma}_2$, $\bar{\Gamma}'_2$ and $\bar{\Gamma}''_2$ points in Fig. 3.3(d) and the grey dispersions correspond to the weaker replicas. The three strong dispersions are superimposed on the data and good agreement is found. The weak dispersions can also be seen, especially in Fig. 3.2(g), (h). The many bands and their overlap can make the direct comparison difficult but some of the details are better seen when comparing the model to second derivatives of the photoemission data in Fig. 3.4(a)-(d). The spectral function around $\bar{\Gamma}_2$ is dominated by three dispersions for all photon energies studied here. The replica bands, represented by the grey dispersions, are very weak and only barely observed for $h\nu = 61$ eV. No dispersions at the “bottom” of the hexagon (i.e., closer to the $\bar{\Gamma}_1$ point, as would be expected for the dispersion resulting from the presence of the moiré) are ever observed. The model of Fig. 3.3(d) also predicts that the two outer dispersions (around $\bar{\Gamma}'_2$ and $\bar{\Gamma}''_2$) should stem from different domains, implying that there cannot be any gap openings at the crossing points of the $\bar{\Gamma}'_2$ and $\bar{\Gamma}''_2$ parabolas, and this is confirmed by the data presented in Fig. 3.4(e).

The two scenarios in Fig. 3.3(d) and (e) are merely limiting cases and not mutually exclusive, but the strength of the effects is very different. The competing periodicities in the first and second layer leading to the trefoil knot Fermi contour are present on a short range: If the surface state wave functions are influenced by the first layer periodicity, this immediately leads to a significant component in the Fourier spectrum. The effect of the overall moiré periodicity, on the other hand, may be weak because of the weak Fourier coefficients for this modulation, the finite number moiré periodicities in one domain and the finite quantum coherence of the wave function [103]. On the other hand, both models predict six weak replicas around $\bar{\Gamma}_1$ and the results reported here are therefore consistent with those of Ref. [93]. Even the observation of initial state gaps between the centre dispersion and these replicas is not in contradiction to the findings here - gap openings would only be prevented between neighboring replicas as these

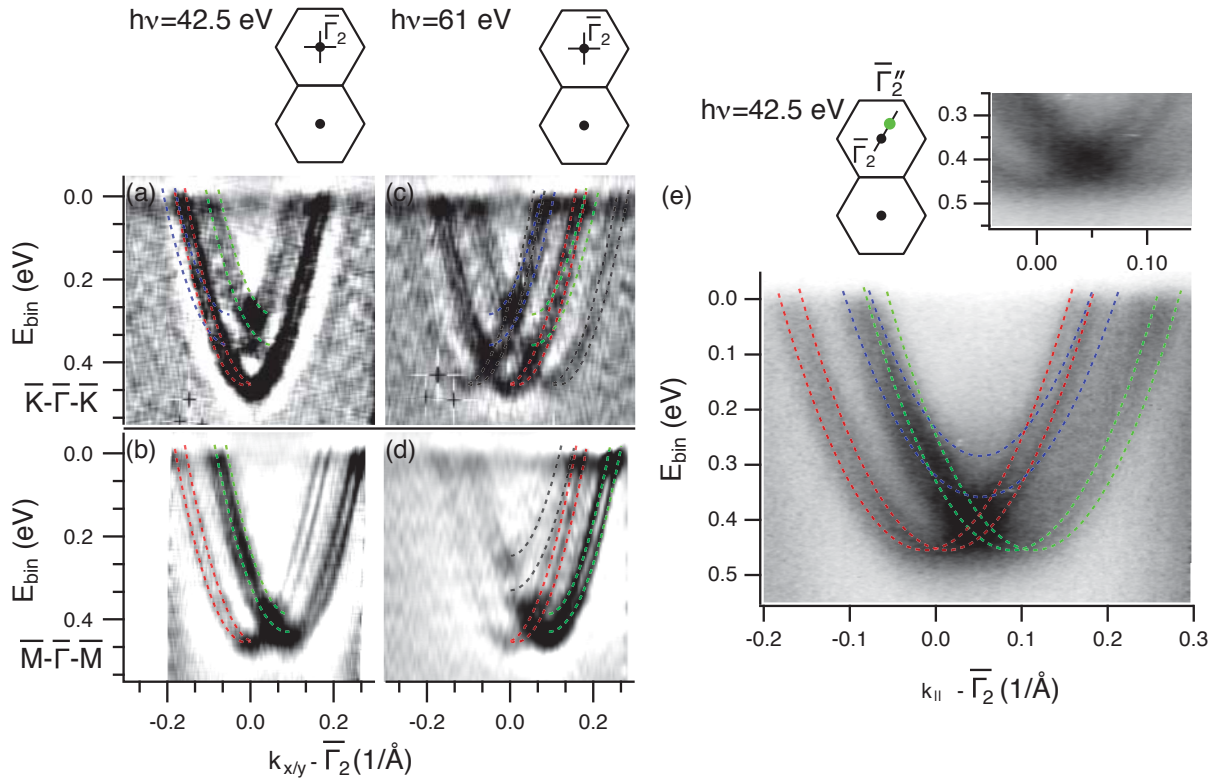


Figure 3.4: (a)-(d) Same figures as (e)-(f) and (h)-(i) in Fig 3.2, respectively, but showing second derivatives of the photoemission intensity instead of the intensity as such. The dispersion of moiré replicas is indicated by grey lines. (e) Surface electronic structure of Au(111) along the cut $\bar{\Gamma}_2-\bar{\Gamma}_2''$ ($\bar{\Gamma}-\bar{K}$), as indicated in the sketch on top of the figure, measured at photon energy of 42.5 eV. The photoemission intensity is shown as a function of binding energy and crystal momentum k_{\parallel} with zero fixed at $\bar{\Gamma}_2$. The colored dispersions are shown as dashed lines on top of the data. The inset is a magnification of the same data and an intensity enhancement, i.e. no gap opening, at the crossing of surface states originating from different rotational domains.

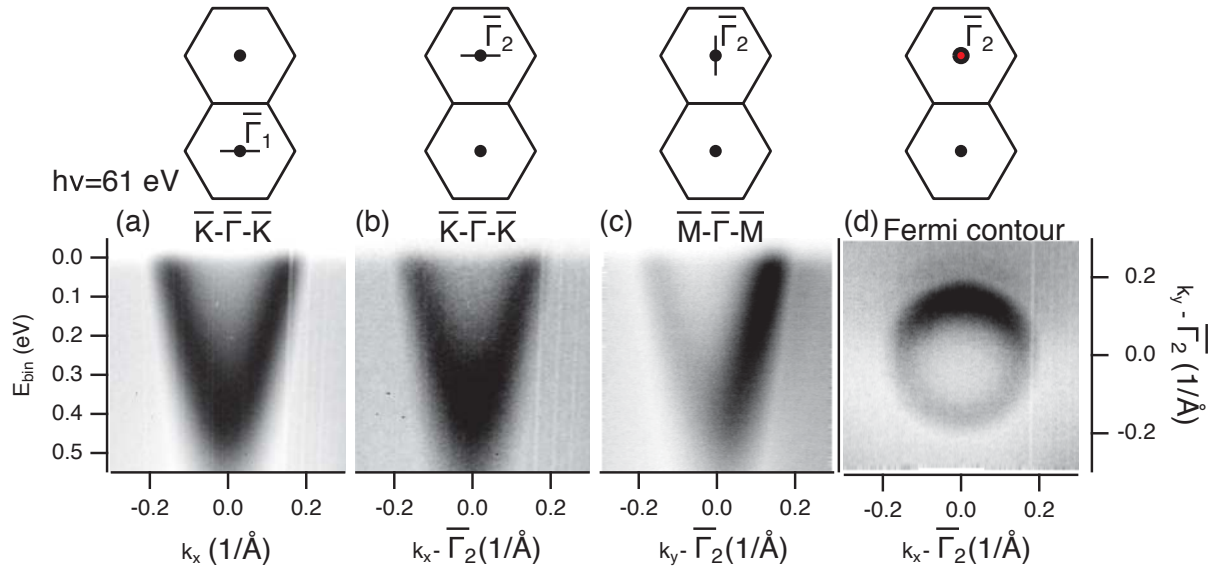


Figure 3.5: Surface electronic structure of Au(111) after lifting the herringbone reconstruction by exposure to H₂S, measured at a photon energy of 61.0 eV. The photoemission intensity is shown as a function of binding energy and / or crystal momentum (k_x, k_y) along the cuts indicated in insets with zero fixed at $\bar{\Gamma}_1$ for panel (a) and $\bar{\Gamma}_2$ for panels (b)-(d); dark corresponds to high intensity.

stem from different domains of the reconstruction.

Previous ARPES results from Au(111) have shown that the consequences of herringbone reconstruction can be detected but that the effect is quite weak [93, 94]. This was in puzzling contrast to results by STM [95, 96] and density functional theory (DFT) [97, 98] which show that the surface state wave functions (or the Kohn-Sham orbitals) are strongly influenced by the reconstruction. In particular, DFT can track the surface state wave function, showing a strong localization of the state in the first layers and a periodicity that follows both the first and the lower layers. We show here that this does also lead to a strong effect in ARPES, but only as regards the surface state in a higher Brillouin zone. The separation of the trefoil knot Fermi surfaces is expected to increase still more when going to even higher order $\bar{\Gamma}$ points. It is also worth noting that introducing the reconstruction in DFT shifts the surface state band at $\bar{\Gamma}$ in binding energy from 350 to 490 meV, and thereby brings it into excellent agreement with the experimental results. When the reconstruction is lifted, for example by sulphur adsorption (see Fig 2.7), this binding energy is again reduced to 376(10) meV and the trefoil knot Fermi contour disappears (Fig 3.5).

We note that the approach of calculating the maps in Fig. 3.3(d) and (e) by just two competing periodicities is, of course, a simplification. On a local scale, STM indicates a stronger binding of the surface state electrons in the hexagonally closed packed regions between first and second layer [95, 96], suggesting a complex interplay between surface state and local structure. Moreover, the compression of the atoms in the first layer is not entirely uniform [84, 99]. However, an estimate of this imperfect periodicity's effect on the expected diffraction pattern shows that it only induces minor changes as discussed in Sec. 3.3. We also note that the simple picture presented here does not account for final state effects.

An interesting consequence of our findings is that it is possible to observe the surface state dispersion in a single domain, such as around $\bar{\Gamma}'_2$ and $\bar{\Gamma}''_2$, instead of the average from all three

domains around $\bar{\Gamma}_1$ or $\bar{\Gamma}_2$. This opens the possibility to test the non-parabolicity of the state. Indications of this effect have previously been detected by STM on Cu(111) and Ag(111) [104] and recently even by ARPES on Au(111) for the domain-averaged Fermi contour around $\bar{\Gamma}_1$ [105]. A more practical consequence relates to the importance of the Au(111) surface state for the calibration of spin detectors. Such a calibration is routinely done using the surface state around $\bar{\Gamma}_1$ [106, 107] but there might be advantages to using the dispersion of a single domain instead.

3.3 Oblique unit cell model of the surface

We start the discussion of the model with an assumption that inter-atomic spacing is constant and given by the mean value of 2.75\AA . This leads to expressions for the top layer \mathbf{a}_i and projected bulk \mathbf{a}'_i lattices:

$$\mathbf{a}_1 = a(1, 0), \mathbf{a}_2 = a \left(\frac{1}{2}, \frac{\sqrt{3}}{2} \right), \quad (3.1)$$

$$\mathbf{a}'_1 = a'(1, 0), \mathbf{a}'_2 = \left(\frac{a'}{2}, \frac{a'\sqrt{3}}{2} \right), \quad (3.2)$$

where $a=2.88\text{\AA}$ and $a'=2.75\text{\AA}$. Thus, corresponding reciprocal lattices are given by:

$$\mathbf{b}_1 = 2\pi \left(\frac{1}{a}, -\frac{1}{a\sqrt{3}} \right), \mathbf{b}_2 = 2\pi \left(0, \frac{2}{a\sqrt{3}} \right), \quad (3.3)$$

$$\mathbf{b}'_1 = 2\pi \left(\frac{1}{a'}, -\frac{1}{a'\sqrt{3}} \right), \mathbf{b}'_2 = 2\pi \left(0, \frac{2}{a'\sqrt{3}} \right). \quad (3.4)$$

The three-fold symmetry of the underlying bulk is reflected by existence of rotational domains of the top layer, which are taken into account in the model by $2\pi/3$ and $4\pi/3$ rotated \mathbf{b}'_i .

The compression of the atoms in the top layer is, however, not uniform [84, 99] and it is interesting to ask how this affects the model outlined above. We test this in the one-dimensional model in Fig. 3.6. Fig. 3.6(a) juxtaposes a lattice manifesting the imperfect, position-dependent periodicity previously discussed in Refs. [84, 99] (red line, with changing periodicity indicated quantitatively at top of panel) with a perfectly periodic function (black dashed line). Fig. 3.6(b) shows the corresponding Fourier transformations. The positions of the first order Fourier components are the same for both cases. The imperfect periodicity leads to a loss of intensity in the first order Fourier coefficients and to very broad side bands around their positions. The consequence of this for the surface state dispersion is a weakening of the coherent dispersions and a slight increase of the background. While the distortion is much bigger than typical atomic vibrations, the result is thus similar to what is described by a Debye-Waller factor in X-ray diffraction.

Another important question is what are the implications of the local strain picture compared to the overall moiré periodicity model. In order to illustrate the differences we first consider a one-dimensional model in Fig. 3.7. The figure and the discussion are adapted from the recent work on moiré structures of graphene by Zeller and Günther in Ref. [101]. We consider two

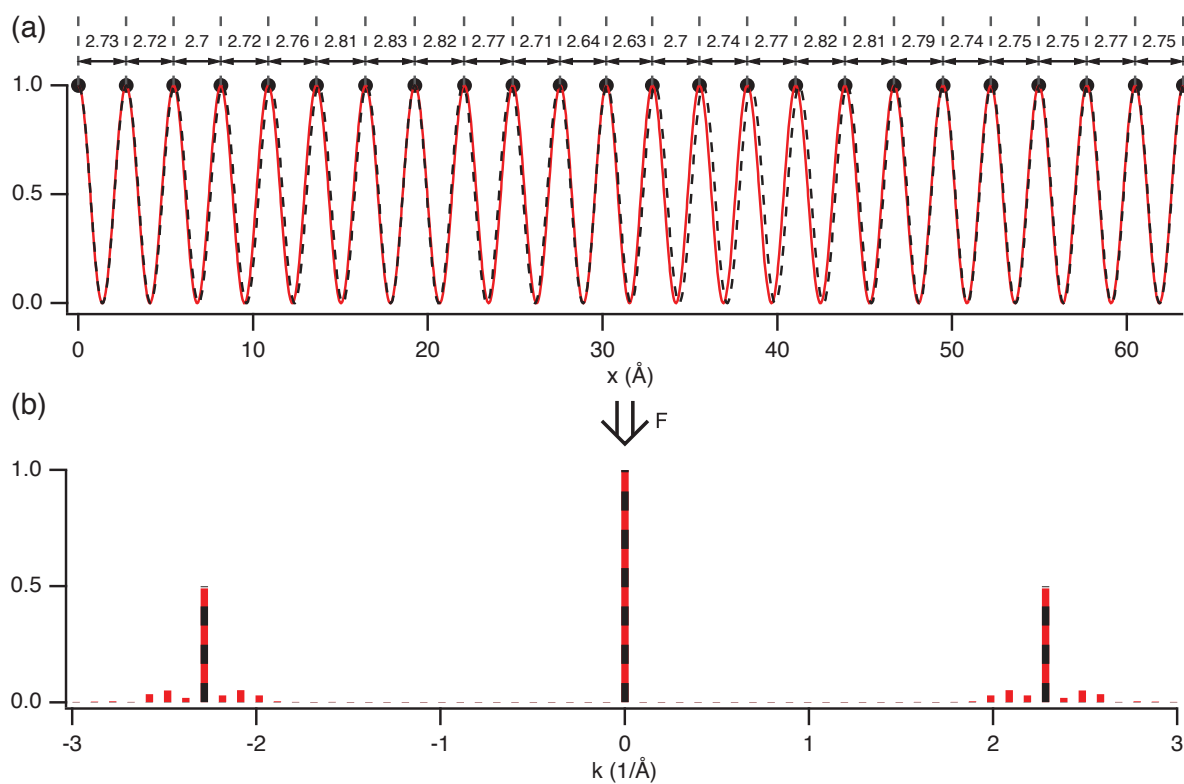


Figure 3.6: Effect of an irregular lattice spacing in the top layer. (a) One-dimensional model of the non-uniform compression in the top layer with the interatomic distances given in Å. The black dashed line is a periodic function for the perfect lattice. The red line is a quasi-periodic function tracking the position of the top layer atoms. (b) Fourier transformation of the two functions.

periodic functions $f_1(x)$ and $f_2(x)$, both of the form $f_i(x) = 1 + \cos(k_i x)$ (the actual values of the Fourier coefficients could be different for the two functions but this does not matter for the simple illustration here). The overall periodicity of the system shall be given by the product of f_1 and f_2 . Fig. 3.7(a) shows this situation represented by the Fourier coefficients $F\{f_1\}$ and $F\{f_2\}$, describing f_1 and f_2 , such that f_1 represents the periodicity of the Au(111) truncated bulk lattice parallel to the surface and f_2 represents the long-range moiré periodicity (with a small k_2). If only one periodicity were present (either only the lattice or only the moiré), the location of non-zero Fourier coefficients would give the Γ_i points. When seeking the Γ_i points for the product, we need to evaluate

$$F\{f_1 \times f_2\}(k) = F\{f_1\}(k) \otimes F\{f_2\}(k) = \int F\{f_1\}(k - k') F\{f_2\}(k') dk' \quad (3.5)$$

where \otimes denotes the convolution of $F\{f_1\}$ and $F\{f_2\}$. This is done graphically: Finite contributions for $F\{f_1\} \otimes F\{f_2\}$ arise when $F\{f_1\}$ is shifted by a k value such that finite Fourier coefficients in $F\{f_1\}$ come into registry with finite coefficients in $F\{f_2\}$. This is the case for shifts by the colored arrows in Fig. 3.7(a). The resulting values of $F\{f_1\} \otimes F\{f_2\}$ can also be directly read from the figure by multiplying the lengths of the overlapping bars: For the orange arrow it is $1 \times 0.5 = 0.5$ and for the blue it is $0.5 \times 0.5 = 0.25$. $F\{f_1\} \otimes F\{f_2\}$ now gives the Γ_i points for the combined system and, at this simple level of theory, the value of the Fourier coefficients represents the strengths of the expected dispersions. Replicas would be found around the origin and around the higher order diffraction spots of the regular lattice and the latter replicas would be weaker than the former.

Fig. 3.7(b) shows the same construction for a situation dominated by the simultaneous presence of the two local periodicities. f_1 again represents the periodicity of the Au(111) truncated bulk lattice parallel to the surface but f_2 now corresponds to the slightly compressed periodicity of the top layer. Following the identical construction of $F\{f_1\} \otimes F\{f_2\}$, we obtain only two Γ_i values in the vicinity of the original single higher order spot of the lattice, not three. Moreover, the Fourier coefficients of the two have equal values in this model.

With this, we numerically calculate the equivalent of Fig. 3.7 in two dimensions in Figs. 3.8 and 3.9 and we present these results schematically in Figs. 3.3(d) and (e). As in the one-dimensional model, the choice of the Fourier coefficients $V_{\mathbf{b}}$ in $f_1(\mathbf{k})$ and $f_2(\mathbf{k})$ is arbitrary. Fig. 3.8 shows the evaluation of the $\bar{\Gamma}_i$ and $|V_{\bar{\Gamma}_i}|$ for the interaction of the truncated bulk lattice (periodicity \mathbf{b}_1 and \mathbf{b}_2 , Fig. 3.8(a)) with the moiré periodicity in one direction (Fig. 3.8(b)). As in Ref. [93], the moiré periodicity is modeled by only one Fourier component in the long direction of the moiré (22 times the lattice constant) and none in the short direction ($\sqrt{3}$ times the lattice constant). The convolution of the two images of Fig. 3.8(a) and (b) is shown in Fig. 3.8(c). It leads to the presence of two weak spots around every position of non-zero Fourier coefficient of the lattice. These spots are weaker around higher order lattice points than around the origin. Fig. 3.8(d) shows the summation of the result in (c) for all three domains present on the surface. The result is consistent with the experimental findings in Ref. [93].

The corresponding situation for the simultaneous presence of the truncated bulk (\mathbf{b}_1 and \mathbf{b}_2) and top layer (\mathbf{b}'_1 and \mathbf{b}'_2) periodicities is shown in Fig. 3.9. If we choose the domain of interest in the same way as in Fig. 3.3, the reciprocal vectors \mathbf{b}_2 and \mathbf{b}'_2 are identical and therefore only one intense spot appears around the position called $\bar{\Gamma}_2$ in Fig. 3.3. However, the convolution also gives rise to two weak replicas close to this. For other first order lattice spots (see second inset in Fig. 3.9(c)), the first order reciprocal lattice vectors are not the same for the top layer and truncated bulk and thus two strong Fourier components appear but no additional weak ones. Finally, when summing over all three domains, every first order reciprocal lattice vector shows

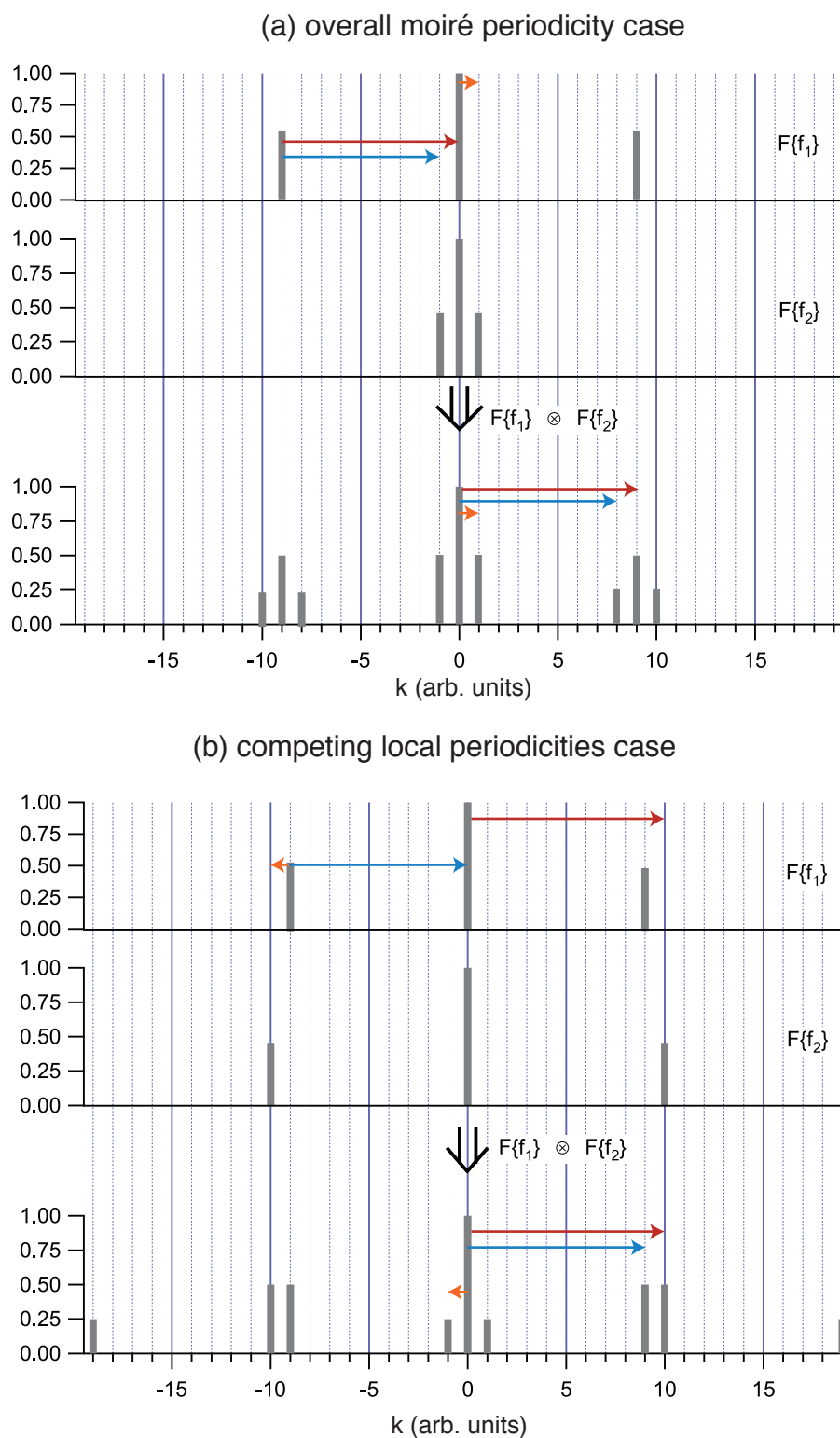


Figure 3.7: One-dimensional model for the calculation of expected surface state dispersion origins. (a) Situation for the simultaneous presence of truncated bulk lattice and overall moiré periodicity. (b) Situation for simultaneous presence of the truncated bulk lattice and the slightly shorter periodicity in the top layer. The arrows illustrate the convolution of the two functions. Each colored arrow corresponds to a k movement that brings finite Fourier components in $F\{f_1\}$ in registry with those in $F\{f_2\}$ and thereby leads to finite values in $F\{f_1\} \otimes F\{f_2\}$ at this k .

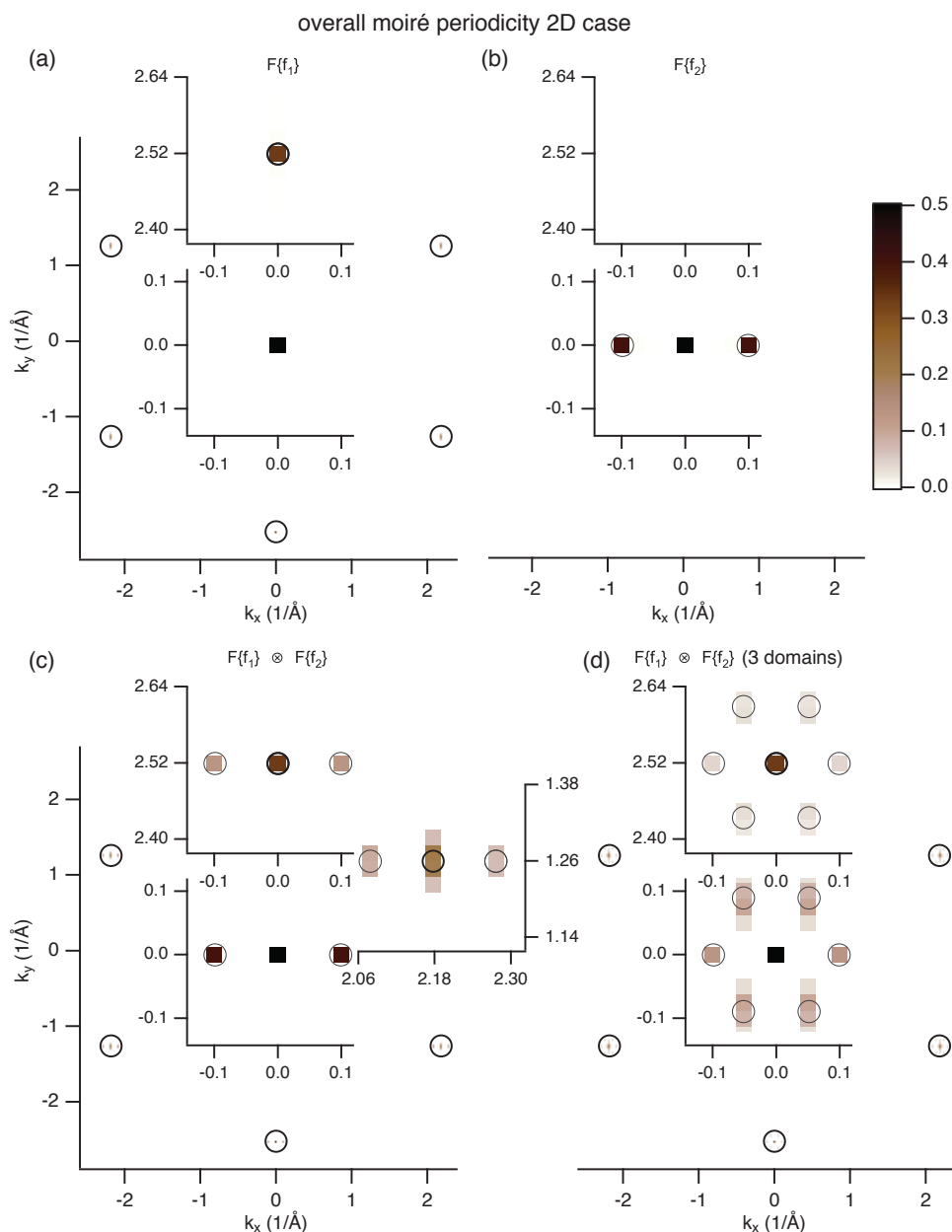


Figure 3.8: (a) and (b) Fourier coefficients $|V_{\mathbf{b}}|$ for the truncated bulk lattice (\mathbf{b}_1 and \mathbf{b}_2) and the moiré periodicity in one domain, respectively. The intensity is normalized to the zeroth order component and mapped with the colors scale included in the figure. The peaks are, in some cases, difficult to see and therefore partly marked by circles around them. The regions around the origin and the first reciprocal lattice point in the vertical direction are magnified in the insets. (c) Convolution of (a) and (b). (d) Sum of convolution of (a) and (b) for the three possible domains on the surface.

three high coefficients in its vicinity and two weak ones. (Fig. 3.9(d)). Figs. 3.9(d) and (e) show a schematic representation of these results in which the magnitudes of the Fourier coefficients are encoded in the size of the markers.

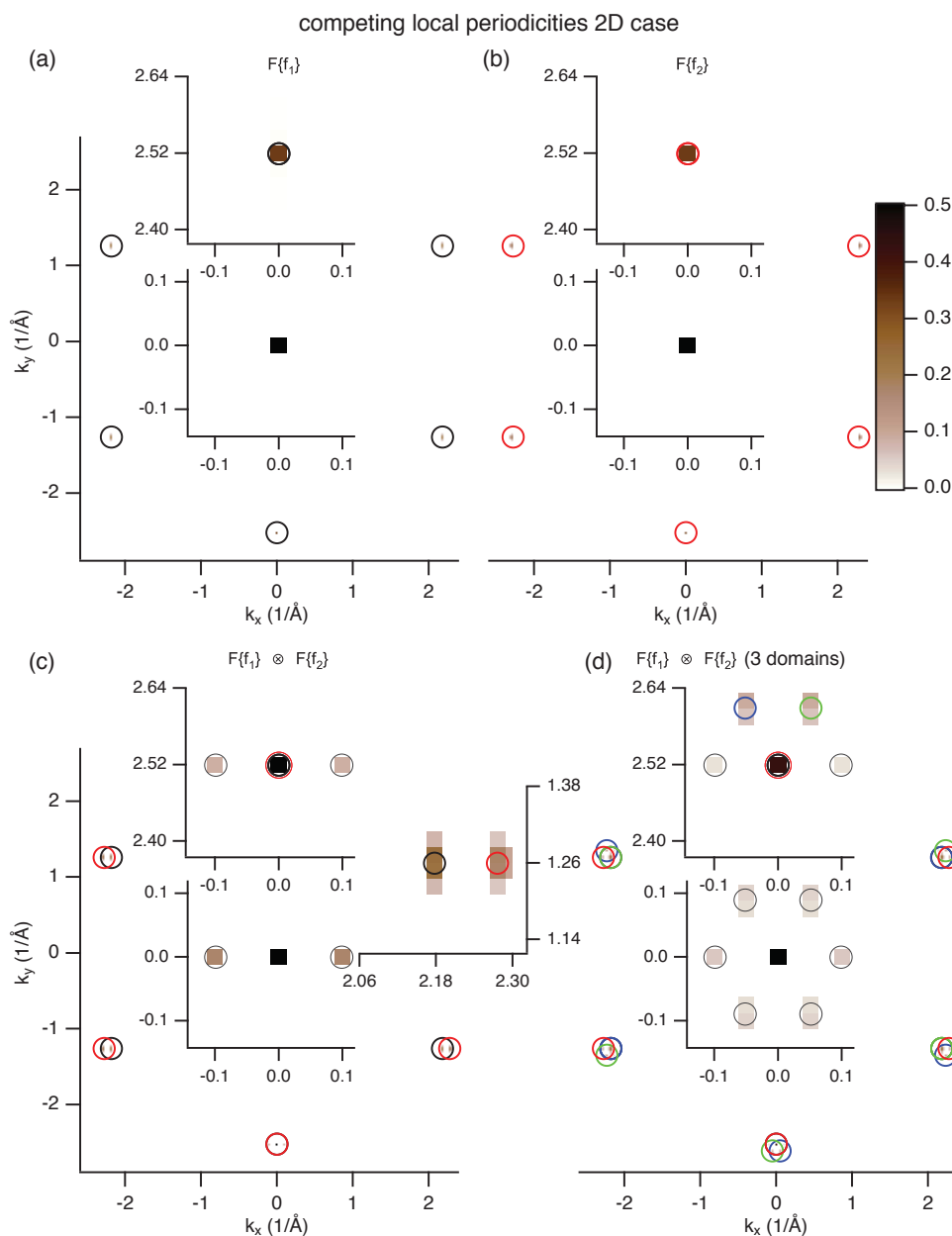


Figure 3.9: (a) and (b) Fourier coefficients for the truncated bulk lattice (\mathbf{b}_1 and \mathbf{b}_2) and the surface layer lattice (\mathbf{b}'_1 and \mathbf{b}'_2), respectively. The intensity is normalized to the zeroth order component and mapped with the colors scale included in the figure. The peaks are very narrow and therefore partly marked by circles around them. The regions around the origin and the first reciprocal lattice point in the vertical direction are magnified in the insets. (c) Convolution of (a) and (b). Here insets show magnifications around the origin and around two first order lattice spots. For this particular domain orientation, one strong Fourier coefficients and two weak ones are found close to one of these points and two strong ones close to the other. (d) Sum of convolution of (a) and (b) for the three possible domains on the surface.

Chapter 4

Synthesis of single-layered transition metal dichalcogenides

This chapter describes methods employed for the growth of SL TMDCs. STM measurements showing morphology changes during the synthesis are presented. Crystal structure is discussed based on LEED and STM investigations. Finally, the morphology of SL TaS₂/Au(111) grown using two different techniques is compared and discussed.

4.1 General growth procedure

Most of the research on 2D TMDCs has been performed on mechanically exfoliated samples [26, 28, 47, 108]. This approach, however, results in small flakes ($\approx 10 \mu\text{m}$) with varying number of layers and random orientations. Such samples are suitable for local techniques, such as electronic transport or optical measurements, but not for ARPES, which probes a large area defined by the light spot size ($\approx 200 \mu\text{m}$). Further, transfer methods may lead to a surface contamination. Recently, it was shown that large-area samples can be grown on a sapphire substrate using a CVD approach [109]. Nevertheless, an insulating substrate hinders ARPES measurements due to charging problems.

In order to synthesize the samples suitable for the envisioned ARPES studies, we adapted a method of metal deposition under an H₂S pressure, originally developed for the growth of MoS₂ nanoislands [110]. Modifications of the above method enabled us to grow high-quality samples, covering a large area of the substrate. This approach turned out to be very robust, resulting in successful growth over a large parameter space. Furthermore, the growth of multiple material systems – including MoS₂, WS₂ and TaS₂ on the Au(111), Ag(111) and graphene/SiC substrates – points to the method’s broad applicability.

Prior to SL TMDC growth, the Au(111) and Ag(111) substrates were prepared by standard UHV cleaning procedure: sputtering in a Ne atmosphere followed by annealing the substrate up to 850°C. Graphene/SiC substrates were annealed up to 300°C to remove physisorbed species that may have collected during exposure to air. During the growth, H₂S gas was introduced into the UHV chamber through a home-build nozzle situated ca. 1 cm from the substrate, which locally increased the pressure directly above the surface. Transition metals were evaporated through an electron-beam evaporator while the chamber was backfilled with an H₂S pressure in the range of $2 \times 10^{-5} - 5 \times 10^{-6}$ mbar. After deposition, samples were annealed up to 450 – 700 °C. Cycles of deposition and annealing were repeated until the desired coverage was achieved, which was monitored by STM in-between the cycles. In the following sections, we refer to this synthesis procedure as the evaporator method. Optimized growth parameters for SL TMDCs on Au(111)

can be found in Refs. [111–113]. The growth of WS₂ on Ag(111) was performed using the same parameters as in the case of WS₂/Au(111). Van der Waals epitaxy of SL MoS₂ on graphene/SiC is described in Ref. [114].

Despite excellent growth of SL TMDCs on these substrates we endeavored to improve the growth process and made progress on a technique that involved dosing H₂S gas through a hot Ta filament. Preliminary results [112] indicated that SL TaS₂ grown with this method exhibited domains of larger size. However, further studies that go beyond the scope of this thesis are still needed. We hypothesize that in this case H₂S volatilized TaS_x species that precipitated on the substrate.

Determination of the grown phase (1H or 1T) of SL TMDCs is problematic based solely on STM or LEED measurements. Nonetheless, band structures differ substantially for those two phases, according to DFT calculations. ARPES results presented in Chapter 5 revealed that all of the TMDCs discussed in this work crystallize in the 1H phase.

4.2 MoS₂ on Au(111)

A schematic of the growth procedure used for the synthesis of SL MoS₂ on Au(111) is depicted in Fig. 4.1(a). We find that changing the growth parameters, such as the H₂S pressure or the substrate temperature during the deposition, enables one to control the morphology of the growing layer. It was shown that Mo dosed on Au(111) in UHV nucleate preferentially on the bridge positions of the herringbone domain boundaries [110]. This allowed us to use the surface reconstruction as a pattern for the synthesis of well-defined arrays of triangular MoS₂ nanoislands [110]. Such an interesting morphology requires the synthesis to be performed under a low pressure of H₂S (ca. 10⁻⁷ mbar) to prevent a complete lifting of the reconstruction, and relatively low temperature (400°C) to reduce the Mo mobility on the surface. The growth of continuous films requires, on the other hand, increasing the Mo mobility by raising the temperature. However, Mo-Au alloying greatly increases for depositions carried out at higher temperatures [115], which might result in decreasing the quality of the grown film. We circumvent this problem by maintaining an H₂S atmosphere during the whole growth process, in order to prevent the surface from alloying. The cycles of deposition and annealing were found to produce samples fulfilling the desired criteria of quality and coverage.

The morphology of SL MoS₂ during the growth is presented in Fig. 4.1. The growth starts with formation of relatively large MoS₂ islands with triangular and truncated hexagonal shapes, as seen in Fig. 4.1(c). Such islands are oriented with (0001) basal plane of MoS₂ parallel to the Au surface and are seen to be distributed over the entire Au surface, which in this case reflects a total SL MoS₂ coverage of ca. 0.3 ML. The high resolution STM image presented in Fig. 4.1(b) reveals the atomically resolved lattice and the moiré structure of MoS₂. Only the S atoms in the topmost layer of this S-Mo-S trilayer structure are imaged by STM and they appear as bright protrusions in the STM micrographs [83]. The distance between these bright protrusions is measured to be 3.2(0.4) Å, which agrees with the distance of 3.15 Å expected for S atoms in the topmost layer. The incommensurability of the Au lattice (2.88 Å) and MoS₂ lattice (3.15 Å) gives rise to a moiré structure that manifests itself on the (0001) basal planes of MoS₂ as clearly visible protrusions in a hexagonal pattern with a periodicity of 32.8 Å (denoted by the double-headed arrow in Fig. 4.1(b)). Further attempts to increase the size of these islands by increasing the Mo coverage did not lead to a more uniform SL MoS₂ coverage, and it was not possible to increase the annealing temperatures due to severe alloying of the Mo and Au that

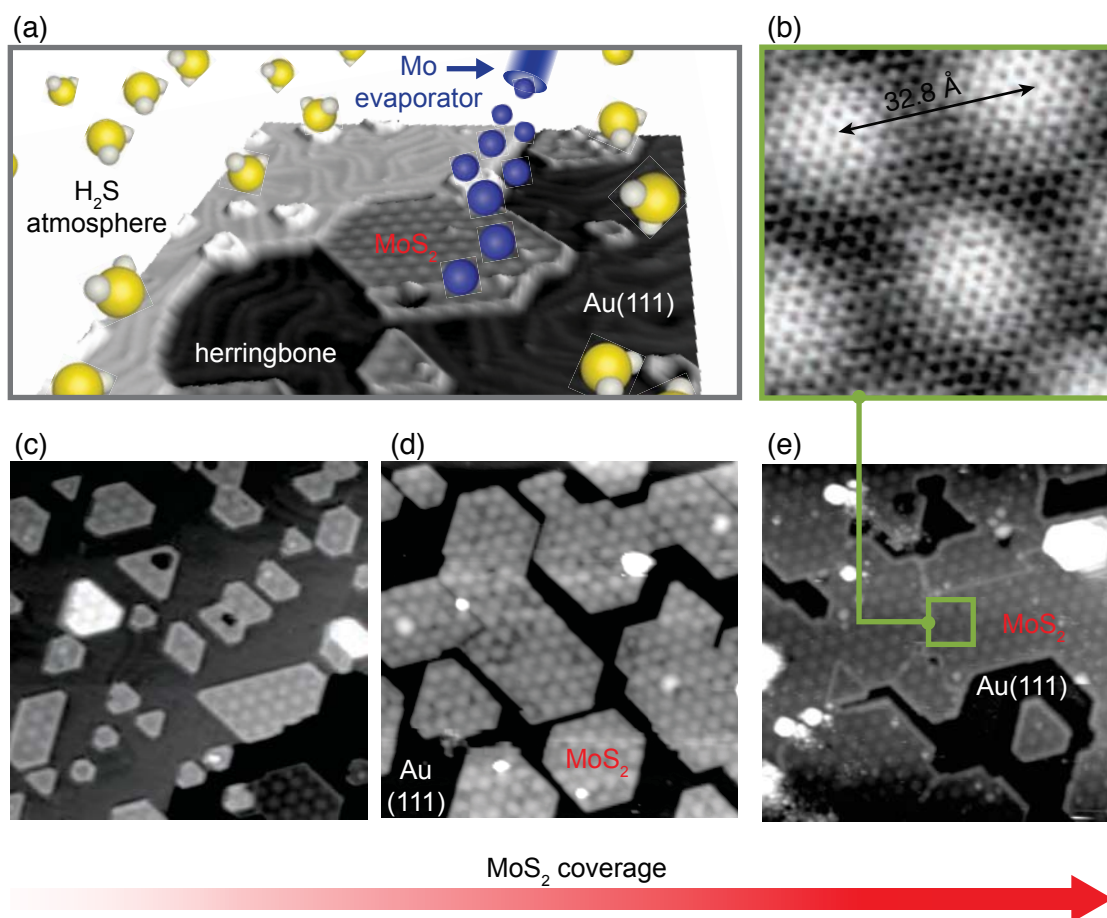


Figure 4.1: (a) Schematic depicting the process by which SL MoS₂ nanoscale islands are grown on Au(111). Mo is evaporated onto the Au surface in a H₂S atmosphere. Following Mo deposition, the surface is annealed while the H₂S pressure is maintained. (b) High-resolution STM image of the moiré lattice of MoS₂ within the area demarcated by the green square in (e). The double-headed arrow marks the moiré periodicity. (c) STM image acquired after one growth cycle showing hexagonal islands of SL MoS₂ (coverage is ≈ 0.3 ML). Continued growth leads to coalescence of islands and a gradual increase in coverage as shown for (d) ≈ 0.6 ML and (e) ≈ 0.8 ML. The STM images are 65 nm \times 65 nm except for the atomically resolved STM image in (b) that is 6 nm \times 6 nm. Imaging parameters are approximately 1.13 nA and -0.15 V.

occurs irrespective of the H₂S pressure. Instead of increasing the temperature and Mo coverage in one step, the key to increasing the coverage of high quality SL MoS₂ involves repeated cycles of Mo evaporation and annealing in H₂S. This results in islands merging together at a MoS₂ coverage of ca. 0.6 ML as shown in Fig. 4.1(d). Continued cycling of the growth process leads to a further increase in coverage (ca. 0.8 ML) and the formation of a nearly contiguous SL of MoS₂ (see Fig. 4.1(e)).

The structural details of the ≈ 0.8 ML coverage MoS₂ sample are further studied by LEED in Fig. 4.2(a). A sharp hexagonal diffraction pattern with satellites surrounding each main diffraction spot is observed, suggesting a clean, ordered, and extended SL of MoS₂. The satellite spots are consistent with the moiré pattern observed in the STM images, indicating a large-area presence of this pattern. To highlight the origin of each diffraction spot, we have added reciprocal lattice vectors in Fig. 4.2(a). The main diffraction spots correspond to the MoS₂ lattice while the satellites are associated with the moiré, in analogy to the case discussed thoroughly in Chapter 3.

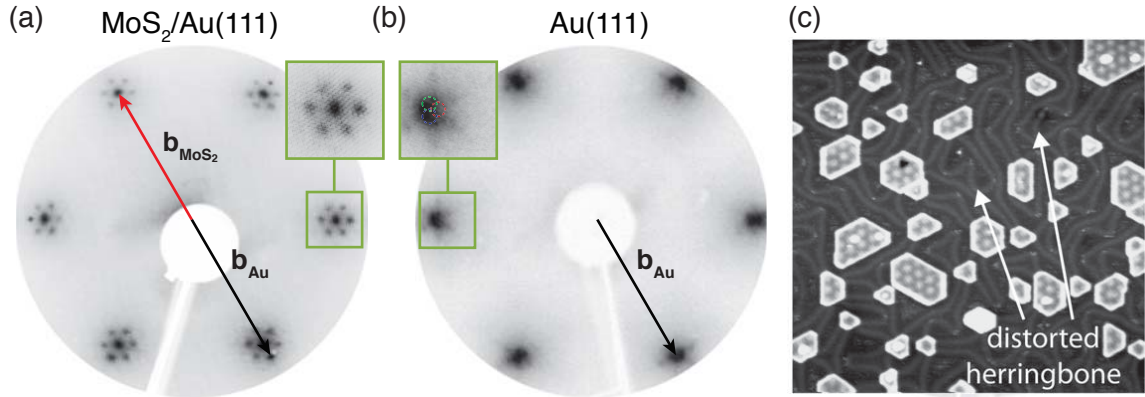


Figure 4.2: LEED patterns acquired using electrons with a kinetic energy of 114 eV for (a) a high coverage (ca. 0.8 ML) MoS₂ on Au sample and (b) a clean Au(111) surface. The Au and MoS₂ reciprocal lattice vectors are shown. In panel (a) the MoS₂ on Au sample reveals six sharp first order spots in a hexagonal pattern and around each of these spots are six satellite spots also arranged in a hexagonal pattern. The inset shows the details of one first order spot. In panel (b) a similar LEED image is shown for the clean Au(111) sample. The inset shows the first order spots for three domains arising from the herringbone reconstruction, as discussed in Chapter 3. (c) STM image of the surface after one growth cycle of MoS₂ in which distortions of the native herringbone are already visible. Image parameters: 100×100 nm, 0.65 nA, -1.25V

A separate LEED image of the clean Au(111) surface is shown for comparison in Fig. 4.2(b). In this case, the hexagonal arrangement of the satellite spots, compared to the high coverage MoS₂ sample, is rotated with respect to one another by 30° (see insets of Fig. 4.2(a)-(b)). Since both diffraction patterns are acquired using electrons with a kinetic energy of 114 eV, the absence of the Au satellite features in the high coverage MoS₂ LEED data of Fig. 4.2(a) suggests that the herringbone reconstruction is lifted underneath the MoS₂ adlayer. These same Au spots are also absent in LEED measurements of the MoS₂ sample acquired at different kinetic energies. Indeed, the lifting of the native Au reconstruction is also supported by the STM image in Figure 4.2(c) which shows triangular looplike distortions of the regular herringbone reconstruction even after only one MoS₂ growth cycle. These perturbations are similar to previously reported STM data of Au thin films grown on Ru(0001) which suggest that such triangular-like structures are amenable to relieving strain in stacked hexagonal layers [116]. Indirect evidence of this lifting is seen for a small number of MoS₂ islands that appear brighter than the rest and still display a moiré pattern, such as the brighter island in Fig. 4.1(c). This increase in apparent height is exactly consistent with the 2.3 Å height of an extra layer of Au atoms beneath the SL MoS₂ island [117]. Such small extra Au islands are expected to be generated by the lifting of the herringbone reconstruction, as this reconstruction has a higher density of atoms (4.5%) in the first layer compared to the truncated bulk surface [118]. Interestingly, some of the grown islands exhibit characteristic large defects appearing as dark pits in Fig. 4.1(c). A combined STM and AFM study has revealed that these are regions of free-standing MoS₂, lacking the Au support due to the redistribution of the surface atoms [119].

Our STM images of the high coverage samples frequently reveal additional features atop SL MoS₂, which are evident from Fig. 4.3. We assign the irregularly shaped clusters highlighted by the green circle in Fig. 4.3(b) to amorphous Mo clusters, which may result from insufficient sulfurization during the growth cycles. Perhaps more interesting is the feature marked by the blue circle, which shows the formation of a BL MoS₂ island. A STM image of such an island is shown in Fig. 4.3(d). In contrast to the SL islands, the basal plane of the BL appears flat

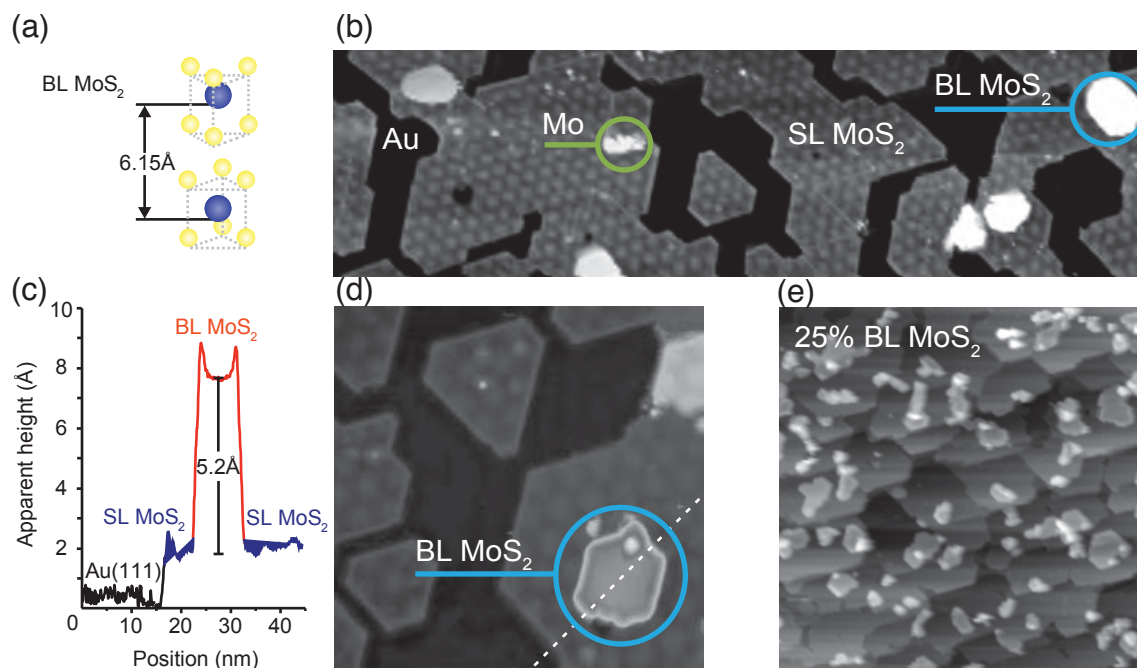


Figure 4.3: (a) Model illustrating the bulk interlayer spacing of 6.15 \AA in the 2H-stacking of S-Mo-S layers. (b) STM image of ca. 0.8 ML MoS₂ on Au(111). Additional features are observed, specifically amorphous Mo clusters (green circle) and small islands of BL MoS₂ (blue circle). Image parameters: $171 \text{ nm} \times 49 \text{ nm}$, 0.27 nA , and -1.23 V . (c) Apparent height of BL MoS₂, relative to the underlying SL MoS₂, extracted from the line profile acquired along the white dashed line in the adjacent STM image. (d) STM image highlighting the difference in apparent height of the BL MoS₂ compared to the surrounding SL MoS₂ areas. Image parameters: $36 \text{ nm} \times 34 \text{ nm}$, 0.40 nA , and -1.16 V . (e) STM image of MoS₂ on Au(111) with an estimated BL MoS₂ coverage of 0.25 ML . Image parameters: $175 \text{ nm} \times 175 \text{ nm}$, 0.19 nA , and -1.16 V .

in the center of the island; a moiré is absent, and it is difficult to obtain atomic resolution. The apparent height of the BL islands relative to the underlying SL islands is $5.2(0.3) \text{ \AA}$, as indicated by the line profile in Fig. 4.3(c). This value is comparable to the bulk interlayer spacing of 6.15 \AA in the 2H-stacking of S-Mo-S layers [120] (see Fig. 4.3(a)), supporting the assignment of these features to BL and not multilayer islands. As the number of growth cycles is increased, we foster the formation of more and larger islands of BL MoS₂. In the STM image shown in Fig. 4.3(e), the BL regions appear brighter than the surrounding darker SL MoS₂ film. Upon close inspection of the STM image, the SL MoS₂ still manifests a moiré pattern that is unaffected by the presence of the BL MoS₂ islands. Here, the BL MoS₂ covers an estimated ca. 25% of the surface. The contours of the BL MoS₂ islands are notably more irregularly shaped than SL MoS₂ islands for a similar coverage; see Fig. 4.1(c) for comparison. Given that in BL regions, the interaction between the second layer of the BL MoS₂ and the underlying SL MoS₂ film is weaker than the interaction between the SL MoS₂ and the underlying Au substrate, we might expect to see growth of islands with many different rotational domain orientations. The irregular shapes of the BL islands suggests that such islands may not seamlessly merge together during subsequent growth cycles and will indeed make the synthesis of large domains of high quality multilayers of MoS₂ more challenging.

The STM images also reveal the presence of distinct line defects, as shown in Fig. 4.4(a). These line defects are boundaries between two opposite rotational domains of the 3-fold symmetric MoS₂ lattice on the unreconstructed Au(111) surface lattice. Similar line defects have been

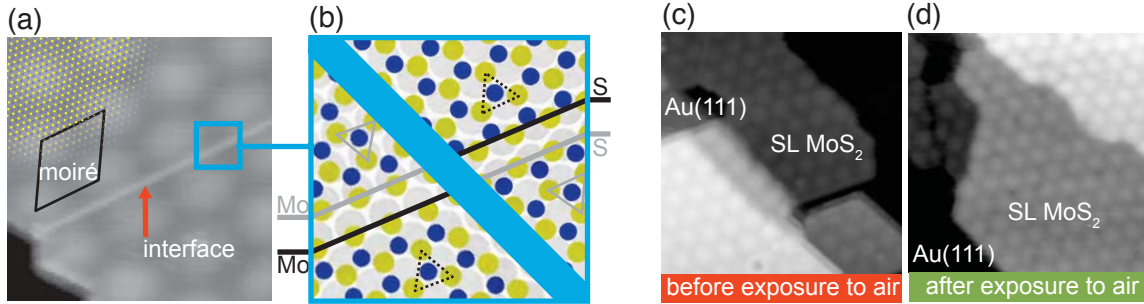


Figure 4.4: (a) STM image of a line defect at the boundary between rotational domains. STM imaging parameters: $10 \text{ nm} \times 10 \text{ nm}$, 0.52 nA , and -0.88 V . The moiré unit cell and ball model are overlaid to highlight the atomic character of the line defect. (b) Schematic of the line defect arising from the coalescence of two oppositely oriented domains. The absolute orientation of the domains could not be determined from the STM data, and therefore both possible scenarios for mating edges are shown and separated by the light blue diagonal line. The Mo-edge and S-edge are simply labeled Mo and S, respectively. The dashed (black) and solid (gray) outlined triangles are added to illustrate the two different rotational domains. Ball model color code: yellow: S, blue: Mo, gray: Au. STM images of SL MoS₂ samples acquired at room temperature (c) before and (d) after exposure to air. The surface quality is essentially the same after the exposed surface is gently annealed to ca. 200°C . Imaging parameters: (c) $35 \text{ nm} \times 35 \text{ nm}$, 0.33 nA , and 0.78 V and (d) $35 \text{ nm} \times 35 \text{ nm}$, 0.28 nA , and 1.00 V .

observed in scanning transmission electron microscopy measurements of CVD-grown MoS₂ on SiO₂ [121]. The MoS₂ islands are either terminated in the $\langle 10\bar{1}0 \rangle$ or $\langle \bar{1}010 \rangle$ directions. These terminations are referred to as the Mo-edge and S-edge, respectively. Joining islands with the same domain orientation, which is equivalent to the meeting of two different edge types, will result in the formation of a continuous SL of MoS₂. However, structural domain boundaries arise when domains of differently oriented MoS₂, or correspondingly the same edge types, meet during the growth process as shown in Fig. 4.4(a). It is not clear from the STM images which type of interface is present for each individual line defect as only the upper layer of S atoms is imaged by STM [122]. Hence, both possible interfaces are shown in Fig. 4.4(b) separated by a light blue line. The 60° rotational domains are neither expected to influence the LEED pattern (although they would affect the relative spot intensities), nor would they have an effect on the overall electronic structure of SL MoS₂ due to the hexagonal symmetry of the reciprocal lattice. However, the presence of line defects suggests that domains rotated by 60° coexist in our sample, and this is of crucial importance as it implies that the high symmetry points \bar{K} and \bar{K}' in the SBZ from different rotational domains coincide in laterally averaging techniques such as ARPES.

It is worth mentioning some interesting properties of the MoS₂ edges. While the basal plane is quite inert, the edges are highly catalytically active and of great interest for industrial processes such as hydrodesulfurization [123]. The under-coordinated edges are also predicted to be metallic [124] in contrast to the semiconducting basal plane. It is likely that a relatively strong interaction between the SL MoS₂ and the Au(111) substrate is mainly restricted to the edges. This hypothesis is corroborated by the unusual mobility of Au nanoislands grown on the bulk MoS₂, which can be moved using a STM tip [125]. We have not observed a similar behavior for SL MoS₂ nanoislands grown on Au(111). Finally, the inertness of the basal plane makes the SL MoS₂ stable under ambient conditions. Fig. 4.4(c)-(d) present STM images of a sample before and after exposure to air for a couple of hours, respectively. No major modifications to the surface were found and the samples could be cleaned of adsorbates by gentle annealing (200°C).

4.3 MoS₂ on graphene/SiC

One of the consequences of reduced dimensionality in SL TMDCs is the reduced dielectric screening leading to the giant exciton binding energies (ca. 1 eV) [126, 127]. This effect, however, might be greatly diminished by the presence of a metallic substrate. Furthermore, the electronic transport measurements and device applications require the substrate to be insulating to some extent. Using the growth techniques already described, we achieve *in situ* van der Waals epitaxy of SL MoS₂ on graphene/SiC which overcomes above issues and elegantly removes the need for additional transfer steps to change substrate. Van der Waals epitaxy relies on the relatively weak coupling between the adjacent 2D materials and does not require that their crystal lattices match. This is in contrast to standard epitaxy methods. Graphene has proven to be a suitable template for such an approach, as exemplified by the successful growth of other low dimensional systems on graphene such as III-V semiconductor nanowires [128] and thin films [129] as well as topological insulators [130]. MoS₂ and other TMDCs have been grown by CVD methods using suitable carrier gases in furnace systems on either CVD graphene on copper [131] sapphire [132] or graphene transferred onto SiO₂ [133]. Alternatively, high-quality epitaxial graphene on SiC substrates have proven to be a good template for van der Waals epitaxy of MoS₂ and WSe₂ in CVD furnaces [134, 135].

The growth of MoS₂ on graphene/SiC started with preparation of the substrate. This was performed by Jill Miwa in a separate UHV chamber by direct current annealing of SiC under a mild flux of Si [136]. Graphene (G) grown using this approach is decoupled from the substrate by a layer of carbon atoms which saturate the dangling bonds of Si [137]. This layer is commonly referred as a buffer layer. The STM image in Fig. 4.5(a) shows the clean G/SiC surface along with the characteristic SL graphene lattice, which can be atomically resolved (see inset in Fig. 4.5(a)). We observe also the regions of buffer layer in our samples. The presence of such buffer layer areas is a key element in the growth of MoS₂, which we follow in its initial stages in Figures 4.5(b)-(f).

Evaporation of Mo was carried out using a Mo flux and duration that gives the submonolayer Mo coverage shown in the STM image in Fig. 4.5(b). Without H₂S, the Mo appears as small, bright, rounded clusters. The G/SiC substrate is held at room temperature during evaporation, which ensures a low Mo mobility, thereby preventing the formation of large Mo aggregates. Interestingly, on the graphene areas, the Mo clusters are found to mainly decorate the edges of the graphene. This is in sharp contrast to the dense film of Mo clusters that can be seen inside the buffer layer regions (denoted B in Fig. 4.5(b)), thereby making the buffer layer easier to distinguish from graphene. The preference for adsorption on the buffer layer is ascribed to its higher reactivity, which has also been confirmed via molecular adsorption patterns observed on G/SiC [138]. In a first attempt, the Mo-decorated surface was annealed for 1 h at ca. 800°C in a H₂S pressure on the order of 10⁻⁵ mbar. This promotes the growth of nanosized MoS₂ islands, which are located predominately in the buffer layer regions in this initial growth stage, as seen in Fig. 4.5(c). The STM image in Fig. 4.5(d) shows an atomically resolved MoS₂ island where the atomic spacing is found to be 3.1(0.3) Å. This island can be seen to already extend onto a single-layer graphene area. Repeating such a growth cycle leads to a gradual increase in the size of islands, as seen in Fig. 4.5(e). The island structures and edge shapes deviate substantially from the hexagonal structure and straight edges expected for a free-standing island in thermodynamic equilibrium [139]. Such irregular edges have also been observed for MoS₂ nanoclusters grown on a highly ordered pyrolytic graphite (HOPG) surface, where their occurrence was attributed to defects that act as pinning sites during the growth [140]. The elevated temperatures during growth are likely to increase the mobility of these defects such that they migrate to the edges

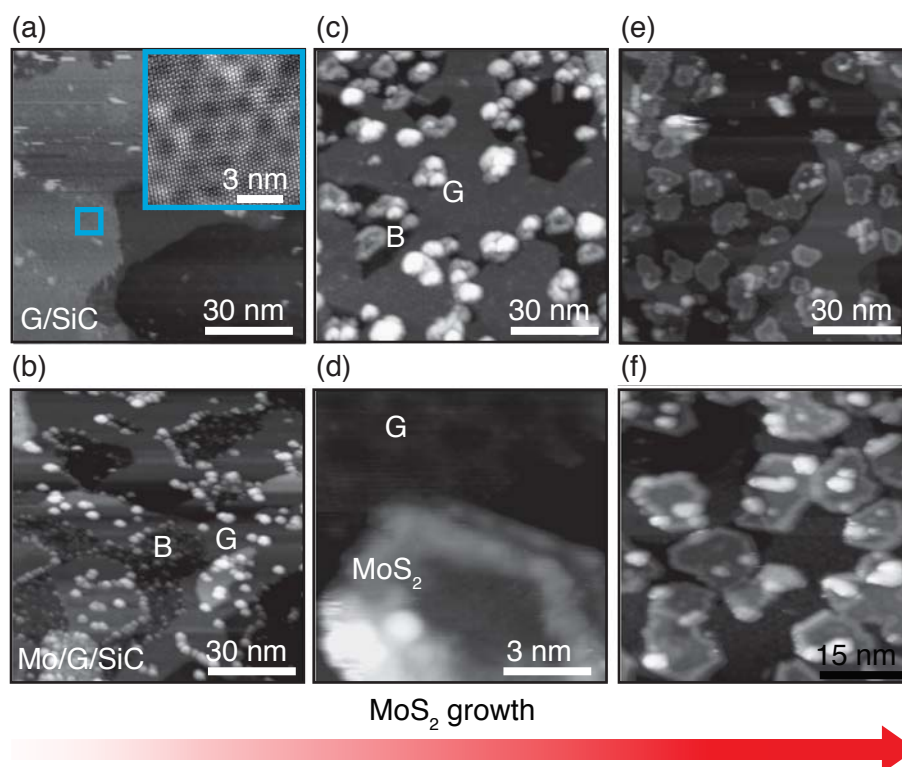


Figure 4.5: (a) STM image of the graphene/SiC (G/SiC) substrate. Inset: Atomic resolution image of the graphene lattice within the area marked by the blue square. (b) Sample surface after evaporation of atomic Mo (Mo/G/SiC). Buffer layer (B) and SL graphene (G) areas are distinguishable via the different distribution of adsorbed Mo. (c) MoS₂ nanoislands grown in B regions after annealing at 800°C in a H₂S atmosphere. (d) Atomic resolution image of a 6 nm wide MoS₂ island, which has grown over a G region. (e,f) Larger MoS₂ islands on graphene after an additional cycle of Mo evaporation and H₂S annealing at 800°C. The image in (f) shows merged islands and atoms inside islands in greater detail. The STM imaging parameters are: (a) -1nA and -0.88 V, (b) -0.9 nA and -1.07 V, (c) -0.9 nA and -0.88 V, (d) -0.9 nA and -0.88 V, (e) -0.5 nA and -1.25 V, (f) -0.6 nA and -0.91 V.

of the islands and force them to assume an irregular shape. Furthermore, due to the relatively weak interaction between MoS₂ and our graphene substrates, many rotational variants of the MoS₂ islands nucleate. Due to the irregularly shaped edges, it is difficult for these differently rotated islands to coalesce, as evidenced in Fig. 4.5(f), where the edges of neighboring islands are seen to line up but not merge seamlessly and, instead, form noticeable domain boundaries. Bright, rounded features are observed on top and around the edges of the MoS₂ islands, which are excess nonsulfurized Mo or partly sulfurized amorphous MoS₂. Their adsorption is presumably facilitated by the higher reactivity at the edges and defect sites in the MoS₂ or in the underlying substrate.

Continuation of the cycled growth leads to extended SL MoS₂ areas as seen for a sample with a coverage of 0.55 ML in Fig. 4.6(a). In contrast to the MoS₂ nanoislands in Fig. 4.5(c), which were mainly localized in the buffer layer areas, the SL MoS₂ is observed to spread across the graphene areas. Since bare buffer layer regions are scarce compared to bare graphene areas, the higher coverage of SL MoS₂ ensures that our samples consist predominantly of MoS₂ on graphene. While clear atomically resolved images of the structure inside the basal plane of MoS₂ could be achieved for the nanoislands, we find it harder to obtain atomic resolution inside the layers in Fig. 4.6(a), which may be due to electronic effects associated with the underlying

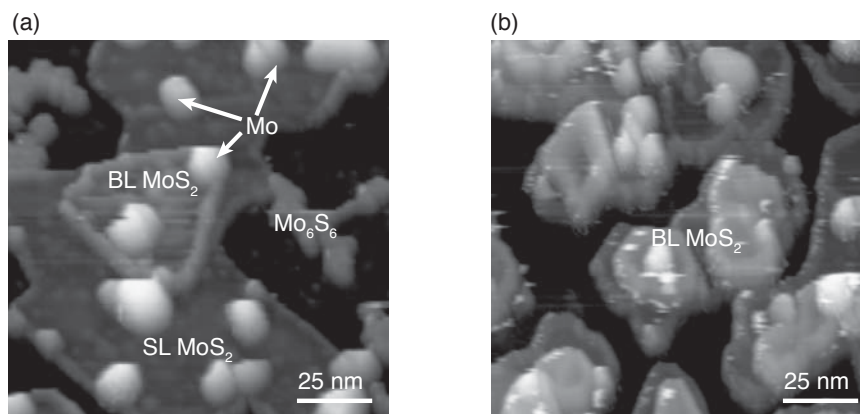


Figure 4.6: STM images of MoS₂ on G/SiC with a SL MoS₂ coverage of approximately (a) 0.55 ML and (b) 0.85 ML. In (a), bare SL MoS₂ areas coexist with metallic Mo clusters (see arrows) and a BL MoS₂ island. Structures that resemble Mo₆S₆ nanowires are seen on graphene areas. The higher coverage sample in (b) has fewer bare SL MoS₂ areas and a higher number of BL MoS₂ islands. The STM imaging parameters are: (a) -1.75 nA and -0.52 V, (b) -1.1 nA and -0.94 V.

substrate. A smaller BL MoS₂ island appears along with Mo clusters on top of the SL MoS₂. We can distinguish SL and BL MoS₂ by their apparent heights in STM, which we measure to be 8(2) and 17(2) Å, respectively. At the coverage of 0.55 ML, we estimate that 6% is BL MoS₂, which appears to be the limiting case where the presence of BL MoS₂ regions does not influence the laterally averaged electronic structure (on a submillimeter length scale) of the sample measured by ARPES, which we discuss in Section 5.2. Features that lack well-defined structure are observed on bare graphene areas. These may be bundles of Mo₆S₆ nanowires similar to those previously observed on HOPG [141] and Cu(111) [142]. Increasing the coverage to 0.85 ML using additional growth cycles leads to 40% BL MoS₂, which is seen in Fig. 4.6(b). The excess metallic Mo clusters act as seeding points for growth of additional MoS₂ layers. Keeping their concentration low, that is, keeping the Mo flux low during evaporation, is the key to favor SL MoS₂ growth. We point out here that in contrast to the growth of MoSe₂ films on G/SiC, where co-deposition of atomic Mo and Se using a MBE approach results in MoSe₂ after annealing in a single growth cycle [143, 144] the reaction between Mo and S from the H₂S gas source necessitates the cycled approach with very gentle Mo deposition in each cycle. Otherwise, we found that metallic Mo assembles in large clusters, which were either difficult to sulfurize within the limits of the experimental setup or seeds on already nucleated MoS₂ islands leading to multilayer MoS₂.

4.4 WS₂ on Au(111) and Ag(111)

The process of WS₂ growth on Au(111) largely resembles the growth of MoS₂ discussed in the previous section. For that reason, we discuss the synthesis of WS₂/Au(111) very briefly and the rest of this section is dedicated to the synthesis of WS₂ on Ag(111).

The synthesis of WS₂ films is illustrated by STM images presented in Fig. 4.7. As in case of MoS₂, the growth starts with triangular islands (Fig. 4.7(a)) which gradually merge together forming a high-coverage film (Fig. 4.7(b)). The average apparent height of the grown film extracted from STM profiles yields 3.2(0.7) Å, in agreement with previous investigations of nanoislands [145]. Domain boundaries suggest a presence of two domains formed by joining the islands with the

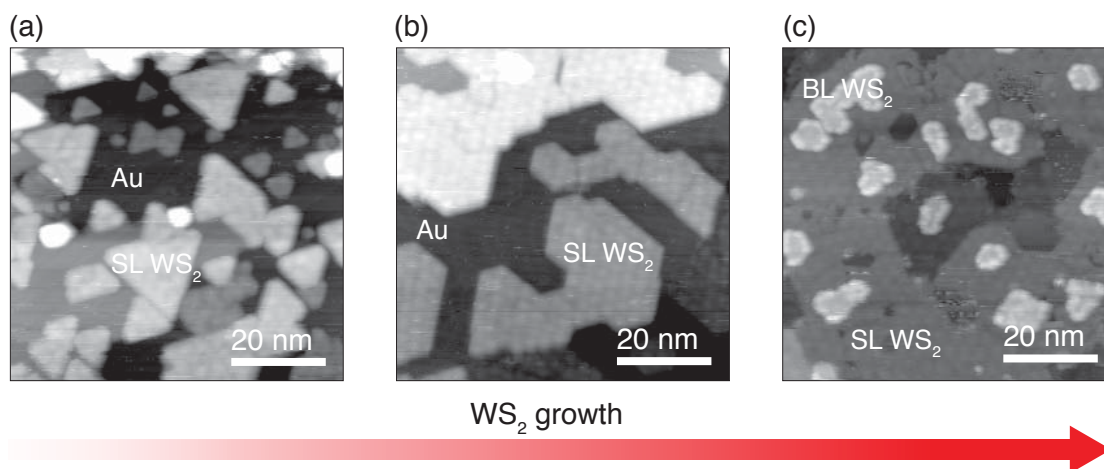


Figure 4.7: STM images of WS_2 on $\text{Au}(111)$ with a SL WS_2 coverage of approximately (a) 0.4 ML, (b) 0.75 ML and (c) 1.15 ML. In (a), WS_2 crystallizes predominantly in form of triangular nanoislands. The higher coverage sample in (b) is formed from larger polygons. The dislocation lines might be a results of the presence of two rotational domains. BL regions are clearly seen in (c) as amorphous shapes at bright contrast. The STM imaging parameters are: (a) 0.49 nA and 1.06 V, (b) 0.58 nA and 1.16 V, (c) 0.61 nA and 0.74 V.

same edge termination. After the coverage is higher than ca. 0.7 ML, the BL starts to nucleate in a form of shapeless islands (Fig. 4.7(c)). Interestingly, tungsten clusters, in contrast to molybdenum, do not show a characteristic nucleation at a specific site of the herringbone reconstruction [145]. This suggests a higher mobility of tungsten on the $\text{Au}(111)$ surface and may lead to different size distribution of the WS_2 nanoislands. However, this does not hinder the growth of large-area films aligned with the substrate. The lattice mismatch between WS_2 and $\text{Au}(111)$ leads to formation of a moiré pattern with periodicity of $32.7(0.6)\text{\AA}$ and matches well the one obtained for $\text{MoS}_2/\text{Au}(111)$. This is not surprising as bulk MoS_2 and WS_2 have a very similar lattice constant [146, 147]. The formation of the moiré pattern can be followed by LEED measurements taken at different WS_2 coverages, as shown in Fig. 4.8. For a coverage of ≈ 0.15 ML, two concentric hexagonal patterns dominate (Fig. 4.8(a)). Based on the length of the unit cell vectors, the outer and inner hexagons can be assigned to $\text{Au}(111)$ and SL WS_2 , respectively. The measured reciprocal unit cell vector ratio $b_{\text{Au}(111)}/b_{\text{WS}_2}=1.09(0.02)$ is in excellent agreement with the crystal unit cell vector ratio $a_{\text{WS}_2}/a_{\text{Au}(111)}=1.1$. The absence of a moiré at this low coverage can be explained by the fact that the growth starts with the formation of small islands, which are initially too small to establish a moiré pattern. In the case of a coverage of ≈ 0.3 ML shown in Fig. 4.8(b), the moiré pattern is clearly observed in addition to the spots caused by the separate reciprocal lattice vectors of $\text{Au}(111)$ and WS_2 . Further increase of the coverage results in a vanishing contribution from bare Au regions and a more uniform intensity of the moiré spots (Fig. 4.8(c)). Finally, when BL regions starts to grow the moiré pattern fades away, as seen in Fig. 4.8(d). This is to be expected if the second layer grows in register with the first one, and neither of the layers is strained.

Au surface is quite inert towards the reaction with H_2S . Prolonged exposure at the elevated temperatures used for the growth results in a lifting of the reconstruction as discussed in Chapter 3. This is not the case for the $\text{Ag}(111)$ surface which can react with sulfur causing the growth of Ag_2S [148]. In order to study this process we exposed a clean $\text{Ag}(111)$ surface to a 10^{-5} mbar pressure of H_2S and annealed to ca. 600°C for 30 min, mimicking the growth conditions. STM images presented in Figs. 4.9(a)-(b) reveal the formation of domains with a

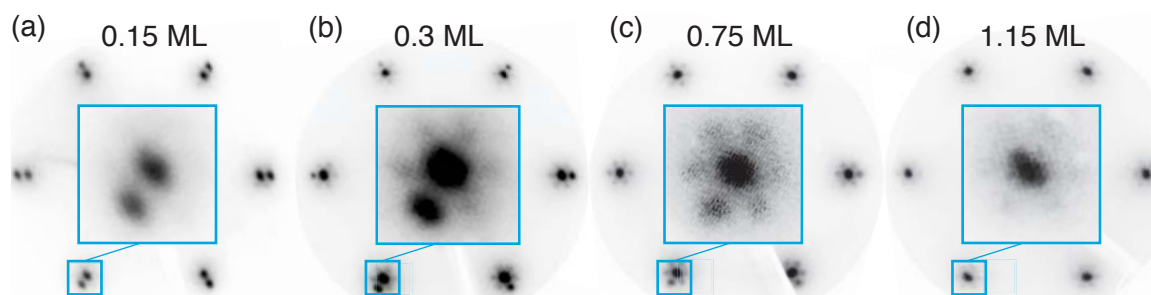


Figure 4.8: Evolution of the LEED pattern of WS₂/Au(111) for different coverage, as indicated in the panels. The insets shows magnified part of an image around the first order spot. Data taken at 118 eV and 114 eV for (a)-(b) and (c)-(d), respectively.

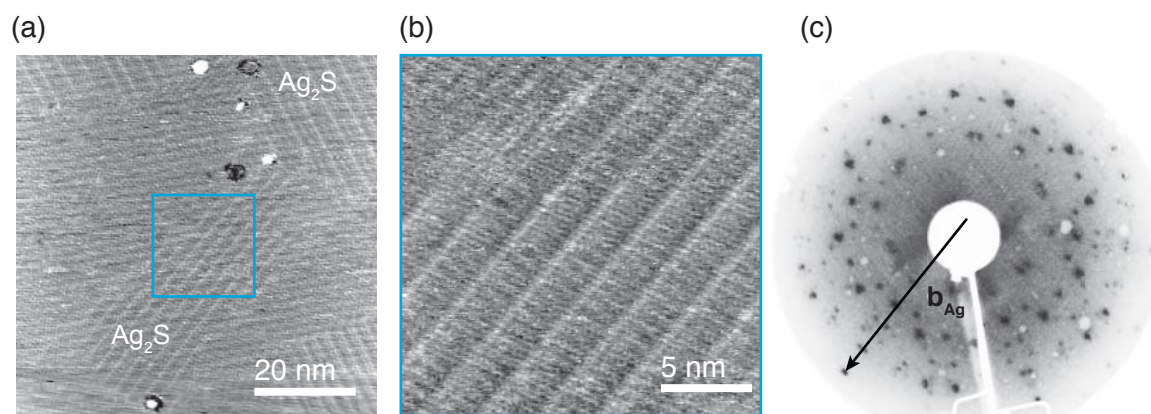


Figure 4.9: (a) STM image of Ag substrate after exposure to H₂S with marked Ag₂S domains. (b) Close-up of the area indicated in (a) by the blue square. The stripe-like pattern of the complex surface reconstruction, as discussed in the text. (c) Corresponding LEED image taken at 60 eV. The STM imaging parameters are: (a) 0.3 nA and 1.06 V, (b) 0.31 nA and 1.06 V.

stripe-like superstructure, possibly made of different phases of Ag₂S coexisting on the surface. The corresponding LEED pattern (Fig. 4.9(c)) resembles the complex $(\sqrt{39} \times \sqrt{39})R16.1^\circ$ structure in which the S atom arrangement and spacing is similar to (100) plane of γ -Ag₂S (the high temperature phase) [149]. A better empirical match to the observed LEED pattern was found with a $(\frac{3.67}{3} \frac{0}{3.5})$ structure, but even high-resolution STM analysis in previous studies has not been able to resolve the atomic structure in detail [150]. It is worth noting that this reconstruction do not conserve the density of Ag atoms relative to the clean surface [151]. This may lead to formation of defects visible in Fig. 4.9(a). We observed that annealing up to 700°C in UHV lifts the reconstruction and clean surface is recovered.

The growth of WS₂ on Ag(111) was performed with similar conditions to the samples synthesized on Au(111). While on Au(111) the shape the initial WS₂ nanoislands is primarily triangular (see Fig. 4.7(a)), there is no such preference on Ag(111) and the shape of the clusters resembles polygons (Fig. 4.12(a)).

Continuation of the growth leads to the formation of large domains, gradually covering the whole substrate area as illustrated in (Fig. 4.12(b)). We observed a presence of large (ca. 1 nm) defects on the basal plane of WS₂ patches, which were not observed for the growth performed on Au(111). However, higher order moiré and overall sharper spots were usually observed with LEED on WS₂/Ag(111) samples than on WS₂/Au(111). Also, the linewidth of the bands measured with ARPES was significantly lower in this case. These results suggest a

better crystalline order of WS₂/Ag(111) in comparison to WS₂/Au(111). In order to evaluate the defect concentration we performed STM analysis shown in Figs. 4.10(c)-(d). Fig. 4.10(b) presents the region on a sample where WS₂ is grown on a single terrace of the substrate. We fit a plane to the regions of bare Ag which is then subtracted from the data. The apparent height is calibrated according to the height of a single atomic step of Ag (2.4 Å). Data points corresponding to SL WS₂ are selected by discrimination of the apparent height ($0.25h_{\max} < h < 0.5h_{\max}$), as shown in Fig. 4.10(c). The histogram showing the distribution of the apparent height of those points is presented in Fig. 4.10(d). This distribution is evidently asymmetric with a visible shoulder towards lower values of apparent height. As domain boundaries fall outside the discrimination range, we conclude that this shoulder corresponds to the observed defects. By fitting the Gaussian profiles to the peaks corresponding to the basal plane and defect contributions we estimate that ca. 8% of the whole monolayer is defective, which is surprising in light of the other findings, described above, pointing to good crystalline order. We compare the results to the case of WS₂/Au(111) (Fig. 4.10(d)), analyzed in analogous manner. In this case the distribution seems to be symmetric and can be described with just a single Gaussian. It is unlikely that the effects of such a large defect concentration are not observed with ARPES and LEED. A possible explanation of those results is the hypothesis that defects observed with STM are pits in the substrated etched by the H₂S gas. The size of defects observed on sulfurized Ag(111) samples matches the size of defects observed on the basal plane of SL WS₂. We expect that high-resolution AFM measurements might be able to elucidate this effect, in analogy to the similar measurements performed for MoS₂/Au(111) [119].

The above analysis allows for a comparison between apparent heights of SL WS₂ grown on both Ag(111) and Au(111). The expectation value of the apparent height distribution on Ag (2.2(0.3)Å) seems to be smaller than on Au (2.5(0.4)Å). This result is consistent with DFT calculations predicting a smaller equilibrium substrate-overlayer spacing for MoS₂/Ag(111) in comparison to MoS₂/Au(111) [152, 153]. Nevertheless, a signal measured with STM is a convolution of topography and local density of states, so it cannot be directly compared to the real thickness of the layer. Furthermore, it was shown that the observed apparent height of MoS₂/Au(111) strongly depends on the applied bias [83].

Another important question concerning the SL WS₂ height is whether the substrate reconstruction is present underneath the grown film. For the growth on Au(111), the herringbone reconstruction seems to be heavily distorted on the bare Au areas (see Fig. 4.2(c)). Furthermore, in simulated STM images, the herringbone reconstruction is visible through a single layer of hexagonal boron nitride or three layers of NaCl(100) (more than 11Å from the topmost Au atoms) [98]. It was demonstrated experimentally with STM that the characteristic pattern of the herringbone reconstruction can be even observed for five-layer-thick NaCl films grown on Au(111) [154]. In case of low-coverage samples (ca. 0.3 ML) WS₂ grown on Ag(111) we observe the coexistence of a complex LEED pattern corresponding to the sulfur-induced surface reconstruction, as seen in Fig. 4.11(a). However, the reconstruction is completely lifted after annealing the sample up to 700°C in UHV (Fig. 4.11(b)). If the reconstruction was present underneath the SL WS₂ film, we would expect to observe changes in the moiré periodicity. No such modifications were observed and the moiré periodicity agrees well with the lattice constants difference between SL WS₂ and unreconstructed substrates, for both Au(111) and Ag(111) cases. These arguments lead us to the conclusion that probably there is no reconstruction present underneath the grown film.

We conclude this section with a discussion of the lattice constant in the grown SL WS₂. According to the band structure calculations, SL TMDCs can be altered significantly with even small changes in a lattice spacing [155]. It is predicted that just 1% of compressive strain can shift the

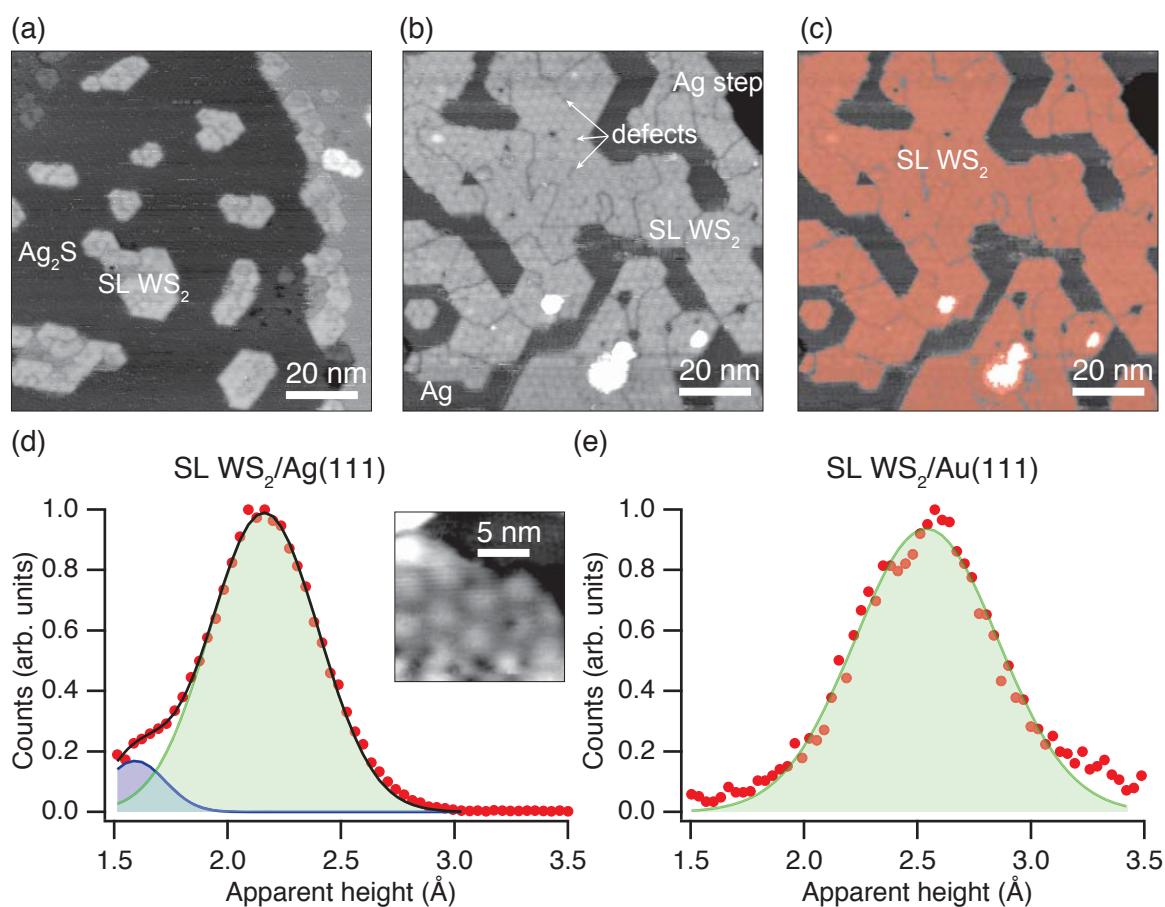


Figure 4.10: STM images of WS₂ on Ag(111) with a SL MoS₂ coverage of approximately (a) 0.15 ML and (b) 0.75 ML. (a), WS₂ crystallizes predominantly in form of polygons. (b) The dislocation lines are likely due to the presence of two rotational domains. Large defects are present at the basal plane of WS₂, as shown in (d)-inset. (c) The same STM image as in (b), but with SL regions masked with red color (excluding the edges). (d) A histogram representing the distribution of the measured apparent height (red points) in the masked region in (c). The distribution is fitted with two Gaussians (colored curves). The black line corresponds to the sum of two peaks. Inset shows the high-resolution STM image of SL WS₂/Ag(111) where the defects are visible. (e) Analogous distribution for the SL WS₂/Au(111) fitted with a Gaussian. STM imaging parameters are: (a) 0.56 nA and 0.81 V, (b) 0.09 nA and 1.43 V, (d-inset) 0.42 nA and 1.16 V.

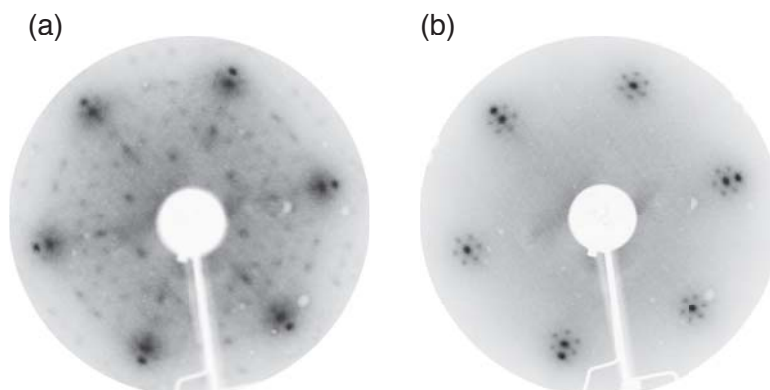


Figure 4.11: Comparison of LEED images taken with kinetic energy of 98 eV for a ca. 0.3 ML sample of WS₂/Ag(111): as grown (a) and after a 30 min anneal in UHV at 700°C(b).

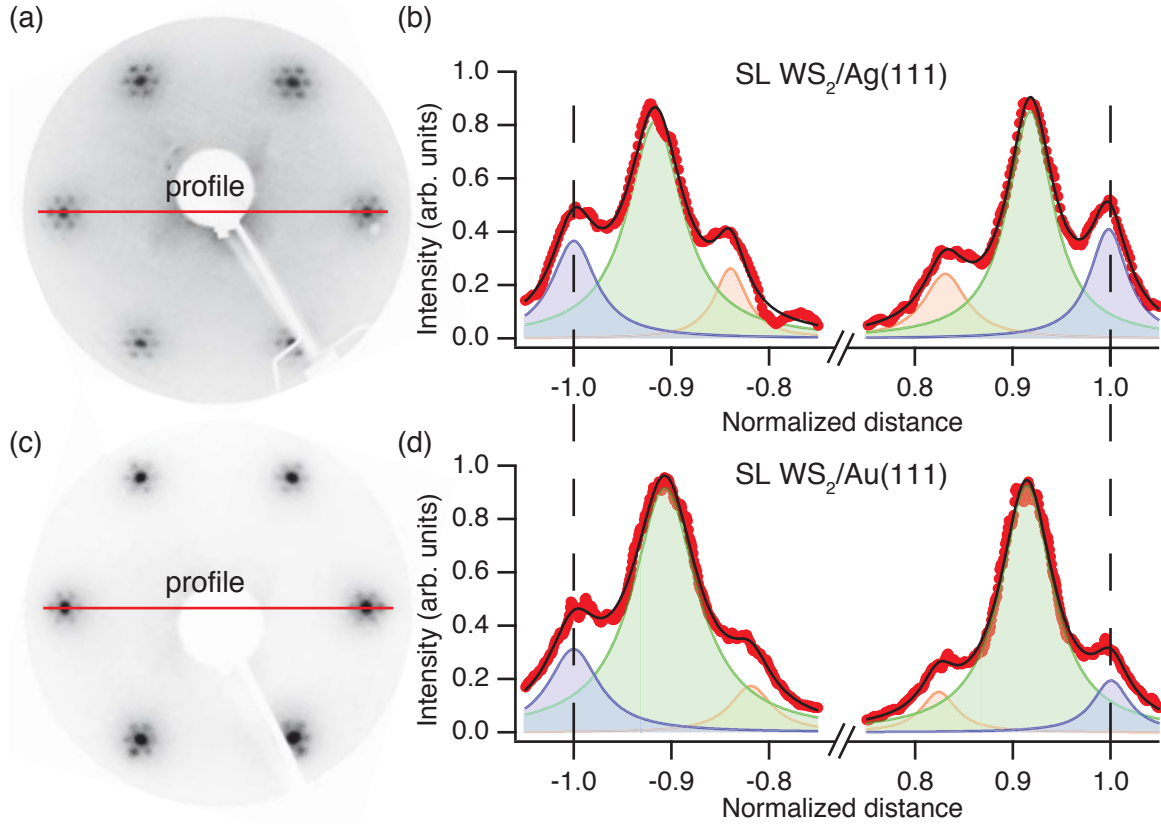


Figure 4.12: Comparison of LEED images taken with kinetic energy of 114 eV for the ca. 0.75 ML samples of $\text{WS}_2/\text{Ag}(111)$ and $\text{WS}_2/\text{Au}(111)$ in (a) and (c), respectively. (b)-(d) Line profiles through the first order spots, as indicated in (a)-(c), respectively. The peaks in the LEED profiles (red points) are fitted with Lorentzian line shapes (colored curves) on a linear background. Black lines correspond to the sum of all peaks. Note that the WS_2 spots and moiré (green and orange curves) are slightly shifted for profiles in (b) and (d), consistently with ca. 0.2% difference in lattice constant of Au and Ag.

conduction band minimum away from \bar{K} , which results in an indirect gap for the free-standing SL WS_2 [155]. For that reason, it is crucial to evaluate the possibility of strain in the grown films. It was previously demonstrated that LEED profile analysis can be applied to establish the lattice constant of a 2D material with uncertainty below 1% [156]. We perform similar analysis here, as illustrated in Fig. 4.12. We extract line profiles through the first order spots of WS_2 , substrate and moiré and fit them with Lorentzians. The distance in reciprocal space is normalized such that outer most peak positions correspond to ± 1 , as seen in Fig. 4.12 (b),(d). In this way, the ratio of reciprocal lattice vectors of WS_2 and the substrate is directly given by the position of the middle peak. Assuming an unreconstructed surface underneath, we use the well-known lattice constants of Au and Ag to calculate the lattice spacing of SL WS_2 . This procedure performed for 3 equivalent cuts in the reciprocal space and 3 images taken at different energies (in total 36 data points) yields the lattice constant of $3.151(0.019)\text{\AA}$ for $\text{WS}_2/\text{Au}(111)$ and $3.152(0.021)\text{\AA}$ for $\text{WS}_2/\text{Ag}(111)$. Those values are in excellent agreement with the bulk WS_2 lattice constant of $3.1532(0.0004)\text{\AA}$ [146]. Based on those result we can exclude a strain larger than 0.7% for SL WS_2 grown on Ag(111) and Au(111).

4.5 TaS₂ on Au(111)

SL TaS₂ was grown on Au(111) using two different methods, and in this section we compare the results. The first approach was the same synthesis method discussed above (evaporator method). The second approach was inspired by Prof. Ludwig Bartel's group (UC Riverside). This method utilizes a hot tantalum filament placed in the vicinity of a sample. H₂S gas is passed through the filament which results in the formation of TaS₂ on the substrate (filament method). The results presented in this section were obtained as a collaboration: the growth and LEED measurements were performed in Aarhus and afterwards the samples were transferred in an UHV suitcase to the group of Prof. Alexander Khajetoorians (Radboud University), where low-temperature STM measurements were performed by Charlotte Sanders and Andreas Eich.

Growth using the evaporator method results in a formation of well-separated triangular TaS₂ islands (see Figs. 4.13(a) and (d)). This is in contrast to the previously studied MoS₂ and WS₂ samples, in which clusters of large size were rather found as polygons. This indicates different growth dynamics for metallic SL TMDCs in comparison to the semiconducting ones. The moiré superstructure with a period of 23.1(0.4) Å is clearly observed and the average apparent height (2.5(0.3) Å) is consistent with the previous results for MoS₂ and WS₂.

Growth using the filament method results in the epilayer exhibiting a completely different morphology. Representative STM image of surfaces morphology is presented in Fig. 4.13(e). We observe a dominating growth of SL TaS₂ with a small contribution of BL TaS₂ and elongated clusters which are presumably Ta_xS_y, since they resemble Mo₆S₆ nanowires described in Section 4.2. SL TaS₂ is found in a form of large (several hundreds of nm) polygonal islands, without a particular preference concerning the shape (Fig. 4.13(b)). Those islands are found to be uniform and without clear domain boundaries. This suggest a single-domain growth, at least within the large island area. The moiré periodicity and amplitude are found to be consistent for the TaS₂ grown with both methods, as seen in Fig. 4.13(f). However, the edges of domains seems to have different apparent heights. Also, the apparent height of the whole domain (ca. 5 Å) seems to be significantly higher than in case of small triangular islands, as presented in Fig. 4.13(c). This apparent height is consistent with results obtained for SL TaS₂ situated on the Au atomic steps, which leads us to the conclusion that SL TaS₂ obtained from the filament method grows over the whole terrace and further growth is stopped at descending edges. Nevertheless, we observed a substantial number of domains across the ascending step, so there might be a preference for the growth through ascending steps over the descending ones.

LEED measurements reveals further differences between samples grown with the filament and evaporator methods, as seen in Fig. 4.14. Overall, the spots are much sharper in case of samples grown with the filament method. The LEED profile analysis yields the value of SL TaS₂ lattice constant of 3.292(0.035) Å, which is in agreement with the value of 3.3(1) measured by STM, and the previously measured bulk lattice constant of 3.31 [157]. Interestingly, higher order moiré spots are observed for the samples grown with the filament method. Also, additional spots can be clearly identified, as indicated in Fig. 4.14(b). Those spots resemble 30° rotated first order TaS₂ spots. We study the possible moiré patterns by constructing simple lattice models after [101], as described in Chapter 3. The model of TaS₂ aligned with the Au substrate is presented in Fig. 4.15. The results of this model are in excellent agreement with STM and LEED measurements. We find a weak intensity in a position corresponding to the LEED additional spot. It is surprising that this spot is very intense in the measurements, while its corresponding Fourier component is marginal. However, LEED intensity is a complex quantity involving multiple-scattering theory [158], so such a simple approach might not be sufficient to

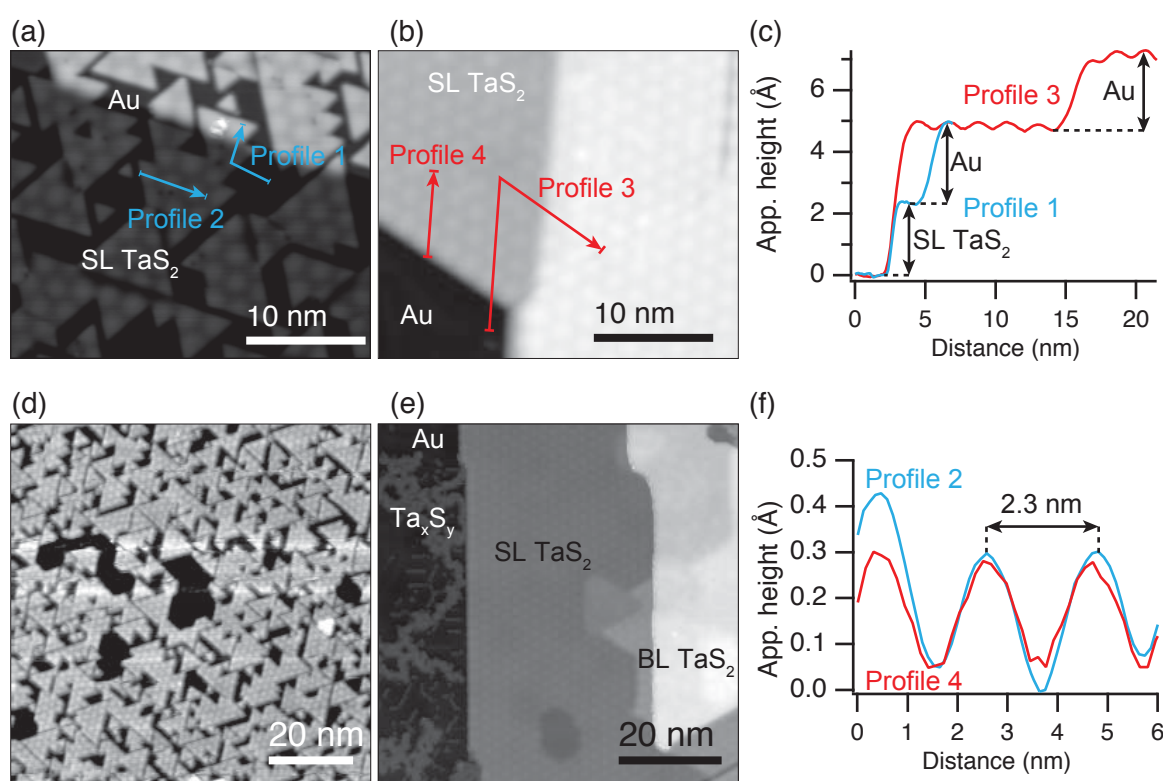


Figure 4.13: STM images of TaS₂ on Au(111) grown with two different methods: evaporator (a) and filament (b) method. See the text for details. (c),(f) STM profiles along the lines indicated in (a) and (b). (d),(e) Large-area STM images corresponding to (a) and (b), respectively. STM imaging parameters are: (a) 0.2 nA and 1 V, (b) 0.1 nA and 0.44 V, (d) 0.1 nA and 0.88 V, (e) 0.05 nA and 0.84 V.

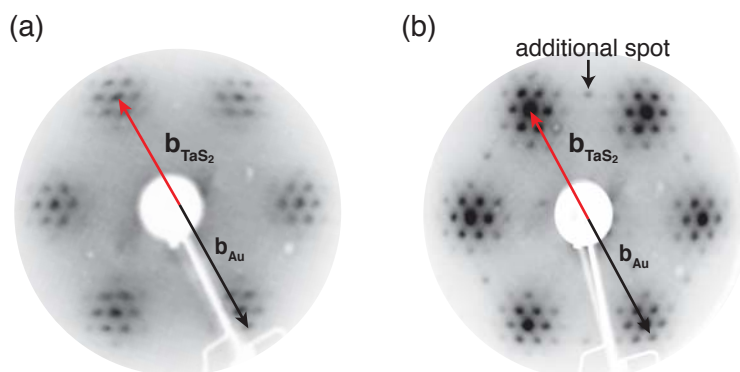


Figure 4.14: (a)-(b) Comparison of LEED images taken with kinetic energy of 90 eV for a ca. 1 ML sample of TaS₂/Au(111) synthesized with the evaporator and filament methods, respectively.

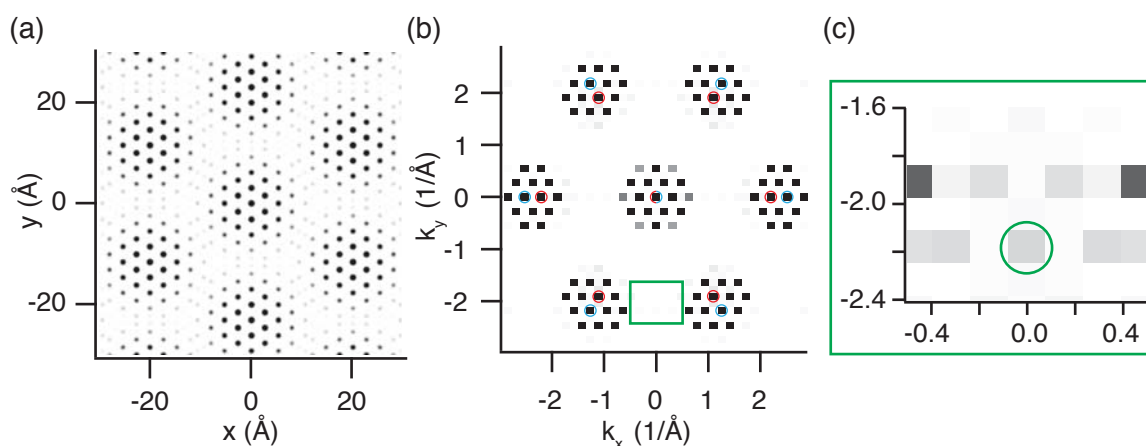


Figure 4.15: (a) Real and (b) reciprocal space images of the modeled SL TaS₂ lattice aligned with Au(111) lattice. (b) Red and blue circles mark the Fourier components of the epilayer and the substrate, respectively. The unmarked components correspond to the moiré replicas. (c) A close-up of the region marked by green rectangle in (b). The green circle mark the position of the moiré replica associated with the additional spot observed with LEED in Fig. 4.14(b). Contrast is enhanced in (c) for clarity.

describe accurately the observed LEED pattern. In order to test the hypothesis of a second domain, we calculate the contrasting model, in which the TaS₂ is rotated by 30° with respect to the substrate. This leads to a different moiré pattern with the periodicity of ca. 5.7 Å, as presented in Fig. 4.16(a). The presence of such a structure was not observed with STM. Also, the simulated reciprocal space pattern differs substantially from the observed LEED images (Fig. 4.16(b)). Based on those findings, we find the growth of 30° rotated domain to be unlikely. Another possible origin of the additional periodicity is the contribution from Ta_xS_y regions. Indeed, we observe a growth of presumed Ta_xS_y nanowires in the perpendicular direction to the Au lattice, which agrees with the previous observation of Mo₆S₆ grown on Cu(111) [142]. Nevertheless, LEED data analysis shows that the additional spots correspond to a periodicity closely matching the one of TaS₂ (within 1% of uncertainty), making any other Ta_xS_y structure an unlikely source of those observations.

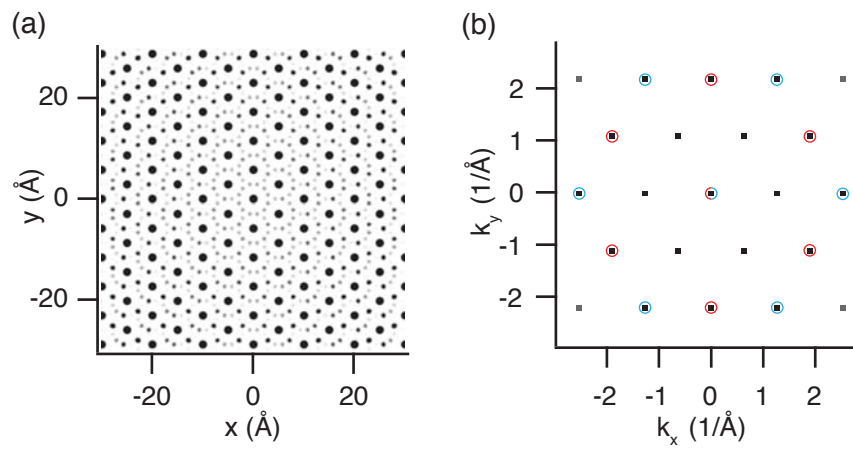


Figure 4.16: (a) Real and (b) reciprocal space images of the modeled SL TaS₂ lattice rotated by 30° in respect to the Au(111) lattice. (b) Red and blue circles mark the Fourier components of the epilayer and the substrate, respectively.

Chapter 5

Electronic structure of single-layered transition metal dichalcogenides

This chapter focuses on the electronic structure of 2D TMDCs. ARPES results together with DFT calculations are presented. The influence of a substrate on the electronic structure is elucidated by the comparison of TMDC synthesized on substrates with the various strength of interaction. The effect of strong SOC in SL WS₂ is discussed. Finally, low-temperature STM/STS data suggesting the suppression of CDW in SL TaS₂/Au(111) is presented and further elaborated in the context of the measured electronic band structure.

5.1 SL MoS₂ on Au(111)

5.1.1 ARPES characterization

Previous ARPES studies of SL MoS₂ has been performed on mechanically exfoliated flakes [159] and CVD-grown samples [160]. Nonetheless, the quality of grown films in those studies was not sufficient for a detailed bandstructure determination, in particular for the most interesting region around the VBM. The methods described in Chapter 4 enabled us to synthesize the samples of much higher quality, which we utilized for studying the dispersion of SL MoS₂ in the whole SBZ.

The samples for ARPES measurements presented in this section were synthesized in a dedicated growth chamber maintained by the group of Prof. Jeppe Lauritsen (Aarhus University). The coverage of SL MoS₂ was chosen to be well below a complete monolayer (ca. 0.65 ML) in order to ensure the lack of BL regions, which could influence the results. After growth, the samples were transported to the SGM3 endstation and mildly annealed up to ca. 200°C. ARPES data were collected at 80 K with an energy and angular resolution better than 20 meV and 0.2°, respectively. All measurements presented in this section were performed with a photon energy of 49 eV.

Figure 5.1 gives an overview of the epitaxial SL MoS₂ band structure. The constant binding energy cuts in Figs. 5.1(a)–(d) reveal both Au(111) and SL MoS₂ features. The Au(111)-related states are best identified near the Fermi energy due to the lack of SL MoS₂ states there. We observe the signature of the familiar noble metal Fermi surface as well as a weak and broad signal stemming from the electronic surface state of Au(111) [161]. At higher binding energies, maxima in the upper VB states of SL MoS₂ are observed, both at the $\bar{\Gamma}$ as well as at the \bar{K} points. These features are also seen in the measured dispersion shown in Fig. 5.1(e). While the states near \bar{K}

are very distinct and sharp, those near $\bar{\Gamma}$ and \bar{M} are rather broad (see Figs. 5.1(e)-(h)). This is ascribed to the different interaction with the substrate and the orbital character of the states. The upper VB near \bar{K} falls into a projected band gap of the Au(111) electronic structure [97] and can therefore not interact with the bulk states. Indeed, the presence of this gap is even visible in the data of Fig. 5.1(e) as a reduction of background intensity between the Fermi energy and a binding energy of ca. 2.2 eV around \bar{K} . It is marked by a dashed line in Fig. 5.1(f). Moreover, the upper VB near \bar{K} is derived from in-plane d - and p -orbitals [27, 162] and thus a weak adsorbate-substrate interaction is expected. The upper VB states near $\bar{\Gamma}$, on the other hand, fall within the continuum of projected bulk states [97] and are derived from out-of-plane orbitals [27, 162]. For these states a relatively stronger adsorbate-substrate interaction can be expected and this can explain the broadening of the band. Such an increased interaction is also supported by a comparison of the measured dispersion and the density functional theory band structure for freestanding SL MoS₂ by Zhu et al. [27]. In Fig. 5.1(f), this calculation is superimposed on the data and aligned at the VBM at \bar{K} . In the calculation, the upper VB maxima at \bar{K} and $\bar{\Gamma}$ are found at nearly the same binding energy. This is also the case for calculations that include many-body effects [59] and in ARPES results from exfoliated SL MoS₂ [159]. Our data, in contrast, show a distortion of the upper VB with the measured maximum at $\bar{\Gamma}$ being 0.31 eV lower than at \bar{K} . It is worth noting that the dispersion for exfoliated SL MoS₂ on SiO₂ also deviates from calculation but in a different way: While the VB maxima at \bar{K} and $\bar{\Gamma}$ are aligned, the total width of this band is significantly smaller than in the calculation. Here, on the other hand, the bandwidth agrees very well with the calculation (see Fig. 5.1(f)). The observed distortion of the upper valence band near $\bar{\Gamma}$ has only a small effect on the effective mass. A fit to a holelike parabola (see Figs. 5.1(g)-(h)) gives an effective hole mass of 2.7(0.1) times the free electron mass m_0 , in agreement with the calculation for SL MoS₂ (2.8 m_0) [163] and the result for exfoliated SL MoS₂ (2.4(0.3) m_0) [159], but much higher than the bulk value (0.62 m_0) [163].

Another expected consequence of the SL MoS₂- substrate interaction would be a manifestation of the pronounced moiré in the electronic structure. A similar moiré has pronounced consequences for the electronic structure of epitaxial graphene, leading to the presence of replica bands and minigaps in the Dirac cone [164, 165]. Here, such replicas would be expected at a distance of ca. 0.17 Å from the main features. We should easily be able to resolve such features, especially for the sharp bands near \bar{K} , but we find them absent from the data, suggesting that the electronic structure of SL MoS₂ is hardly affected by the moiré. We ascribe the difference to graphene to the different character of the states near \bar{K} : In graphene, the buckling of the layer directly affects the local interaction of the out-of-plane π orbitals with the substrate. In MoS₂, on the other hand, the bands have a mix of Mo $d_{x^2-y^2}$, d_{xy} , and S p_x , p_y character and are thus totally in-plane. Their local interaction with the substrate can be expected to be less affected by the buckling. Note that this argument does not hold for the upper VB near $\bar{\Gamma}$ where the states have out-of-plane character. While replicas of this band due to the moiré are not observed, we cannot exclude that they contribute to the large width of this band.

Apart from $\bar{\Gamma}$, the dispersion of the bands around \bar{M} is the second point of disagreement between the measured dispersion and the calculation for the free-standing layer. In the calculation, the spin-splitting of the bands reduces to zero at \bar{M} . This is expected at \bar{M} (and at $\bar{\Gamma}$) due to the combination of time-reversal and crystal symmetry. \bar{M} is a so-called time-reversal invariant momentum in the 2D BZ [166], meaning that two \bar{M} points can be connected both by an inversion of the \mathbf{k} -direction and by a reciprocal lattice vector. The combination of these symmetries enforces a spin-degeneracy in the 2D electronic states. This degeneracy is observed at $\bar{\Gamma}$ but the situation is somewhat unclear at \bar{M} . We shall return to these two points of disagreement when we discuss the calculations for SL MoS₂ adsorbed on Au(111).

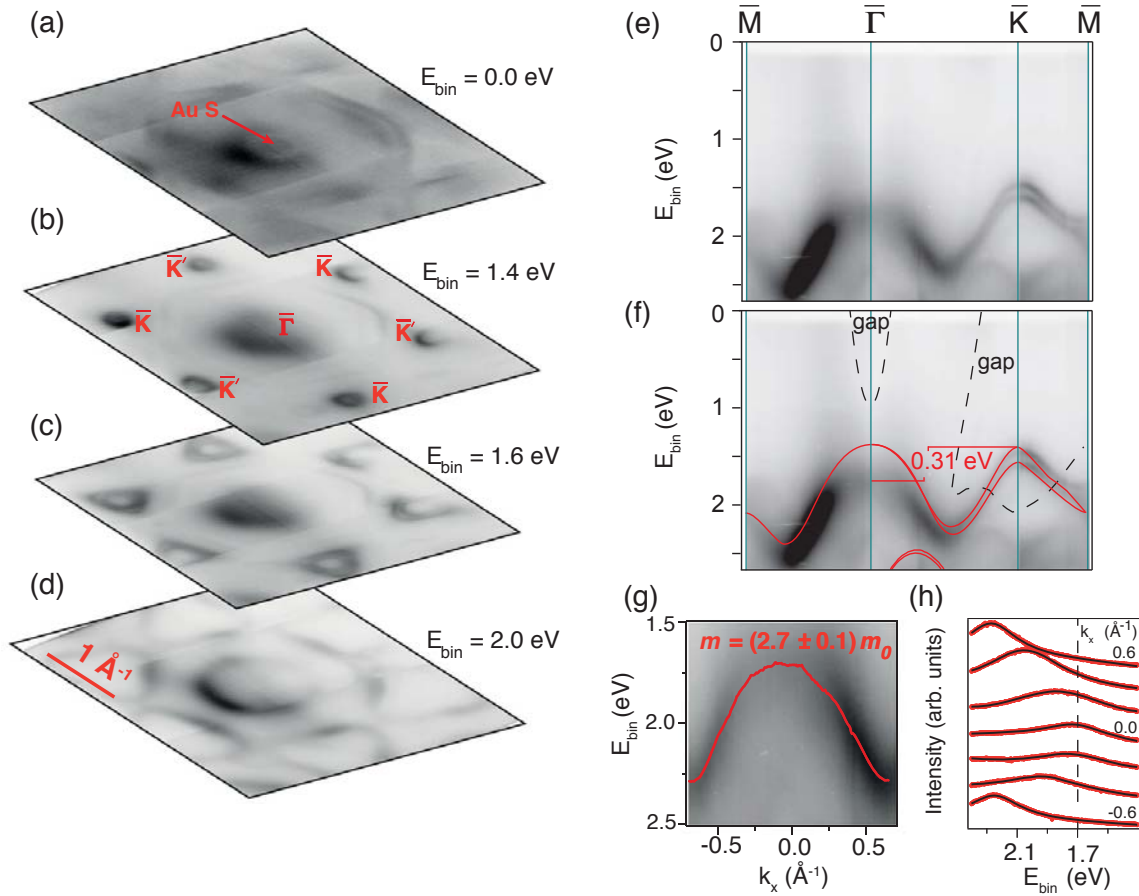


Figure 5.1: Electronic structure of epitaxial SL MoS₂: (a)–(d) Constant energy slices through the first Brillouin zone, showing (a) the Fermi contour dominated by Au bulk states and the surface state (Au S) and (b)–(d) evolution of MoS₂ valence band features around \bar{K} , \bar{K}' , and $\bar{\Gamma}$ points. (e) Valence band dispersion along the high-symmetry directions. (f) The same data as in (e) but with the theoretical dispersion for a free-standing layer (solid red lines) [27] and projected band gap edges of the (111) surface of Au (dashed lines) [97] superimposed. (g) Close-up of the MoS₂ upper valence band dispersion around $\bar{\Gamma}$. The red line is the peak position extracted from energy distribution curves shown in (h). The curvature of the parabolic band provides the stated effective mass m in units of the free electron mass m_0 . The two-dimensional high-symmetry points in this figure refer to the SL MoS₂ structure.

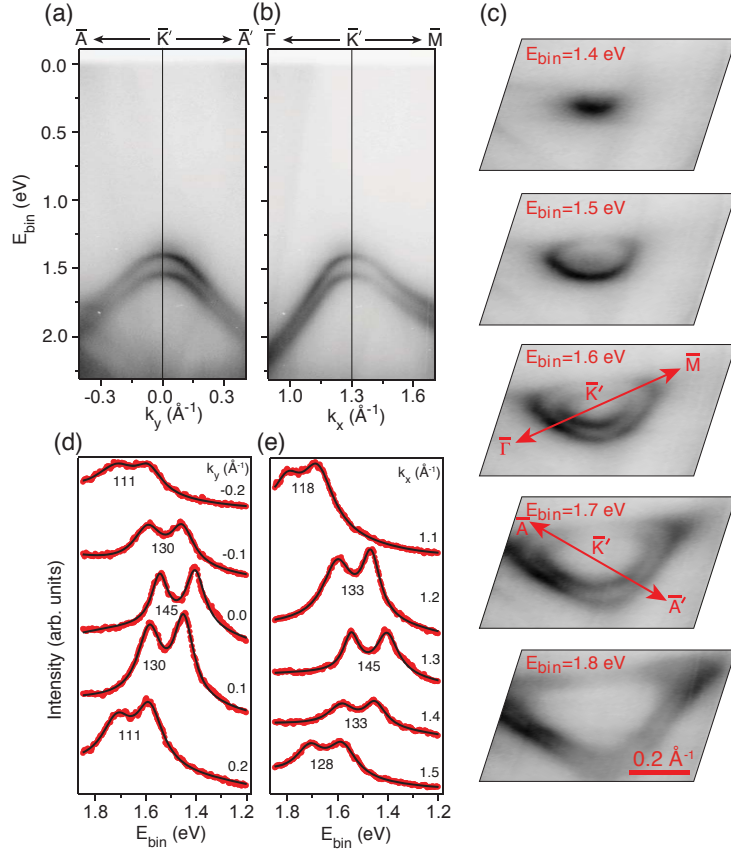


Figure 5.2: Detailed dispersion around valence band maximum at \bar{K} (\bar{K}') and analysis of spin-orbit interaction. (a)–(b) Cuts along directions defined in the constant energy contours in (c). The points \bar{A} and \bar{A}' are along the line perpendicular to the $\bar{\Gamma}$ - \bar{K} direction passing through \bar{K} . (d)–(e) EDCs at the given momentum values. The peaks are fitted by a double Lorentzian function, and the difference between peak positions is taken as the splitting of the bands, which is stated in meV below the curves.

A remarkable effect is the strong spin-orbit splitting of the upper VB near \bar{K} , shown in greater detail in Fig. 5.2. Note that the splitting in SL MoS₂ is a genuine lifting of the spin-degeneracy and different from the splitting in the inversion-symmetric bulk material, where it is a combination of layer interaction and spin-orbit coupling and does not remove the spin degeneracy [59]. An equivalent splitting has been observed in ARPES from SL MoSe₂ grown on epitaxial graphene [143] but it has so far remained unresolved for exfoliated SL MoS₂ [159]. The size of the splitting can be determined from a fit of the EDCs obtained from the data in Figs. 5.2(a),(b) and shown in Figs. 5.2(d),(e). The strongest splitting at \bar{K} is found to be 145(4) meV. This is somewhat bigger than the value of ca. 100 meV obtained by triply resonant Raman scattering[167] and, as expected, smaller than the ARPES result for SL MoSe₂ of 180 meV. It is in excellent agreement with the theoretical prediction of 148 meV from density functional theory [27] and 146 meV from GW calculations [59]. The anisotropy of the splitting away from \bar{K} that gives rise to a triangular warping of the constant energy contours in Fig. 5.2(c) also agrees with the theoretical prediction [27]. SL MoS₂ is expected to be a semiconductor with a direct band gap at \bar{K} , in contrast to the bulk that has an indirect band gap [26, 28, 124].

Access to the CBM of the SL MoS₂ in ARPES is possible by doping with potassium. This is illustrated in Fig. 5.3, which shows a series of scans along the \bar{M} - \bar{K} - $\bar{\Gamma}$ and \bar{A} - \bar{K} - \bar{A}' directions of the SBZ for the clean surface and increasing exposures to potassium. Overall, the expected

strong electron doping is indeed observed: For a small potassium dose, all bands are shifted to higher binding energies and a weak photoemission intensity due to the conduction band minimum at \bar{K} becomes observable (Figs. 5.3(b),(e)). As the doping is increased, the CBM becomes populated, demonstrating the direct band gap of the material, as the VBM is also at \bar{K} (Figs. 5.3(c),(f)). The CBM is found to be rather broad, in contrast to the VBM at \bar{K} , consistent with the out-of-plane character of these states [27, 162]. We determine the gap energy to be 1.39(0.05) eV, substantially smaller than the value of 2.8 eV predicted from *GW* calculations which account for electronic correlations [168]. We attribute the observed band gap reduction to both intrinsic (metallic substrate) and extrinsic (doping) reasons. Typically, the band gap is not strongly dependent on the doping, but for low-dimensional materials strongly-enhanced electron correlations can lead to giant band gap renormalizations [169]. Additional electrons can induce lattice dilation and screen the electron-electron interaction, reducing the band gap substantially in a highly non-linear manner [170]. This issue can be partially overcome by using time-resolved ARPES technique, which utilize the optical pumping of electrons into the conduction band and subsequent emission by a second photon, or by STS technique. The studies using those methods indeed report the band gap of SL MoS₂/Au(111) to be significantly larger: 1.95(0.05) eV in case of time-resolved ARPES [171], and 1.74(0.27) eV for STS [172], but still smaller than the theoretical value. We expect that effect of the metallic support leads to further band gap reduction in terms of intrinsic doping and enhanced screening. This effect has been studied theoretically by placing SL MoS₂ onto (insulating) BN and (conductive) graphene and this change leads to a band gap reduction of ca. 0.5 eV. Experimentally, the effect has been probed with STS for SL MoSe₂ that was grown on both bilayer graphene and bulk graphite [144]. In this case, the effect is not as drastic because both substrates are conductive, but it still leads to a band-gap reduction of ca. 0.24 eV for the more conductive bulk graphite. It should be noted that comparison of the electronic band gap obtained using ARPES or STS to the optical band gap obtained using photoluminescence experiments [28] might be misleading. In simple terms, the optical band gap corresponds to the energy required to create an exciton while the electronic band gap also requires the breaking of the exciton and is thus higher due to the exciton binding energy. In case of bulk MoS₂, the difference is not significant as the exciton binding energy is ca. 50 meV [173], but for a SL this can be as large as 570 meV [174] due to increased electron correlations in 2D.

Upon closer inspection of Figs. 5.3, it becomes clear that potassium adsorption does not give rise to a simple rigid shift of the valence band to higher binding energies: While the VBM at \bar{K} shifts by 1.39 eV - 1.56 eV = -0.17 eV from the clean sample to the highly potassium-dosed situation, the maximum at $\bar{\Gamma}$ shifts by 1.70 eV - 2.03 eV = -0.33 eV, such that the upper VB is severely distorted upon doping. These shifts, together with the observed distortion of the upper VB in the undoped case and the reduced band gap, can all be accounted for by the orbital character of the states involved: Both the upper VB at $\bar{\Gamma}$ as well as the CB minimum at \bar{K} are predominantly of out-of plane $d_{3z^2-r^2}$ character [27, 162] and these states are found to shift to higher binding energy upon either interaction with the substrate or exposure to adsorbed alkali atoms. It is this shift that already deforms the upper valence band near $\bar{\Gamma}$ for the pristine SL MoS₂ on Au(111) and this deformation is merely enhanced upon potassium adsorption. A significantly distorted upper valence band was also found for transferred SL MoS₂ on oxidized Si [159]. In that case, the distortion is quite different in that it leads to a narrowing of the entire band with the energies at $\bar{\Gamma}$ and \bar{K} almost at the same energy. This distortion was also ascribed to the MoS₂-substrate interaction.

The strong dependence of the band maximum at $\bar{\Gamma}$ on the substrate can be understood in the following simple picture: the transition from an indirect to a direct band gap in MoS₂ upon the

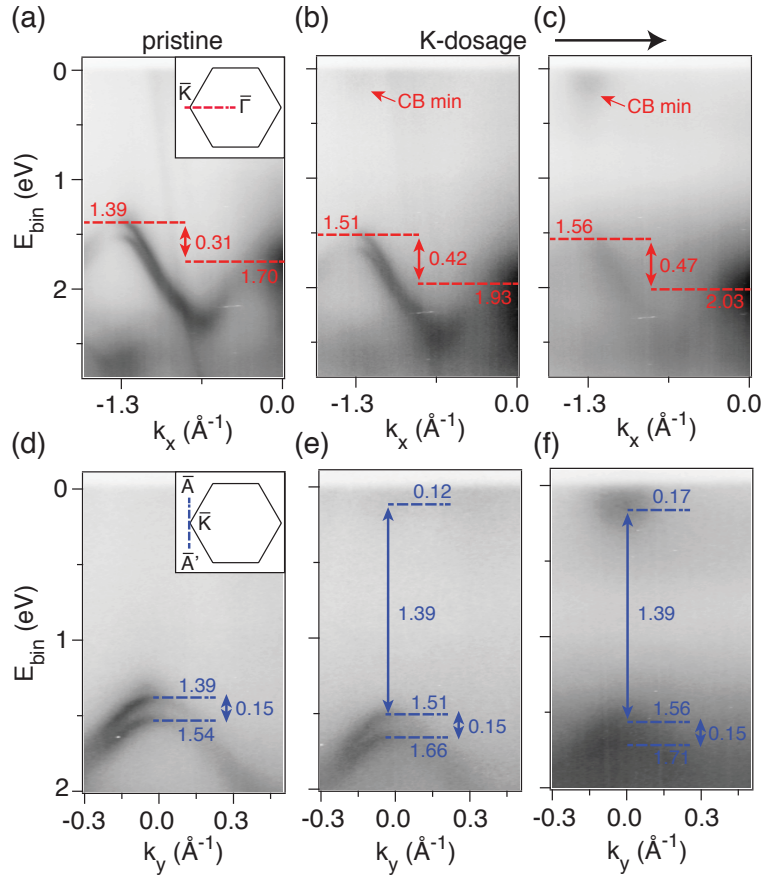


Figure 5.3: Tuning of the band structure by potassium adsorption. (a),(d) Clean sample, (b),(e) first dose, and (c), (f) second dose. The scan directions for the cuts in (a)–(c) and (d)–(f) are given in the insets of (a) and (d), respectively. The points \bar{A} and \bar{A}' are defined in the caption of Fig. 5.2. The energies are given in eV.

reduction to a SL has been ascribed to a quantum confinement effect [26, 28]. An inspection of the band structure for a different number of layers shows that the confinement-induced energy changes are strongest for the upper valence band maximum at $\bar{\Gamma}$ [26]. In fact, the confinement has a much stronger effect on these states than on the conduction band minimum near \bar{K} , despite the similar orbital character. The energy of such quantum-confined states does not only depend on the thickness of the film but also on the wave function's phase shift at the boundaries, i.e., at the MoS₂-substrate and MoS₂-vacuum interfaces [175]. This explains the sensitivity of the VBM at $\bar{\Gamma}$ on the character of the substrate and also on the modification of the vacuum interface upon doping.

5.1.2 DFT calculations

The obtained results underline the influence of substrate interactions on the electronic structure of 2D materials. In order to further validate generic arguments based on the origin of orbitals forming the band structure we study the results of the DFT calculations, which model SL MoS₂ adsorbed on Au(111). Those calculations were performed by the group of Prof. Bjørk Hammer (Aarhus University).

Electronic structure calculations were carried out using the VASP code [176–178]. The valence

electrons were described with plane-wave basis sets with a kinetic energy threshold of 415 eV, and the interaction between the valence and frozen core-electrons was accounted for by means of the projector-augmented-wave (PAW) method of Blöchl [179]. The PBE approximation to the exchange-correlation functional was used [180]. Further details of the following calculations can be found in Ref. [172].

The lattice mismatch between the Au substrate and the MoS₂ epilayer pose a severe problem for the calculations. The realistic (10×10) MoS₂ superstructure on a (9×9) supercell of Au(111) is computationally unfeasible, so the problem needs to be somehow simplified. We propose two models presented in Fig. 5.4: (1×1) structure with Au lattice expanded by 9% to match MoS₂ (matched model), and ($\sqrt{13} \times \sqrt{13}$)R13.9° MoS₂ supported on (4×4) Au lattice (mismatched model) suggested originally by Farmanbar *et al.* [152]. Although significant expansion of Au lattice results in artificial destabilization of the Au surface and to shifts of Au surface and bulk bands to higher energies, it is a useful tool to directly study the MoS₂-Au interaction and its effect on the band structure of the SL MoS₂. On the other hand, mismatched model only requires a 0.15% contraction of the Au lattice in order to avoid the artificial distortion of the work function of the Au surface. In this model, a slightly smaller unit cell, than the experimentally observed supercell shares most of the structural features observed in experiments, including the different S-Au contact regions, i.e., on-top, hcp, and fcc, within the unit cell.

In case of matched model, the bottom S atoms can be placed in the fcc, hcp or on-top site (Fig. 5.4(a)). A structural optimization of the matched models results in the on-top position model being the most stable one by 199 and 215 meV per unit cell, compared to the hcp and fcc models, respectively. This higher stability is accompanied by a smaller optimized distance r between the lower S layer and the outermost Au layer (Fig. 5.4(c)) for the on-top structure (2.51 Å), as for the fcc and hcp structures (3.20 and 3.03 Å, respectively). Interestingly, such height differences are in close to quantitative agreement with those measured in experimental STM images of SL MoS₂ on Au(111) [181]. However, the intuitive assignment made in Ref. [181] of the different areas within the moiré pattern, where topographically higher regions are assigned to on-top bonding modes, may be called into question in view of the present results, where the on-top configuration leads to the smallest r of the matched models. For the mismatched model, the optimized r is 3.29 Å, which is larger than for the matched models, probably as a result of S atoms being, on average, in less favorable positions.

The calculated band structure for the free-standing MoS₂ layer (Fig. 5.5, first panel) is in excellent agreement with previous results using the same exchange-correlation functional [27], and the resulting band gap (1.58 eV) is also very similar. This value significantly underestimates the electronic gap of 2.8 eV determined by more sophisticated quasiparticle *GW* calculations [168]. Nevertheless, studying the MoS₂/Au(111) with standard DFT methods provides valuable insight into the effect of the substrate on the band structure despite the gap underestimation.

Figure 5.5 presents the results of the calculations performed for the matched model (on-top). Adsorption of the MoS₂ layer on Au(111) leads to pronounced changes in its band structure (Fig. 5.5, second panel) but, surprisingly, the fundamental gap near \bar{K} (1.58 eV) is only 0.02 eV lower than for the free-standing layer. Moreover, the bands forming the VBM and CBM of the layer remain well-defined, something that is ascribed to their greater contribution from Mo orbitals (which do not directly bond to the Au substrate), to the in-plane nature of such states for the VBM and, most importantly, to their position in a projected gap of the Au(111) band structure. The binding energies of the occupied bands for the matched model are generally in good agreement with the experimental values from ARPES, and the position in the projected band gap is consistent with the VBM states being very sharp in ARPES. However, the exact

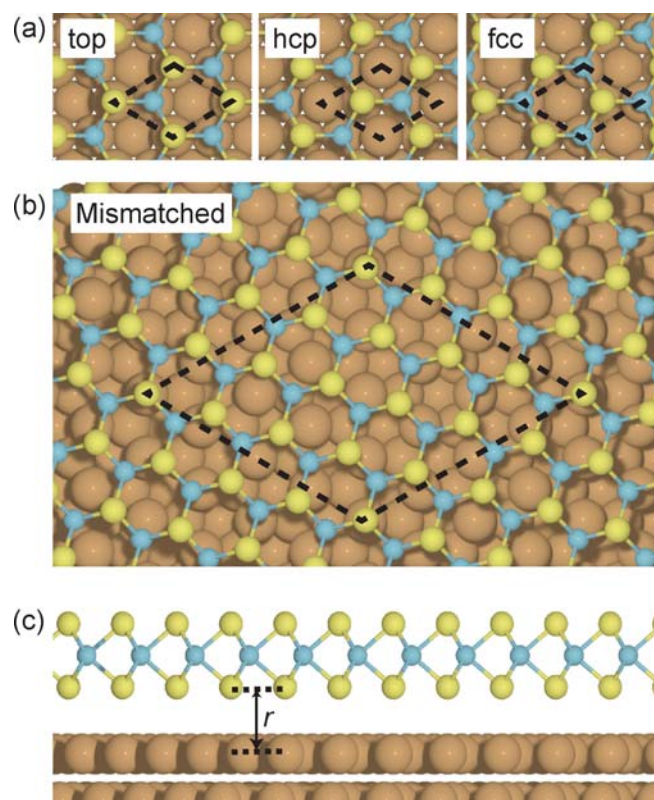


Figure 5.4: Models used for the DFT calculations. (a) Top views of the matched model consisting of a (1×1) unit cell of MoS₂ on a (1×1) cell of Au(111). The different positions considered of the bottom S atoms with respect to the underlying Au lattice (on-top, hcp, and fcc) are shown. (b) Top view of the mismatched model consisting of a $(\sqrt{13} \times \sqrt{13})R13.9^\circ$ cell of MoS₂ on a (4×4) cell of Au(111). (c) Side view of the MoS₂/Au(111) interface indicating the relevant distance r between the lower S layer and the outermost surface layer of Au(111). Turquoise, yellow, and brown spheres indicate the position of Mo, S, and Au atoms, respectively.

energy of the bands for the matched model is affected by the artificial strain induced in the Au(111) slab, as described above, and should thus not be directly compared to the ARPES values. The unchanged size of the band gap with respect to the free-standing SL MoS₂, on the other hand, is a common feature of all models, and the same was found for other mismatched models with compressed Au(111) surfaces when studied with similar levels of theory [153, 182].

In contrast to the situation around the fundamental gap, the upper valence band near $\bar{\Gamma}$ is strongly affected by the adsorption on Au(111). The band is still well-defined as it enters the bulk continuum and its spin-splitting is lost. However, very close to $\bar{\Gamma}$ it strongly merges with the bulk bands. The band maximum at $\bar{\Gamma}$ is very diffuse but significantly lower (by ca. 0.4 eV) than at the \bar{K} point. These observations are in excellent agreement with the experiment where a similar energy shift and a strong broadening, indicative of MoS₂-substrate interaction, is observed. In fact, this band structure change is consistent with the simple expectation that the adsorbate-substrate interaction should mainly affect the boundary condition for the quantization of the out-of-plane states in the SL. Note that the MoS₂ character is retained for higher energy states near $\bar{\Gamma}$.

The band structure can be further explored by decomposing the states of the SL MoS₂/Au(111) model into the contribution from the Mo atoms and from the lower (in contact with Au) and upper (in contact with the vacuum) layer of S atoms. Figure 5.5 shows such weighted band structures, separated into out-of-plane orbitals and in-plane orbitals. The VBM of the MoS₂ layer is mostly formed from in-plane Mo $4d$ states at the \bar{K} point [27, 162] which, together with their position in the projected band gap, explains why it remains relatively unaffected by the interaction with the Au(111) surface. The CBM at the \bar{K} point, on the other hand, is formed by out-of-plane Mo $4d$ states, which are expected to be distorted by out-of-plane interactions. Nevertheless, the size of the fundamental gap at \bar{K} calculated here is unaffected by the interaction with the metallic substrate. This is attributed to the calculation approach which only partially accounts for electronic correlations and neglects long-range exchange. In contrast, more advanced *GW* calculations account for long-range Coulomb interaction and are able to predict subtle screening effects. Indeed, for SL MoSe₂ (which has a very similar electronic structure to MoS₂) a small direct gap reduction is calculated upon interaction with a support [144], and lower \bar{K} - \bar{K} gaps are predicted when increasing the number of layers or decreasing the interlayer distance in MoS₂ [126]. Similar screening effects are expected to be generally present for 2D materials on a substrate. For example, a reduction of the electron-phonon coupling of graphene on Ir(111) was attributed to the screening of the electronic correlations by the metallic substrate [183].

In contrast to the situation at \bar{K} , the VBM at $\bar{\Gamma}$ contains significant contributions from the sulfur $3p_z$ states (as well as some contribution for out-of-plane Mo $4d_{z^2}$ and $4d_{yz}$ orbitals) and here we observe a strong asymmetry for the top and bottom sulfur atoms. While the top-atoms still participate in the formation of the upper valence-band states at $\bar{\Gamma}$, the contribution of the $3p_z$ orbitals of the bottom sulfur atoms is completely hybridized and merged with the Au(111) states. As one might have expected, this is an indication of a Au-S bond formation in the system. Here, we note again that the artificial expansion of the Au(111) unit cell leads to a significant shift of Au surface state to higher energies. Instead of crossing the Fermi level, the Au surface state is found 3–4 eV above it. Furthermore, for this matched model, every lower layer S atom is in an ideal on-top position and Au sp states and S p_z states overlap very efficiently, strongly hybridizing and forming S-Au chemical bonds. As a result, and despite of the energy difference, hybridization of the p_z orbital of the lower S atom with Au can be clearly seen in the last panel of Fig. 5.5, where the greatest contributions from S $3p_z$ orbitals appear at Au bands with strong sp character, i.e., the surface states of Au and other bands with strong contributions from Au s

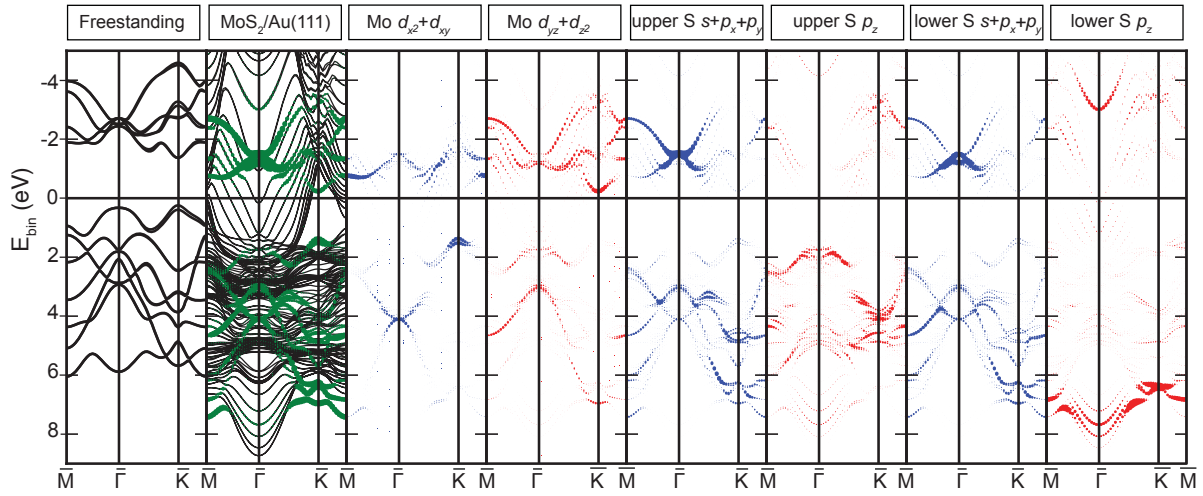


Figure 5.5: Calculated band structures for free-standing SL MoS₂ and SL MoS₂ on Au(111) (matched model). The size of the green circles in the second panel indicate the weight for each state from MoS₂ orbitals. For the rest of panels, the blue (red) circles indicate the weight from in-plane (out-of-plane) orbitals for the Mo atom and for the sulfur atoms on the MoS₂-vacuum (upper S) and MoS₂-Au(111) interfaces (lower S). The weight for the S orbitals have been multiplied by two in order to visualize their contributions more clearly.

orbitals found at very low energies (8 eV).

The interaction with the bulk state continuum can explain the failure to observe the expected spin-degenerate upper valence band at \bar{M} . As can be seen in Fig. 5.5(second panel), the upper valence band mixes so strongly with the Au states that it does not exist as a well-defined state at \bar{M} .

In case of mismatched model, the band structure of a large supercell needs to be unfolded into its smaller BZ in order to recover the primitive cell picture of the band structure of Au-supported MoS₂. This is done by calculating the so-called effective band structure (EBS) for this system. To help differentiate between MoS₂ and Au bands, Fig. 5.6(a) shows the band structure for the Au(111) slab (without the MoS₂ layer) unfolded on the primitive cell of MoS₂. The intensity in the EBS plots for an energy interval dE and a k -vector of the primitive cell depends on the number of states of the supercell that have the same character as the primitive cell k -vector in that energy interval, i.e. that are related by the unfolding operator [184, 185].

Unfolding the band structure of the Au(111) supercell on the primitive cell of MoS₂ results in an EBS with several bands, which shows that despite the mismatch, there are states of the Au(111) slab that have a similar character as the primitive cell of MoS₂. In particular, the d -band continuum of Au appears diffuse below ca. 2.0 eV and several bands cross the Fermi level, some of which have minima at $\bar{\Gamma}$. Two of these bands- probably the ones with the minimum closest to the Fermi level- correspond to the surface states of Au(111). For finite slab models such as the ones used here, there are two surface states (one for each side of the slab). Furthermore, since these two states have the same character and symmetry and unless the slab is sufficiently thick (>20 atomic layers), these interact and give rise to two nondegenerate states [186]. This effect is larger for thinner slabs such as the four Au layer one used in the matched model, and this is reflected in the band structure shown in Fig. 5.6(a), where two Au bands separated by ca. 1 eV and with minima at $\bar{\Gamma}$ are present. The energy of the surface state of Au(111) is thus not well-reproduced due to such nondegeneracy and, although using a much thicker Au(111) slab model

would correctly reproduce the surface state, such calculations would be too computationally demanding. In addition, it should be noted again that the unfolding is done on the unit cell of MoS₂ and this means that the unfolded band structure does not exactly correspond to that of the Au(111) primitive cell.

The EBS for the MoS₂/Au(111) mismatched model in Fig. 5.6(b) shares most of the VBM features of the band structure of the on-top matched model. The characteristic spin-split (by 151 meV) bands at \bar{K} are clearly visible, and the band gap at \bar{K} from the EBS is 1.61 eV, which is very similar to those calculated for the free-standing SL (1.60 eV) or for the on-top matched MoS₂/Au(111) model (1.58 eV). MoS₂ bands merge with the Au *d*-band, and become more diffuse closer to $\bar{\Gamma}$, where they are nearly extinguished. In addition, the same states found crossing the Fermi level in the EBS of the bare Au(111) can also be recognized in the presence of the MoS₂ layer, but shifted towards higher energies. This is not surprising given the n-doping of the MoS₂ layer, which leads to a concomitant p-doping of Au. Interestingly, in contrast to the matched on-top model, MoS₂ bands hybridize with states forming the Au *d*-band continuum rather than with Au surface states, which is due to the smaller overlap between Au *sp* and S *p_z* orbitals. Furthermore, the interaction of MoS₂ band with one of the Au bands not only shifts the latter towards higher energies but also leads to avoided crossings between these bands near $\bar{\Gamma}$ as sketched in Fig. 5.6(c). The mixing of MoS₂ with Au states also destroys the local maximum of valence band at $\bar{\Gamma}$ and instead two local maxima in the vicinity of $\bar{\Gamma}$ are found. This is consistent with the ARPES spectra, where the VBM is hardly discernible at $\bar{\Gamma}$. It is therefore clear that the choice of model affects the role of the Au surface states upon hybridization with MoS₂ states, although it does not affect the fundamental band gap at \bar{K} or the distorted shape of the MoS₂ valence band at $\bar{\Gamma}$.

5.2 MoS₂-graphene heterostructure

The results of the previous section clearly show that the Au substrate influences the electronic structure of SL MoS₂ to a large extent, in particular around $\bar{\Gamma}$. It is, therefore, beneficial to study the dispersion of MoS₂ adsorbed on a more inert substrate. Graphene grown on SiC is a suitable substrate for that purpose due to a weak van der Waals interaction with MoS₂. Further, it is a substrate readily compatible with ARPES technique as it does not charge. Nevertheless, a weak interaction is problematic for the growth of a single rotational domain. In fact, we find a dominant orientation MoS₂ lattice being rotated by 30° in respect to graphene, but with a significant contribution of other orientations. This is affecting the measured dispersion at \bar{K} , making the spin-splitting unresolved, but not so much the isotropic dispersion around $\bar{\Gamma}$. Furthermore, σ -band of graphene is found for binding energy higher than 3.5 eV [187], which ensures no band overlap with the MoS₂ VB edge at $\bar{\Gamma}$. This system is also suitable for studying the electronic properties for multiple-layer MoS₂, as the inter-layer coupling is predicted to change the valence band at $\bar{\Gamma}$ significantly, while having a minimal effect on the dispersion around \bar{K} [59, 188]. Data presented in this section provides complementary information to the results obtained in Sect. 5.1.

The samples of MoS₂ on graphene/SiC were synthesized in a dedicated growth chamber maintained by the group of Prof. Jeppe Lauritsen (Aarhus University). After growth, the samples were transported to the SGM3 endstation and mildly annealed up to ca. 200°C. ARPES data were collected at 70 K with an energy and angular resolution better than 25 meV and 0.2°, respectively. The photon energy range employed for studies of the dispersion and intensity variation of the electronic states at $\bar{\Gamma}$ was 18 to 70 eV.

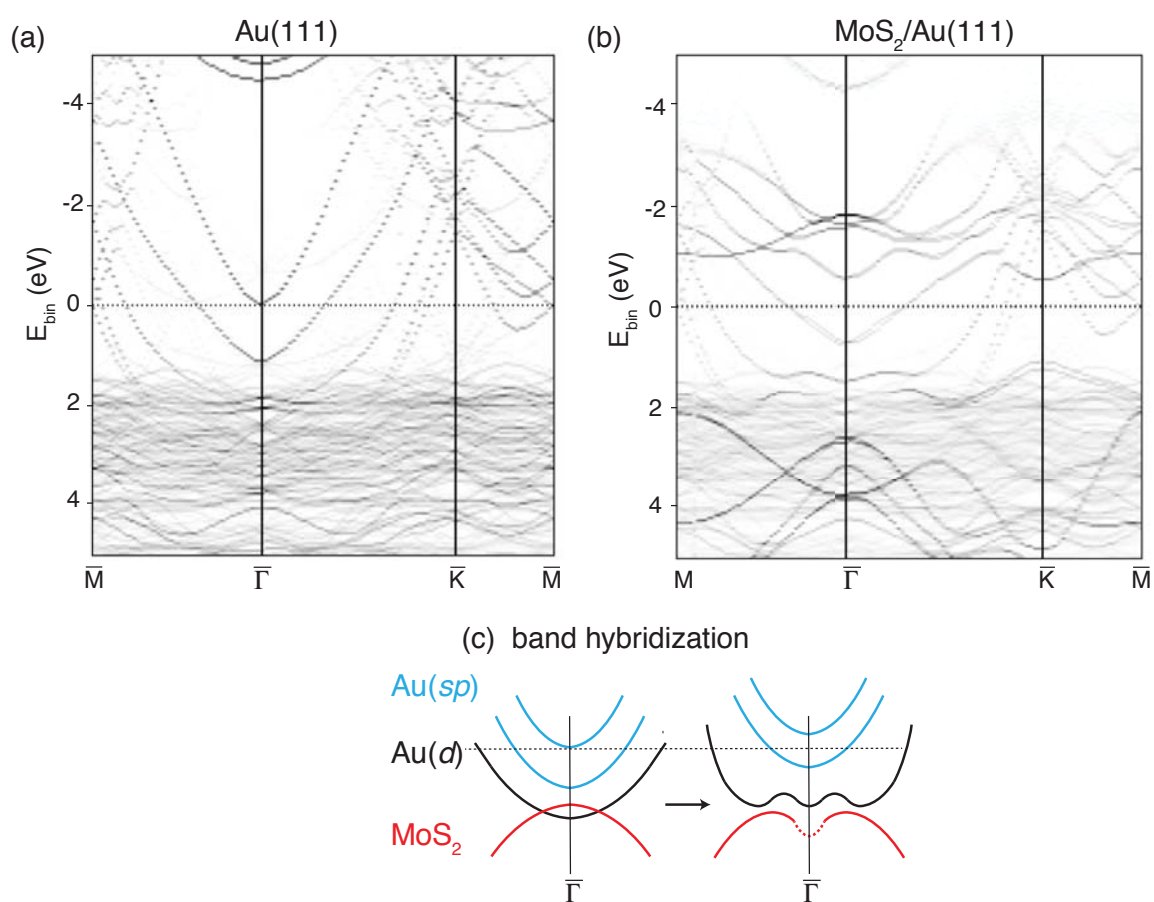


Figure 5.6: Unfolded band structures for (a) a bare (4×4) Au(111) surface and (b) the mismatched model of $\text{MoS}_2/\text{Au}(111)$, as described in the text. The hybridization of MoS_2 states with d -band continuum states of Au is illustrated in (c) for clarity.

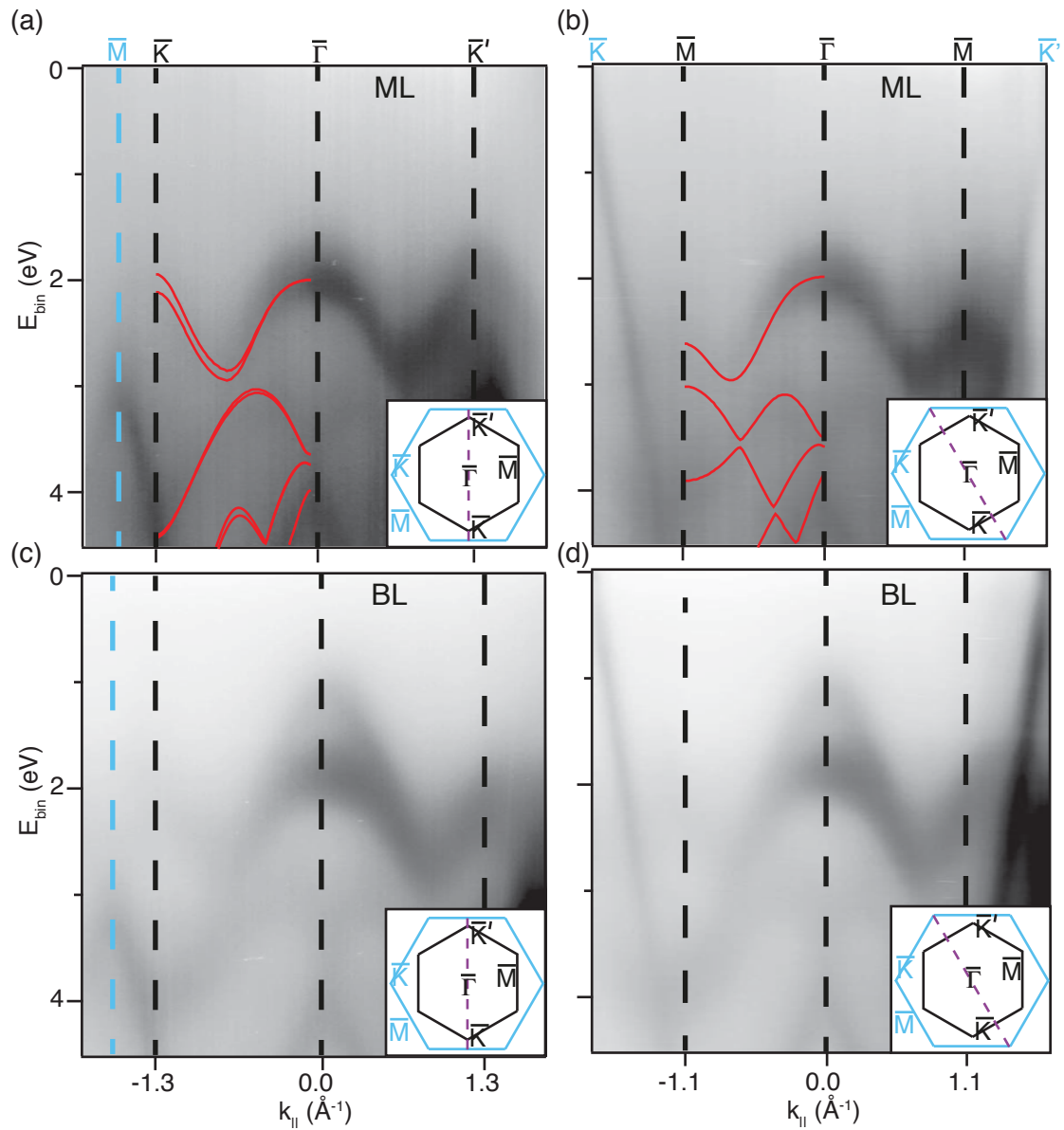


Figure 5.7: Electronic structure measured by ARPES at the photon energy of 70 eV for (a)-(b) SL MoS₂ and (c)-(d) BL MoS₂. The data in (a),(c) are cuts along the \bar{K} - $\bar{\Gamma}$ - \bar{K}' direction of the MoS₂ Brillouin zone, while (b)(d) present cuts along \bar{M} - $\bar{\Gamma}$ - \bar{M} . The MoS₂ (black) and graphene (blue) hexagonal BZs and cut directions are shown in the insets. The solid red lines in (a),(b) correspond to the calculated electronic bands for the free-standing SL MoS₂, after [27].

The valence bands of the SL and BL MoS₂ graphene heterostructures are measured by means of ARPES using 70 eV photons, as shown in Fig. 5.7. We directly measure the dominant orientation of the hexagonal SBZ of MoS₂ rotated by 30° with respect to the graphene SBZ (see insets in Fig. 5.7). A cut along the \bar{K} - $\bar{\Gamma}$ - \bar{K}' direction of MoS₂ is presented in Fig. 5.7(a). Immediately striking are the intense VB maxima around $\bar{\Gamma}$ and \bar{K} and the overall remarkable agreement between the experimental dispersion and the calculated band structure for the free-standing MoS₂ (red lines) [27]. Our measurements completely reproduce the prediction of the global VBM at \bar{K} being displaced 0.1 eV higher than the local VBM at $\bar{\Gamma}$. We are not able to resolve the spin split bands at \bar{K} , which we attribute to the aforementioned different rotational domains of MoS₂. We do not observe any apparent signatures in the electronic structure from the MoS₂ on buffer layer regions, which is expected because MoS₂/G/SiC areas dominate in our samples, as seen in STM. The clear dispersion of the Dirac states around the \bar{K} points of graphene in Figs. 5.7(b),(d) ensures that there is SL graphene under MoS₂, as the buffer layer does not exhibit the linear Dirac bands [137]. In the \bar{M} - $\bar{\Gamma}$ - \bar{M} direction of MoS₂ shown in Figs. 5.7(b),(d) we find a similarly good agreement with the theoretical dispersion. It is noticeable that the bands are extinguished at increasingly negative k_{\parallel} but enhanced toward increasingly positive k_{\parallel} . This asymmetric behavior of the photoemission intensity between the lower and upper halves of the BZ is purely an effect of the angular dependence of the MoS₂ photoemission matrix elements. These influence the measured intensity due to the varying angle of incidence between the incoming electric field and the Mo 4*d* and S 3*p* orbitals that make up the VB states [189].

The overall intensity of the features in the BL sample shown in Fig. 5.7(c)-(d) appears higher than that for the SL sample, which can be understood basically from the higher coverage. The main difference in the dispersion for the BL MoS₂ sample is the shift of the VB global maximum to $\bar{\Gamma}$, which is caused by the appearance of an additional band. Indeed, the splitting of the bands at $\bar{\Gamma}$ is a direct consequence of the inter-layer coupling. For a similar MoSe₂, DFT calculations predict formations of n bands at $\bar{\Gamma}$ for n -layer system, merging eventually into a continuum for the bulk. [143].

In contrast to micro-ARPES measurements of exfoliated MoS₂ flakes on a thin SiO₂ substrate, we do not observe a substrate-induced compression of the overall VB bandwidth [159]. The band structure at $\bar{\Gamma}$ does not seem to be strongly modified, contrary to the observations for MoS₂/Au(111). The lack of such substrate-induced effects on the graphene/SiC template applied here shows that the Mo 4*d* and S 3*p* atomic orbitals are much less affected by the underlying electron system of graphene. This is further substantiated by the lack of hybridization between the Dirac states of graphene and the MoS₂ VBs in Figs. 5.7(a),(d). Nevertheless, in case of CVD-grown flakes transferred onto a graphene/SiC substrate some small effects on the graphene dispersion were observed [190]. These consist of mini-gaps on the π -band for binding energies of ca. 5 eV, exclusively for the case of specific rotation (6°) between the lattices. This effect is accounted to the formation of a distinct moiré pattern, which can lead to openings of mini-gaps. [164]. We do not observe any indications of this behavior; probably due to a small size of crystallites exhibiting multiple rotations between the lattices.

The actual 2D character of the electronic states is essential for the vast majority of the electronic properties of SL MoS₂ [191], which has prompted us to study these states in further detail by following their dispersion with photon energy, as shown in Fig. 5.8. We focus on the states around $\bar{\Gamma}$, because these exhibit the most dramatic change of shape between SL and BL samples. Constant momentum cuts taken in the BZ center show three bands of constant intensity throughout low (18-30 eV) and high photon energy (45-70 eV) ranges for SL MoS₂ in Fig. 5.8(b). The local VB maximum is located at a binding energy of 1.9 eV. In the BL case, the additional

fourth band has its maximum at a binding energy of 1.3 eV, as seen in Fig. 5.8(c). The complete lack of dispersion with the photon energy of all the bands in the measured binding energy range indicates that these electronic states belong to the MoS₂ and that these states can indeed be considered genuinely two-dimensional in our heterostructure samples. Strong oscillations in the relative intensities of the bands are detected with pronounced maxima in intensity of the main VB at a binding energy of 1.9 eV for photon energies of 25, 50, and 70 eV. This behavior is analogous to the layer-dependent band structure changes observed for multilayer graphene, where the intensity resonances for the bulk case emerge as the number of layers is increased [192]. Here, this bulk character of the bands is already becoming evident with the addition of the second MoS₂ layer.

The differences in appearance of all the studied VBs at specific photon energies are illustrated for SL MoS₂ in Fig. 5.8(a) and BL MoS₂ in Fig. 5.8(d). The cuts have been taken in a direction of the BZ around $\bar{\Gamma}$, where the intensity is symmetric. In the lower photon energy range in Fig. 5.8(a),(d), these cuts show the bands at higher binding energies with stronger intensities than in the cuts extracted from the higher photon energy range or in Fig. 5.7. We note that in the SL case these bands are again perfectly consistent with the calculation for free-standing SL MoS₂ [27], while in the BL case, subtle differences in the dispersion can be seen. The BL character around $\bar{\Gamma}$ is unmistakable at a photon energy of 62 eV, where the two topmost bands are equally intense. We notice that at photon energies of 19 and 50 eV the topmost BL band is much harder to detect. This deceiving behavior of the photoemission intensity with the photon energy is essential to take into account when characterizing the layer-dependent electronic structure of MoS₂. Here, we have provided a scheme to clearly distinguish the electronic structures of SL and BL MoS₂ on graphene.

5.3 SL WS₂

5.3.1 Semiconducting SL WS₂ on Au(111)

The interest in studying 2D TMDCs is largely stemming from the significant spin-splitting of the band structure. Therefore, it is important to investigate the effect of the spin-orbit coupling on the dispersion of those materials. We follow this direction by comparing the electronic structure of SL WS₂ synthesized on Au(111) against a similar MoS₂/Au(111) system. Such an approach, enables us to largely isolate the influence of spin-orbit interaction, as both of those materials share similar structural and electronic properties: both of those materials crystallize in virtually the same structure (lattice constant difference <0.2%) [146, 193] and band structure calculations carried without SOC yield almost the same results [27]. However the strength of SOC differs substantially and needs to be taken into account. Interestingly, only after inclusion of SOC the valence band maximum is found at \bar{K} for both SL MoS₂ and WS₂ [27]. This, in turn, results in a direct band gap observed for both of those materials.

Before proceeding with ARPES results, it is worth mentioning previous studies of SL WS₂. The first ARPES characterization of SL WS₂ grown on graphite was shown by Klein *et al.* in 2001 [194]. Although the VBM is found at \bar{K} and spin-splitting of the bands is clearly visible in the presented data, authors' interpretation of the results is disputable. Lead by calculations neglecting SOC [194], authors attributed obtained results to the artificial strain originating from the substrate interaction. Such an interpretation may be called into question in a view of presented data here.

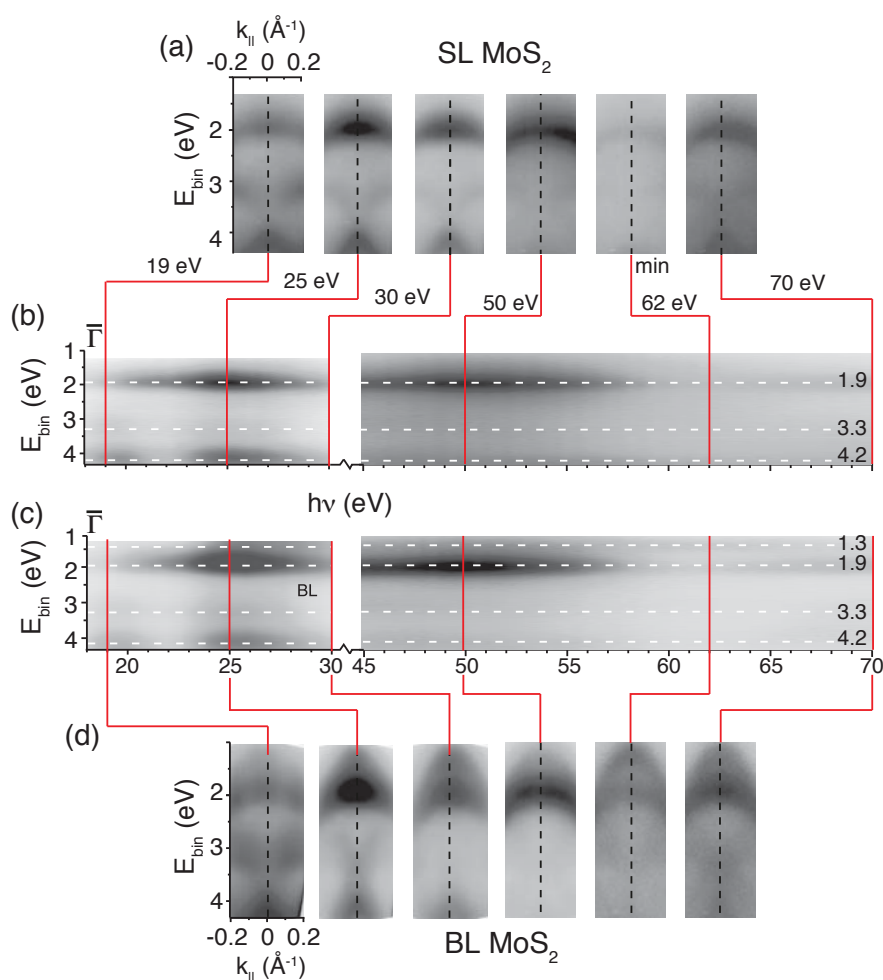


Figure 5.8: Photon-energy-dependent ARPES measurements, showing the dispersion and intensity variation of the electronic states around $\bar{\Gamma}$ for (a),(b) SL MoS₂ and (c),(d) BL MoS₂. In (a),(d), snapshots of the k -dependent dispersion around $\bar{\Gamma}$ are given at selected photon energies for SL MoS₂ and BL MoS₂, respectively. In (b),(c), the photon energy dependence of the photoemission intensity of the states at $\bar{\Gamma}$ is shown for SL MoS₂ and BL MoS₂, respectively. Dashed white lines in (b),(c) mark nondispersive states at the energies given to the right in electronvolts.

The samples for ARPES measurements presented in this section were synthesized *in situ*, at the SGM3 endstation. The coverage of SL WS₂ was chosen to be well below a complete monolayer (ca. 0.7 ML) in order to ensure the lack of BL regions. ARPES measurements were carried out at a temperature of ca. 110 K, with energy and angular resolutions better than 20 meV and 0.2°, respectively. Measurements were taken with photon energies in the range of 14–80 eV. The observed constant energy contours around the \bar{K} point were compared with DFT calculations of electronic structure of free-standing SL WS₂ performed by the group of Prof. Bjørk Hammer (Aarhus University). Computational details of those calculations can be found in Ref. [113].

We start the discussion on the electronic structure with an analysis of the obtained XPS data. Figure 5.9 shows core-level spectra illustrating the local chemical changes accompanying the adsorption of WS₂ on Au(111). All spectra were analyzed by the subtraction of a Tougaard-type background [195] and subsequently fitted by Lorentzian profiles [196]. Before the growth, the Au 4*f* core-levels of the clean Au(111) crystal were measured as a reference (Fig. 5.9(a)). A fit reveals a bulk component and a surface-shifted component at lower binding energy, in good agreement with the literature [196]. The growth of approximately 0.7 ML of WS₂ was found to affect the Au 4*f* core-levels as shown in Fig. 5.9(b). The surface component intensity is largely reduced and shifted towards the bulk component by 58(32) meV with respect to clean Au(111). It is difficult to analyze this spectral change in detail, as there are several factors contributing to it. The first is the actual suppression or shift of the surface core-level component due to the interaction with the sulphur. The second is the remaining presence of clean Au(111) patches that should give rise to a much weaker but largely un-shifted surface component.

The W 4*f* core-level spectrum consists of a spin-orbit split doublet with each peak showing an intense high binding energy component and a weak low energy component. The observed binding energies for the main components are $E_{5/2} = 34.85(0.02)$ eV and $E_{7/2} = 32.72(0.01)$ eV. The spin-orbit splitting of the states is thus 2.13(0.02) eV. These values are consistent with measurements on other WS₂ systems [145, 197, 198]. However, there is a clear difference between the spectra here and those previously reported for smaller nano-scale WS₂ islands on Au(111) [145], for which two almost equally strong components were found in each spin-orbit split peak of the W 4*f* core-level. Those findings were interpreted in terms of core-level components from the edges as well as from the basal plane of the WS₂ nanoislands, consistent with findings for MoS₂ nanoislands [199]. This interpretation is supported by our result of only one main component, as the number of edge atoms with lower coordination is small for the high coverage realized here. The weak low binding energy component observed in Fig. 5.9(c) might stem from edge atoms, or from the presence of W atoms in lower oxidation states, probably due to not fully sulfidized regions WS_{2-x} [145, 197]. The presence of metallic W(0) or W(+II) is not observed.

ARPES results for the electronic structure of SL WS₂/Au(111) along different high symmetry directions of the Brillouin zone are shown in Fig. 5.10(a). Corresponding constant energy contours are presented in Fig. 5.10(b). Features attributed to Au(111), such as the surface state [161], *sp* bulk bands and projected bulk gap edges [97], are marked in Fig. 5.10(a).

The uppermost valence band of SL WS₂ is discernible for binding energies larger than 1.2 eV, especially between $\bar{\Gamma}$ and \bar{K} and towards \bar{M} . The band is significantly sharper within the projected bulk band gaps of Au around \bar{K} (outlined by dashed lines) than near $\bar{\Gamma}$ and \bar{M} . Near \bar{M} the WS₂ states strongly hybridize with the gold continuum and cannot be discerned. At $\bar{\Gamma}$, the state is clearly visible as a broad maximum in the photoemission intensity at a binding energy ≈ 0.51 eV higher than at \bar{K} , consistent with the expected direct band gap at \bar{K} . The observation of a single valence band at $\bar{\Gamma}$ with a higher binding energy than at \bar{K} also rules out

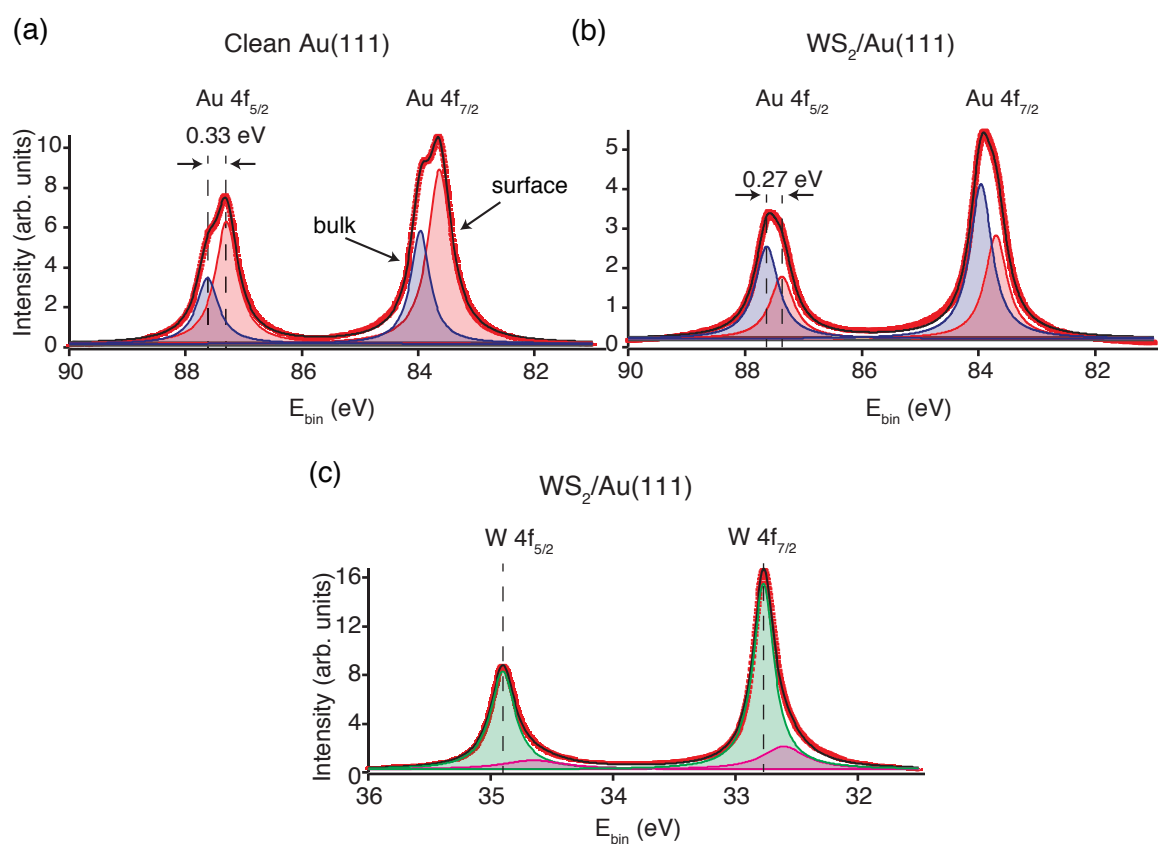


Figure 5.9: (a-b) Au_{4f} core-levels for clean Au(111) and ≈ 0.7 ML of WS₂/Au(111), respectively. Blue and red peaks correspond to bulk and surface components, respectively. (c) W_{4f} core-levels from SL WS₂. Small peaks observed at lower binding energy (in magenta) indicate the presence of W atoms with lower oxidation states (WS_{2-x}).

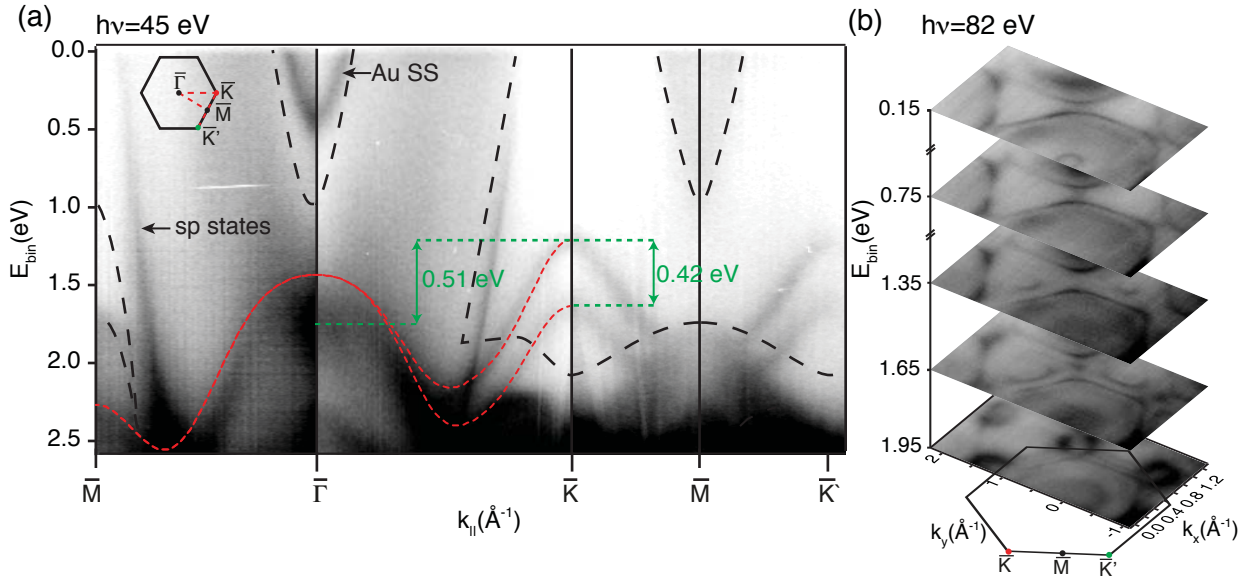


Figure 5.10: (a) ARPES spectra of SL WS₂ on Au(111) along high-symmetry directions shown in the inset. The well-defined contribution from the Au surface state (SS) and the *sp* bands are indicated in the image. The projected bulk band gaps of Au(111) [97] are outlined by dashed black lines. The energy differences between the valence-band extrema at $\bar{\Gamma}$ and \bar{K} (0.51 eV) and the spin-splitting of the bands at \bar{K} (0.42 eV) are marked with dashed lines. The corresponding peak positions are determined by fitting Lorentzian profiles to the energy distribution curves. The theoretical dispersion (after Ref. [27]) for the free-standing SL (red dashed line) is superimposed on the data. (b) Photoemission intensity along constant energy contours throughout the surface Brillouin zone at different binding energies.

a significant contribution from BL WS₂, as discussed in Section 5.2.

The overall observed dispersion of the band structure is in good agreement with calculations for the free-standing SL WS₂ (red dashed lines) [27], notably around \bar{K} . Divergence from these calculations in terms of a shift towards higher binding energy is seen near $\bar{\Gamma}$, similar to what we previously observed for SL MoS₂/Au(111), where we explained it in terms of an interaction with the substrate. Here, analogical arguments based on the orbital character of the bands also hold: the bands around $\bar{\Gamma}$ are a mixture of out-of-plane W d_{z^2} and S p_z orbitals, which can participate in bond formations with the Au and as a result change the band dispersion [27]. In contrast to this, the valence bands at the \bar{K} points are derived mainly from in-plane W d_{xy} and $d_{x^2-y^2}$ orbitals. These are not only less likely to be affected by the interaction with the substrate, but they are also situated in a projected bulk band gap.

Perhaps the most interesting feature of the SL WS₂ valence band structure is the large spin-splitting, especially at the \bar{K} points. In a simple picture, the size of the splitting strongly depends on the atomic spin-orbit splitting and it is thus expected to be significantly larger for W- than for Mo-based TMDCs. We investigate the spin-splitting of SL WS₂ near \bar{K} in more detail using the data in Fig. 5.11, which shows a spin-splitting of the valence band extrema of $\Delta E_{VB}=419(11)$ meV (Fig. 5.11(b)). This does indeed greatly exceed the value observed for SL MoS₂/Au(111) ($\Delta E_{VB}=145(4)$ meV), and is in good agreement with theoretical predictions [27, 200] and with values measured for analogous exfoliated materials [201]. Among the semiconducting TMDCs, only SL WSe₂ ($\Delta E_{VB}=462$ meV) is expected to exhibit a larger spin-splitting [27, 53], something that was confirmed experimentally with ARPES measurements [202].

The complete mapping of the bands around \bar{K} not only permits a determination of the spin-

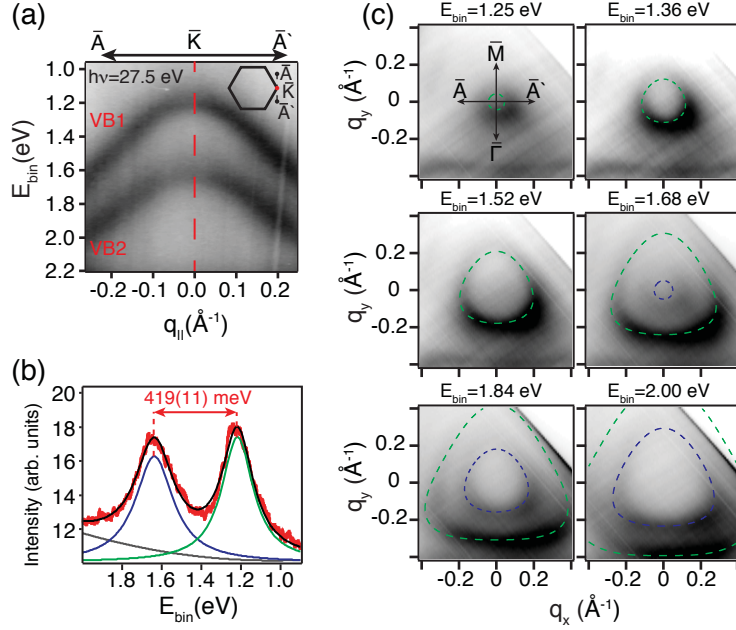


Figure 5.11: (a) ARPES spectrum of SL WS₂ on Au(111) along the $\bar{A}-\bar{K}-\bar{A}'$ direction, as indicated in the inset. (b) Energy distribution curve through the \bar{K} point (red dashed line in (a)) fitted with two Lorentzian profiles and quadratic background. (c) Constant energy contours close to the \bar{K} point with superimposed results of DFT calculations for the free-standing SL WS₂ (dashed lines). The q_x and q_y coordinates have \bar{K} as origin. Green and blue lines refer to the upper and lower valence band, respectively.

splitting at the high symmetry point but also of the directional dependence of the band structure, which has implications for the effective mass tensor. To this end, Fig. 5.11(c) shows a comparison of the constant energy contours (CECs) obtained with ARPES near \bar{K} and corresponding DFT calculations for free-standing SL WS₂. The calculated band structure has been aligned with the experimental data such that the top of the upper valence band is placed at the same energy. The agreement is excellent, confirming that the low energy dispersion around \bar{K} is not significantly affected by the substrate. A closer look at the CECs reveals an anisotropy of the valence band dispersion around \bar{K} , visible as a trigonal warping (TW). This effect is theoretically predicted and in the simplest approximation can be described as a third order correction to the parabolic energy dispersion [53]. In the $\mathbf{k} \cdot \mathbf{p}$ formalism, it is caused by the interaction terms between the uppermost valence band with the lower lying valence bands [27, 54]. TW reflects the underlying three-fold rotational symmetry of the crystal structure. It should be noted that this effect is connected to the general electronic structure rather than to the relativistic spin-orbit coupling: thus, for example, it is also present for graphite and graphene where spin-orbit coupling is negligible [203, 204].

Given the constraint that the spin-splitting has to vanish at $\bar{\Gamma}$ and \bar{M} , the size of the splitting at \bar{K} can be expected to indirectly affect the band curvature of the valence band maximum and thus the hole effective mass of the material. This is investigated by determining the effective masses near \bar{K} . For consistency with calculations [53] and to avoid the problem of a directional dependence due to the TW, the effective mass has been fitted in a region very close to the \bar{K} point ($\approx 0.07 \text{ \AA}^{-1}$) along the $\bar{\Gamma}-\bar{K}-\bar{M}$ direction. This procedure leads to hole effective masses for VB1 and VB2 (defined in Fig. 5.11(a)) as $m_{\text{VB1}} = 0.40(02)m_e$ and $m_{\text{VB2}} = 0.57(09)m_e$, respectively. The same fitting procedure applied for SL MoS₂/Au(111) yields $m_{\text{VB1}} = 0.55(03)m_e$ and $m_{\text{VB2}} = 0.67(04)m_e$. The effective mass of the uppermost valence band is therefore indeed reduced, consistent with the naive expectation (even though the most simple picture does not explain

why $m_{\text{VB}2}$ is also reduced). All these values are in good agreement with calculations [53].

Finally, an interesting difference between the data presented here and that discussed previously for SL MoS₂/Au(111) is the very clear presence of the Au(111) surface state near $\bar{\Gamma}$ seen in Fig. 5.10. For SL MoS₂/Au(111), only a very faint signature of this state was observed. This difference is ascribed to the slightly different preparation procedure. In the present work, the synthesis and all the analysis were performed in a single UHV system without ever exposing the sample to air. In the previous work for SL MoS₂/Au(111), synthesis and ARPES were performed in separate UHV systems, and the sample was transferred between them through air. After such a transfer, atomically clean SL MoS₂ can be recovered by a brief anneal, and the measured electronic structure of the layer is not affected. This, however, is not necessarily the case for the remaining uncovered Au(111) terraces, where the surface state might remain quenched by adsorbed contaminants — at least, this may be the case for the low annealing temperature of ca. 200°C. The observed surface state in Fig. 5.10 is thus likely to be located on the remaining clean terraces and not under the SL WS₂. In fact, when preparing MoS₂ on Au(111) and measuring without an exposure of the sample to air, the surface state is also observable in ARPES.

5.3.2 Metallic SL WS₂ on Ag(111)

Applications of 2D TMDCs in electronic devices requires finding an efficient way of connecting metallic electrodes in order to avoid a formation of the Schottky barrier. In fact, contact resistance was identified as a dominating factor influencing the performance of TMDC-based transistors [205]. One of the suggested solutions of decreasing Schottky barrier height was the usage of a low work function metal contact [152]. However, our previous results showed that interaction with a metallic substrate is far from trivial and can induce complicated changes in the band structure of 2D TMDCs, which necessitates further research in this direction. In this section we present ARPES measurements of SL WS₂ synthesized on Ag(111). We compare the obtained results to SL WS₂ grown on Au(111), which has a significantly higher work function than Ag(111). Further, Ag and Au have nearly identical lattice constant which is important to minimize the possibility of the strain-induced effects. It is predicted that already 1% of strain destroys the direct band gap in SL WS₂ [155].

The samples for ARPES measurements presented in this section were synthesized *in situ*, at the SGM3 endstation. The coverage of SL WS₂ was chosen to be well below a complete monolayer (ca. 0.7 ML). ARPES measurements were carried out at a temperature of ca. 100 K, with energy and angular resolutions better than 20 meV and 0.2°, respectively. Measurements were taken with the photon energy in the range of 25-140 eV.

Figure 5.12 presents an overview of the measured dispersion. High binding energy of Ag bulk bands near \bar{M} enables us to follow unambiguously the whole uppermost valence band of SL WS₂. The measured dispersion is in a reasonable agreement with calculations of free-standing SL WS₂. Divergence from these calculations is seen near $\bar{\Gamma}$, similar to what we previously observed for SL WS₂/Au(111). We attribute this effect to the substrate-induced orbital hybridization, as discussed in Sect. 5.3.1. The observed dispersion is very similar to the SL WS₂/Au(111), however exhibits some notable differences. The bands seem to be sharper for WS₂/Ag(111), which we attribute to the higher quality of the epilayer grown on Ag(111). The spin-splitting at \bar{K} (412(10) meV) is found somewhat smaller, but within the measurement uncertainty. The state at $\bar{\Gamma}$ is visible as a broad maximum at the binding energy ≈ 0.54 eV below than at \bar{K} , which is slightly larger than for the case of SL WS₂/Au(111). Overall, the WS₂ VB edge is found shifted towards higher binding energy by ca. 0.26 eV in respect to SL WS₂/Au(111). The

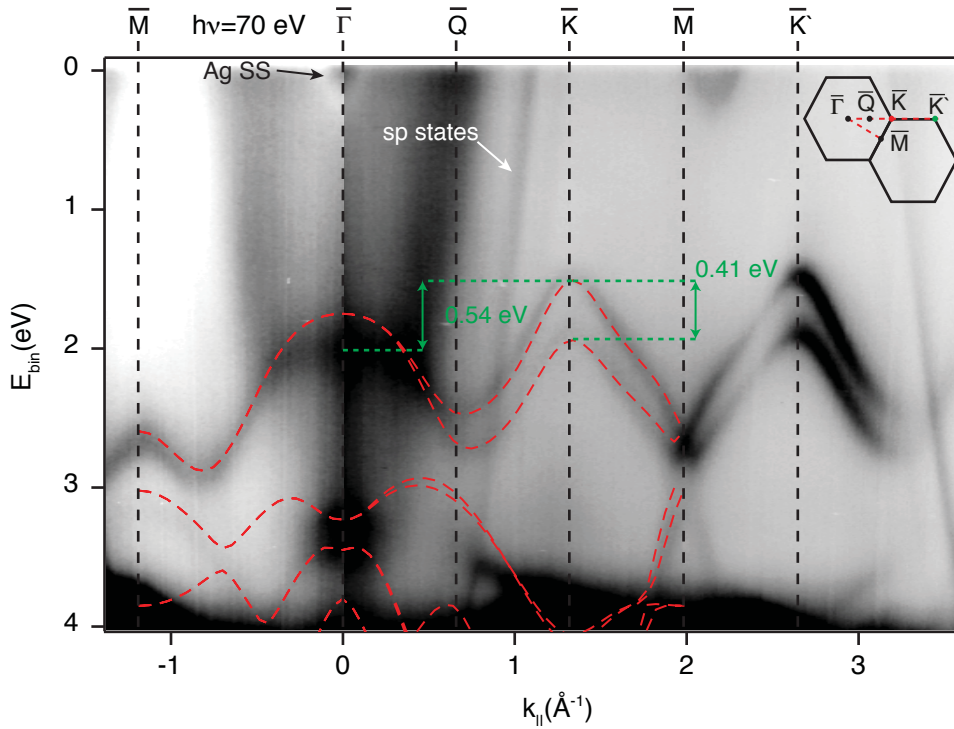


Figure 5.12: ARPES spectra of SL WS₂ on Ag(111) along high-symmetry directions shown in the inset. The well-defined contribution from the Ag surface state (SS) and the *sp* bands are indicated in the image. The energy differences between the valence-band extrema at $\bar{\Gamma}$ and \bar{K} (0.54 eV) and the spin-splitting of the bands at \bar{K} (0.41 eV) are marked with dashed lines. The corresponding peak positions are determined by fitting Lorentzian profiles to the energy distribution curves. The theoretical dispersion (after Ref. [113]) for the free-standing SL (red dashed line) is superimposed on the data. Data taken with the photon energy of 70 eV.

origin of such a strong band realignment is not clear. It is predicted that even without a net charge transfer between a metal substrate and an adsorbate, the surface charge repulsion effect can drive the charge redistribution within the two contacted materials [153].

An interesting difference between SL WS₂ grown on Ag(111) and Au(111) is emergence of an additional band crossing the Fermi level between $\bar{\Gamma}$ and \bar{K} (\bar{Q} point). This is not seen very clearly in Fig. 5.12 due to the high intensity of Ag *d*-bands at this photon energy. We study the band structure further by using the photon energy of 25 eV, at which Ag bulk bands are observed with much lower intensity. Figs. 5.13(a),(c) shows the ARPES data with a small electron pocket around \bar{Q} clearly resolved. This band was not observed neither in the case of SL WS₂/Au(111) (see Figs. 5.13(b),(d)), nor in the case of clean Ag(111) (data not presented here).

DFT calculations predict that with a small strain (1%) the CBM indeed shifts towards \bar{Q} [155]. However, we can exclude the strain larger than 0.7% based on the LEED data, as discussed in Sect. 4.4. Furthermore, if the CBM was at \bar{Q} due to the strain, one would expect to observe also the CB at \bar{K} close to the Fermi level. tr-ARPES measurements performed on SL WS₂/Ag(111) shows, however, that CB edge at \bar{K} is ca. 0.5 eV above the Fermi-Level [206]. For that reason, the most likely interpretation seems to be the substrate-induced band hybridization. Recently, it was proposed that interfacing SL MoS₂ with a metal contact can lead to a formation of the interface gap states [152, 153]. In simple terms, those states can be described as decaying metallic wave functions into the semiconductor [207, 208]. The metal-induced gap states are

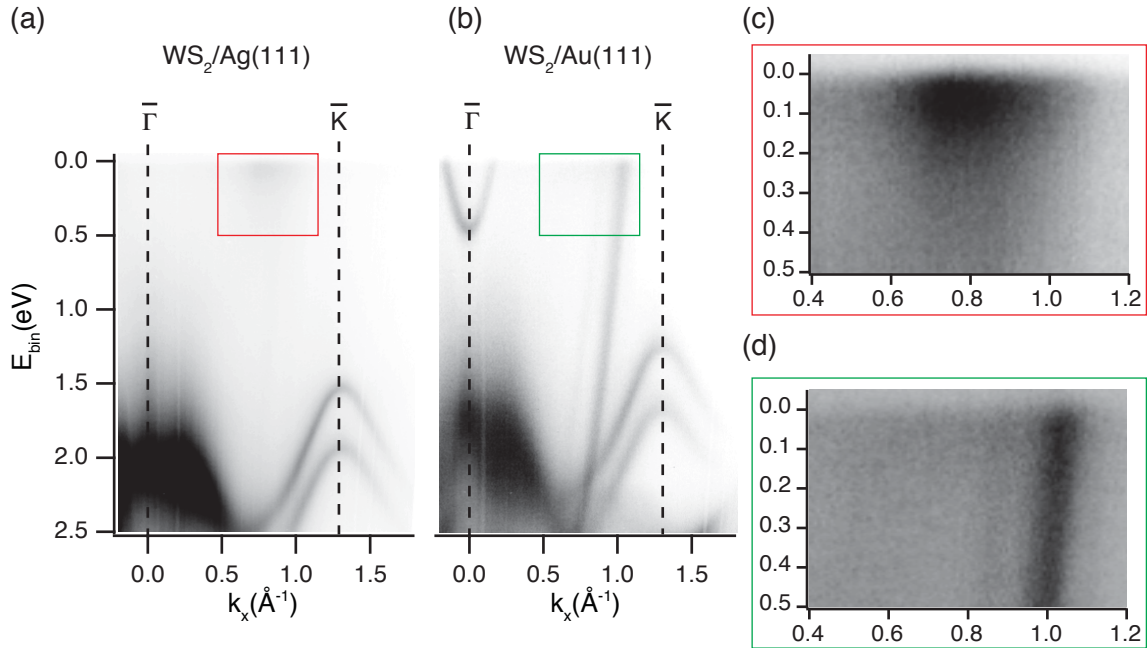


Figure 5.13: (a)-(b) ARPES spectra along the $\bar{\Gamma}$ - \bar{K} direction for SL WS₂ on Ag(111) and SL WS₂ on Au(111), respectively. Red and Green rectangles in (a)-(b) mark the dispersion regions presented in (c)-(d), respectively. Note that the contrast has been enhanced in (c)-(d) for better visibility. Measurements taken with the photon energy of 25 eV.

well-known to arise at the metal-semiconductor interface and have a crucial role on the Fermi level pinning [153].

CB edge at \bar{Q} originate from the in-plane d_{xy} and $d_{x^2-y^2}$ orbitals [53], so the direct interaction with the substrate is rather not expected [153]. Gong *et al.* [153] proposed an unusual mechanism for the gap states formation in a SL MoS₂-metal junction. They proposed that substrate-S bonding can weaken the intralayer S-Mo bonding, and thus Mo d states can penetrate into the band gap [153]. This explanation is likely to hold also for similar WS₂ and it seems to explain our observations. The reason why this effect is not observed for WS₂/Au(111) might be a weaker Au-S interaction.

The above explanation is further corroborated by XPS measurements, as presented in Fig 5.14. The W $4f$ core-level spectrum for SL WS₂/Ag(111) can be described in terms of 4 peaks, which we attribute to WS₂ (main components) and a small contribution from edge atoms or not fully sulfurized regions WS_{2-x}, as discussed in Sect. 5.3.1. We find the main components shifted by ca. 0.15 meV towards higher binding energy in comparison to the corresponding peaks obtained on WS₂/Au(111) (see Fig 5.14(a)). Such a shift is consistent with VB relocation and might stem from the charge redistribution between WS₂ and Ag(111). Most importantly, we find the shape of peaks to be asymmetric. While in the case of WS₂/Au(111) the peaks can be fitted with plain Lorentzians, in the case of WS₂/Ag(111) we observe the characteristic high-binding-energy tail (see Fig 5.14(b)). The fit using Doniach-Šunjić profiles [73] with a Tougaard-type background [195] reveals the asymmetry parameter of ca. 0.07 for all the components (see Fig 5.14(a)). In a simple picture, a core-hole can act as a potential which scatters the conduction electrons [70]. This leads to the characteristic tail towards higher binding energy, described by Doniach-Šunjić profile. The presence of this effect in the observed W $4f$ core-level spectrum is thus likely to originate from W electrons occupying the states close to the Fermi energy. In fact, this mechanism was proposed to describe the asymmetry in $4f$ core-level spectra of metallic

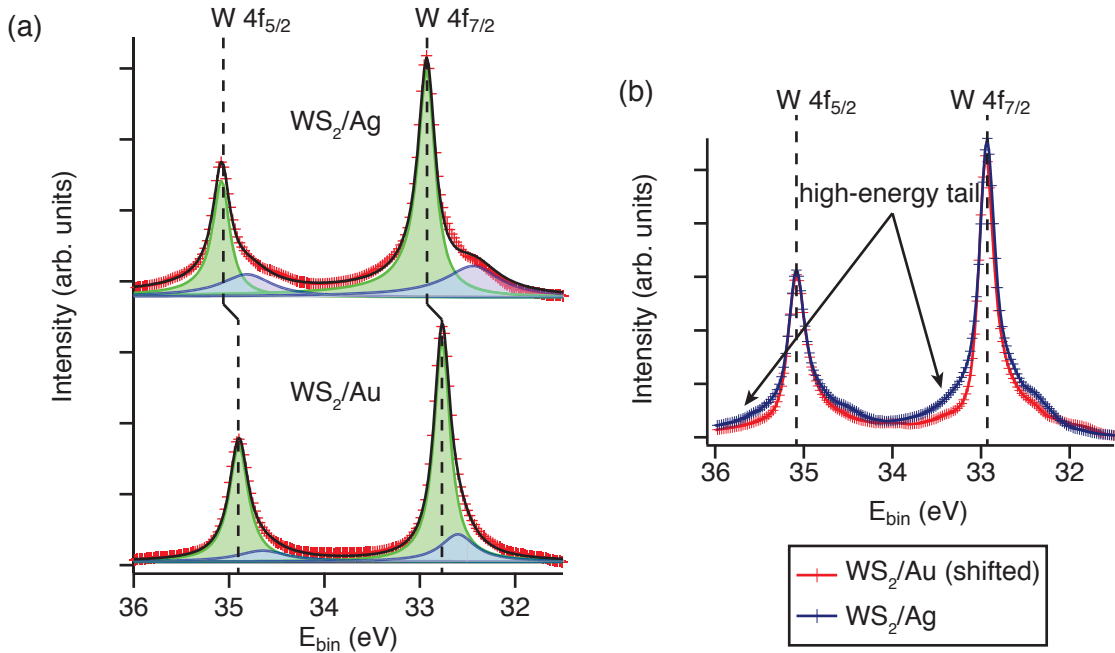


Figure 5.14: (a) W_{4f} core-levels from SL WS₂ on Ag(111) and SL WS₂ on Au(111), as indicated in the graph. Small peaks observed at lower binding energy (in magenta) indicate the presence of W atoms with the lower oxidation states (WS_{2-x}). (b) The same data as in (a), but aligned for better comparison of the peak profiles.

TaS₂ [209, 210].

5.4 Suppression of CDW in SL TaS₂ on Au(111)

In contrast to MoS₂ and WS₂, a free-standing TaS₂ is metallic due to the unpaired *d*-electron. In bulk, metallic TMDCs host a wide range of symmetry-breaking electronic instabilities, such as charge density waves, superconductivity, and Mott states [6,7]. However, it still remains an open question how these would change in the SL limit. This has been explored theoretically [157, 211] and, very recently, experimentally for SL TiSe₂ [212, 213] and SL NbSe₂ [37, 214]. STS measurements of SL TaS₂ on Au(111) reveals that CDW is quenched, or at least highly suppressed. Here we study the electronic structure of SL TaS₂ in order to elucidate this effect.

The samples for ARPES measurements presented in this section were synthesized *in situ*, at the SGM3 endstation. The coverage of SL TaS₂ was chosen to be below a complete monolayer (ca. 0.7 ML). ARPES measurements were carried out at the temperature of ca. 95 K, with energy and angular resolutions better than 20 meV and 0.2°, respectively. Measurements were taken with the photon energy of 30 eV. DFT calculations of electronic structure for free-standing 1H and 1T SL TaS₂ were performed by the group of Prof. Bjørk Hammer (Aarhus University). Computational details of those calculations can be found in Ref. [112]. STM and STS measurements were performed at the temperature of 4.7 K, in a collaboration with the group of Prof. Alexander Khajetoorians.

The ARPES data in Fig. 5.15 reveal the electronic band structure close to the Fermi level. In addition to the features arising from the exposed Au substrate (in particular, the Au surface state at $\bar{\Gamma}$ and the Au *sp* states closer to the edge of the Brillouin zone (BZ)), the TaS₂ overlayer

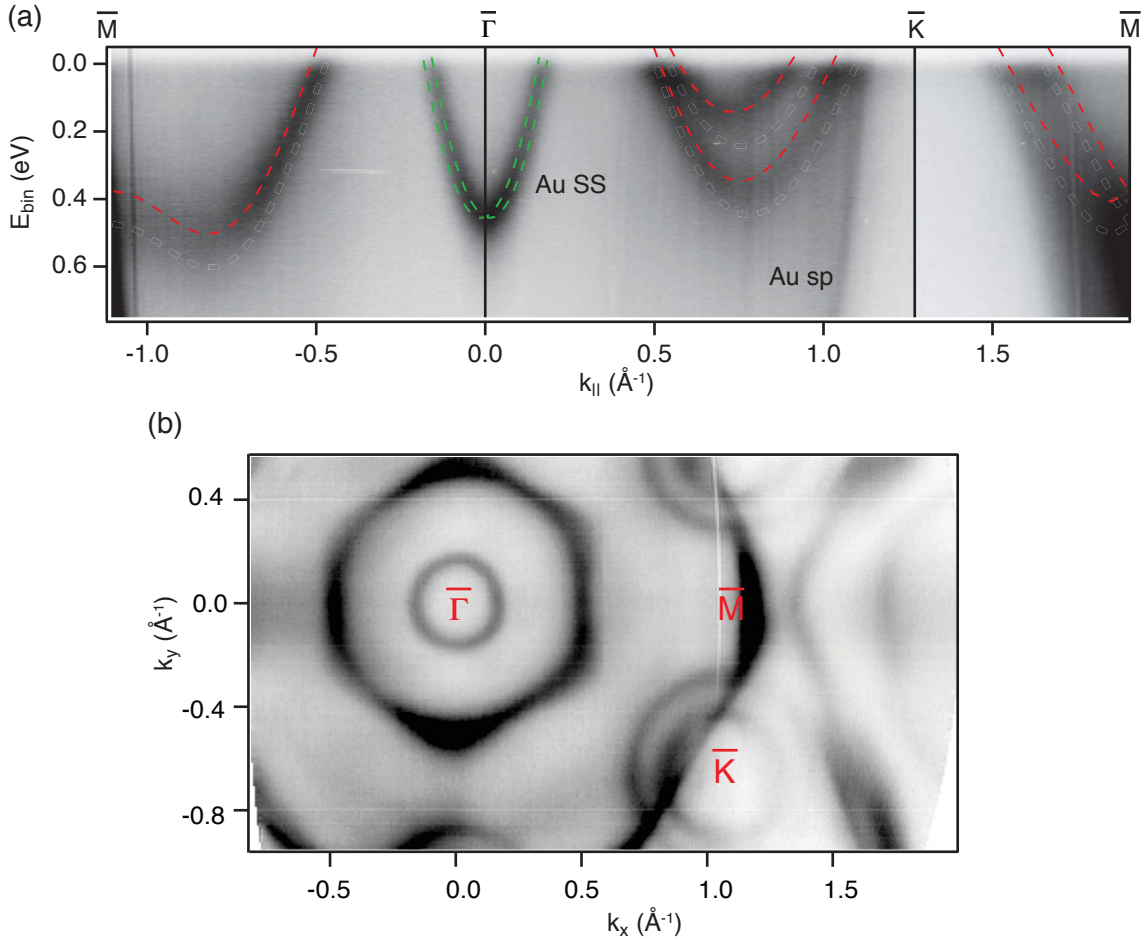


Figure 5.15: (a) ARPES spectrum of SL TaS₂ on Au(111) along the high-symmetry directions. The well-defined contribution from the Au surface state (SS) and the *sp* bands are indicated in the image. The results of SS fitting performed on clean Au(111) before the growth (green dashed line) and the theoretical dispersion for the free-standing SL (red dashed line) are superimposed on the data. Theoretical dispersion has been shifted by 0.12 eV to higher binding energy. (b) Photoemission intensity at the Fermi energy. Measurements taken with the photon energy of 30 eV.

exhibits a Fermi contour (Fig. 5.15(b)) consisting of two distinct features. The first is an apparently hexagonal contour around the BZ center $\bar{\Gamma}$. The second consists of two concentric rings around the \bar{K} point.

The predicted band structures of 1T and 1H phases differs significantly (see Fig. 1.5), which enables the phase identification based on ARPES data. Clearly, the band structure for the 1H modification gives better qualitative agreement with the experimental data. The quantitative agreement can be obtained when the calculated bands are shifted by 0.12(2) eV to a higher binding energy to account for electron doping, as shown in Fig. 5.15(a). Furthermore, the observed Fermi surface (Fig. 5.15(b)) agrees well with the calculations performed for doped free-standing SL 1-HTaS₂ (Fig. 5.16(c)). Based on this comparison, we conclude that the structural phase preferred by epitaxial TaS₂ on Au(111) is 1H, rather than 1T.

Overall, the dispersion of SL TaS₂ strongly resembles the dispersion of heavily n-doped SL WS₂. The observed bands crossing the Fermi level stem from the same band, which is spin degenerate near $\bar{\Gamma}$ but strongly split near \bar{K} , and thus all Fermi contours are hole pockets. A comparison to the calculated Fermi contours (see Fig. 5.16(c)) reveals that the finite but unresolved splitting

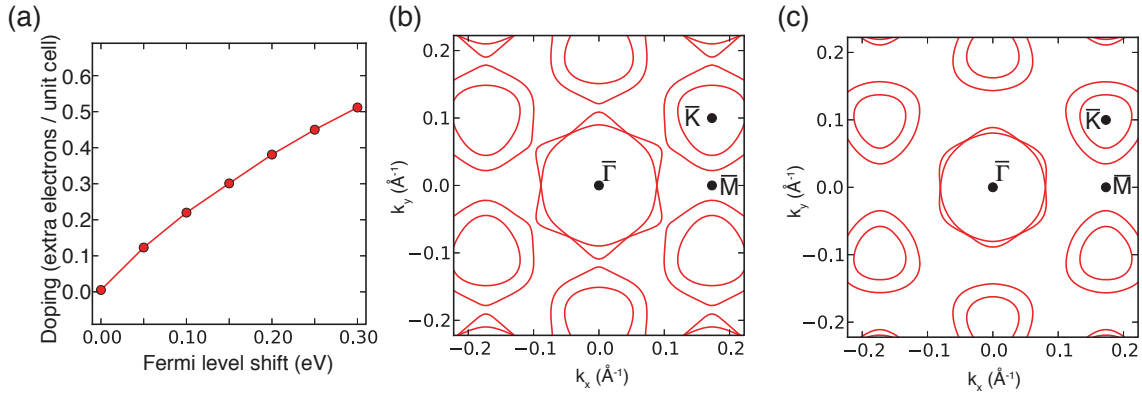


Figure 5.16: (a) Relation between extra top valence band occupation (1 electron / unit cell in the charge-neutral case) and doping (Fermi level shift needed to achieve this occupation) for SL-1H TaS₂. (b)-(c) Calculated Fermi contours for the charge-neutral case and for a doping level of 0.15 eV, respectively.

of the bands near the Fermi contour around $\bar{\Gamma}$ is responsible for the apparently hexagonal shape of this hole pocket, even though the individual bands do not have hexagonal Fermi contours. Replica bands stemming from either moiré or CDW were not observed in the data.

While the band structure of the bulk 2H parent compound can be considered to be quasi-2D, the truly 2D situation in the SL manifests important differences from the quasi-2D bulk case. Particularly relevant are the modifications to the single band forming the Fermi contour of the SL. In the SL, the band is twofold degenerate near $\bar{\Gamma}$ and spin split near \bar{K} . In the 2H bulk, on the other hand, the spin degeneracy is never lifted because of the structure's inversion symmetry. Still, the interaction of the two layers in the unit cell splits the band into two twofold degenerate bands near $\bar{\Gamma}$ while it remains fourfold degenerate at the BZ border point H. This causes a rather strong dispersion perpendicular to the TaS₂ layers, giving rise to a deviation from 2D behavior [215]. Naively, one might thus expect a stronger tendency for the formation of CDW states in the SL, at least for nesting-driven CDWs.

We address the question of whether the grown samples exhibit CDW or SC by inspecting STM/STS data taken at 4.7 K (Fig. 5.17). In bulk 2H-TaS₂, the superconducting critical temperature $T_c = 0.6$ K [216], and a CDW of (3×3) periodicity sets in below 75 K [157], with an accompanying lattice distortion that is clearly visible as a periodic superstructure in the STM data [217] (the same is true for SL NbSe₂ [37]). Low-temperature STM data in Fig. 5.17(a) on the other hand, show no indication of any additional periodicities apart from the lattice as such and the moiré superstructure. This is confirmed by an inspection of the Fourier transformation of the image, which only shows these two periodicities (see Fig. 5.17(b)).

STS measurements made at 4.7 K show a strong feature at approximately 430 meV above the Fermi energy (Fig. 5.17(c)), consistent with results obtained from NbSe₂, where this has been associated with the top of the valence band at $\bar{\Gamma}$ [37]. The spectra give no indications of a SC or CDW gap opening. It is not surprising that SC is not observed, since the critical temperature is much lower than the measurement temperatures used in this study. One set of recent studies has suggested that critical temperature in thin flakes might be higher than the bulk value [218, 219]—in contrast to what has been seen for the case of NbSe₂, where T_c is suppressed in the SL limit [37, 214]—but even the highest proposed temperatures for thin TaS₂ are considerably smaller than the measurement temperatures in this study. The absence of a CDW, however, is surprising. The onset of CDW instability at 75 K in bulk 2H-TaS₂ is significantly above

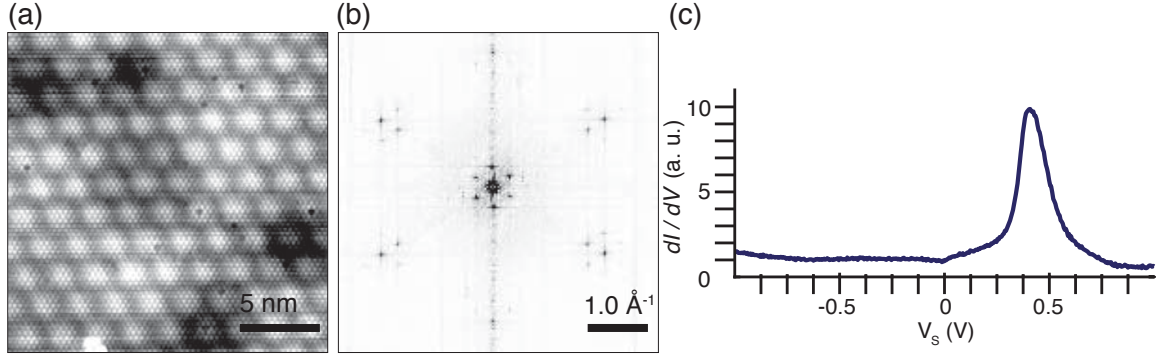


Figure 5.17: STM and STS data acquired at 4.7 K revealing the absence of CDW state for SL TaS₂. (a) High-resolution STM image, showing the atomic lattice and moiré superstructure (0.5 nA and 4.3 mV). (b) Fourier transformed data in (a). (c) Representative STS point spectrum ($I_{\text{stab}} = 0.5$ nA, $V_S = 1$ V, $V_{\text{mod}} = 5$ mV, $f_{\text{mod}} = 4423$ Hz)

that at which STM and STS data were acquired. In the related material NbSe₂, there have been conflicting findings for the CDW onset temperature in the SL with respect to the bulk. A strongly increased T_{CDW} was reported for SL NbSe₂ on silicon oxide [214], whereas a minor decrease was observed for SL NbSe₂ in UHV on bilayer graphene[37].

In this context, it is interesting to compare the Fermi vector $2k_F = 0.96(2)^{-1}$ measured across the hole pocket at $\bar{\Gamma}$ with that which would be required if a (3×3) CDW state were driven by nesting: In the nesting-driven case, the nesting vector would need to be 0.73^{-1} . Clearly, this value matches poorly to the experimentally derived value of $2k_F$; however, this disagreement is not sufficient to explain the absence of a CDW, since simple nesting cannot explain the CDW in the bulk parent materials, either [220–222].

The most likely explanation for the lack of CDWs is doping of the TaS₂ by the Au substrate. As already seen in Fig. 5.15(a), the calculated bands have to be shifted to higher energy by 0.12 eV to match the observed dispersion, suggesting that the SL is electron doped. Measurement of the Fermi contour areas gives a carrier concentration of approximately 0.3(1) extra electrons per unit cell —i.e., an occupation of 1.3(1) electrons in the uppermost valence band, in contrast with the single electron that one would expect for the undoped material. This result is consistent with the DFT calculations relating the band-shift with an extra electron occupation, as presented in Fig. 5.16(a). Previous studies of alkali-intercalation compounds [223] have shown that the CDW can already be suppressed at more modest electron doping, suggesting that this plays a decisive role. Nevertheless, such a strong doping observed here is quite surprising taking into account inertness of Au. Recently, Wehling *et al.* proposed a mechanism of pseudo-doping in metallic SL TMDCs [224]. They relate the observed apparent doping with the band hybridization, rather than with the actual electron transfer. The calculated band-shift for SL TaS₂ on Au(111) agrees well with our observations. Furthermore, the proposed pseudo-doping is expected to affect the formation of CDW state [224].

It should be noted that the CDW transition might also be influenced by other factors, e.g., reduced dimensionality; substrate interactions other than doping, such as screening [144, 171]; chemical bonding; or strain [225]. However, the uncertainty in the measurement of the atomic lattice puts an upper limit of ca. 1% on the in-plane strain and Fig. 5.15(a) show that the substrate has only a minor influence on the band structure of SL TaS₂, apart from the doping. However, these factors might still play a minor role in suppressing CDW formation [226].

Chapter 6

Summary

Novel 2D materials were successfully synthesized on a variety of different substrates. The morphology and electronic structure of the grown films were characterized in detail using STM, LEED, ARPES and XPS techniques. Obtained results are in good agreement with DFT calculations and theoretical considerations. In addition, characterizations of the Au(111) substrate itself, shed new light on the well-known herringbone reconstruction. The main findings can be summarized in the following:

- **Au(111) surface electronic structure:** ARPES measurements performed in the higher order SBZ revealed unexpected modifications of the Fermi contours, which are attributed to the herringbone reconstruction present on the surface. The structural model based on an oblique unit cell was proposed in order to explain the findings. Obtained results solve a long-standing discrepancy between predicted changes in the surface electronic structure, confirmed by STS investigations, and their conspicuous absence in photoemission experiments.
- **SL MoS₂:** The prototypical semiconducting 2D TMDC was successfully synthesized on Au(111) and graphene/SiC substrates. SL MoS₂ was found to grow epitaxially on the Au(111) substrate, which was confirmed by STM measurements. High quality and large area of the grown film enabled us to perform detailed ARPES characterizations of the electronic structure of MoS₂. In case of SL MoS₂/Au(111), the measured dispersion is in agreement with the DFT calculation of the free-standing layer, except the region around $\bar{\Gamma}$. Further calculations, which include the contribution of Au(111), explained the results by predicting the substrate-MoS₂ band hybridization. The dispersion around \bar{K} was not found to be significantly affected by the substrate. Doping of SL MoS₂ with alkali metals resulted in the band gap renormalization and the nonuniform shift of the valence band in respect to the Fermi level. In case of the SL MoS₂ synthesized on graphene/SiC, the growth of rotational domains was observed. The preferred orientation of MoS₂ being 30° rotated in respect to graphene was found. The SL MoS₂ band structure around $\bar{\Gamma}$ was found to resemble the free-standing case due to a lack of strong interactions with graphene. The emergence of an additional band, effectively shifting the VBM to $\bar{\Gamma}$, was observed for BL MoS₂.
- **SL WS₂:** The synthesis of SL WS₂ demonstrated the universality of developed growth methods. XPS measurements revealed the presence of not-fully sulfurized regions of WS_{2-x}. Substitution of Mo with much heavier W atoms, enabled to elucidate the effect of SOC on the electronic dispersion of SL TMDCs. The spin-splitting of the WS₂/Au(111) bands at \bar{K} was found to be strongly enlarged in comparison to MoS₂/Au(111). Simultaneously, enhanced SOC leads to a reduction of the hole effective mass at \bar{K} , suggesting that WS₂ might be a better material than MoS₂ for applications in electronics. The dispersion

around \bar{K} was found to be trigonally warped, in good agreement with the DFT calculations for the free-standing layer. ARPES measurements performed on $\text{WS}_2/\text{Ag}(111)$ enabled us to resolve the band structure around \bar{M} . Furthermore, a small electron pocket at \bar{Q} was observed in this case, which *de facto* changes semiconducting WS_2 into a metal. This is corroborated by XPS observations of the asymmetric peak profiles of W $4f$ core-levels, which are attributed to the high density of states at the Fermi level. LEED measurements of the SL WS_2 lattice constant enabled us to exclude the strain-induced origin of those band structure changes. The experimental results point towards the recently proposed mechanism of the substrate-induced in-gap states formation, which predicts the TM d -band modifications mediated by sulfur interactions with the substrate [153].

- **SL TaS₂:** The growth procedure of SL $\text{TaS}_2/\text{Au}(111)$ was successfully modified in order to decrease the amount of domain boundaries and thus increase the quality of TaS_2 . The CDW state was found to be strongly suppressed, which was confirmed by low-temperature STM and STS measurements. This observation is explained by strong doping originating from the substrate. Recent theoretical predictions suggest that the origin of SL TaS_2 doping stem from the band hybridization, rather than the actual charge transfer between TaS_2 and $\text{Au}(111)$ [224].

Bibliography

- [1] R. Peierls, *Annales de l'institut Henri Poincaré* **5**, 177 (1935).
- [2] L. Landau, *Phys. Z. Sowjetunion* **11**, 26 (1937) **11**, 26 (1937).
- [3] N. D. Mermin and H. Wagner, *Physical Review Letters* **17**, 1133 (1966).
- [4] J. C. Meyer, A. K. Geim, M. I. Katsnelson, K. S. Novoselov, T. J. Booth, and S. Roth, *Nature* **446**, 60 (2007).
- [5] A. Fasolino, J. H. Los, and M. I. Katsnelson, *Nature Materials* **6**, 858 (2007).
- [6] P. R. Wallace, *Physical Review* **71**, 622 (1947).
- [7] S. Hagstrom, H. B. Lyon, and G. A. Somorjai, *Physical Review Letters* **15**, 491 (1965).
- [8] J. W. May, *Surface Science* **17**, 267 (1969).
- [9] J. Shelton, H. Patil, and J. Blakely, *Surface Science* **43**, 493 (1974).
- [10] K. S. Novoselov, A. K. Geim, S. V. Morozov, D. Jiang, Y. Zhang, S. V. Dubonos, I. V. Grigorieva, and A. A. Firsov, *Science* **306**, 666 (2004).
- [11] E. H. Hall, *American Journal of Mathematics* **2**, 287 (1879).
- [12] Y. Zhang, Y.-W. Tan, H. L. Stormer, and P. Kim, *Nature* **438**, 201 (2005).
- [13] K. S. Novoselov, Z. Jiang, Y. Zhang, S. V. Morozov, H. L. Stormer, U. Zeitler, J. C. Maan, G. S. Boebinger, P. Kim, and A. K. Geim, *Science* **315**, 1379 (2007).
- [14] X. Du, I. Skachko, F. Duerr, A. Luican, and E. Y. Andrei, *Nature* **462**, 192 (2009).
- [15] O. Klein, *Zeitschrift für Physik* **53**, 157 (1929).
- [16] A. K. Geim and K. S. Novoselov, *Nature Materials* **6**, 183 (2007).
- [17] A. H. Castro Neto, F. Guinea, N. M. R. Peres, K. S. Novoselov, and A. K. Geim, *Reviews of Modern Physics* **81**, 109 (2009).
- [18] M. I. Katsnelson, K. S. Novoselov, and A. K. Geim, *Nature Physics* **2**, 620 (2006).
- [19] C. Gómez-Navarro, M. Burghard, and K. Kern, *Nano Letters* **8**, 2045 (2008).
- [20] K. S. Novoselov, V. I. Fal'ko, L. Colombo, P. R. Gellert, M. G. Schwab, and K. Kim, *Nature* **490**, 192 (2012).
- [21] A. K. Geim, *Angewandte Chemie International Edition* **50**, 6966 (2011).
- [22] K. S. Novoselov, D. Jiang, F. Schedin, T. J. Booth, V. V. Khotkevich, S. V. Morozov, and A. K. Geim, *Proceedings of the National Academy of Sciences* **102**, 10451 (2005).
- [23] M. Chhowalla, H. S. Shin, G. Eda, L.-J. Li, K. P. Loh, and H. Zhang, *Nature Chemistry* **5**, 263 (2013).
- [24] R. Balog, B. Jørgensen, L. Nilsson, M. Andersen, E. Rienks, M. Bianchi, M. Fanetti, E. Lægsgaard, A. Baraldi, S. Lizzit, Z. Sljivancanin, F. Besenbacher, B. Hammer, T. G. Pedersen, P. Hofmann, and L. Hornekær, *Nature Materials* **9**, 315 (2010).
- [25] M. S. Nevius, M. Conrad, F. Wang, A. Celis, M. N. Nair, A. Taleb-Ibrahimi, A. Tejada, and E. H. Conrad, *Physical Review Letters* **115**, 136802 (2015).

- [26] A. Splendiani, L. Sun, Y. Zhang, T. Li, J. Kim, C.-Y. Chim, G. Galli, and F. Wang, *Nano Letters* **10**, 1271 (2010).
- [27] Z. Y. Zhu, Y. C. Cheng, and U. Schwingenschlögl, *Physical Review B* **84**, 153402 (2011).
- [28] K. F. Mak, C. Lee, J. Hone, J. Shan, and T. F. Heinz, *Physical Review Letters* **105**, 136805 (2010).
- [29] B. Radisavljevic, A. Radenovic, J. Brivio, V. Giacometti, and A. Kis, *Nature Nanotechnology* **6**, 147 (2011).
- [30] D. Krasnozhan, D. Lembke, C. Nyffeler, Y. Leblebici, and A. Kis, *Nano Letters* **14**, 5905 (2014).
- [31] Y.-C. Lin, R. K. Ghosh, R. Addou, N. Lu, S. M. Eichfeld, H. Zhu, M.-Y. Li, X. Peng, M. J. Kim, L.-J. Li, R. M. Wallace, S. Datta, and J. A. Robinson, *Nature Communications* **6**, 7311 (2015).
- [32] R. S. Sundaram, M. Engel, A. Lombardo, R. Krupke, A. C. Ferrari, P. Avouris, and M. Steiner, *Nano Letters* **13**, 1416 (2013).
- [33] M. Bernardi, M. Palumbo, and J. C. Grossman, *Nano Letters* **13**, 3664 (2013).
- [34] V. K. Sangwan, D. Jariwala, I. S. Kim, K.-S. Chen, T. J. Marks, L. J. Lauhon, and M. C. Hersam, *Nature Nanotechnology* **10**, 403 (2015).
- [35] P.-C. Yeh, W. Jin, N. Zaki, D. Zhang, J. T. Liou, J. T. Sadowski, A. Al-Mahboob, J. I. Dadap, I. P. Herman, P. Sutter, and R. M. Osgood, *Physical Review B* **91**, 041407 (2015).
- [36] D. W. Latzke, W. Zhang, A. Suslu, T.-R. Chang, H. Lin, H.-T. Jeng, S. Tongay, J. Wu, A. Bansil, and A. Lanzara, *Physical Review B* **91**, 235202 (2015).
- [37] M. M. Ugeda, A. J. Bradley, Y. Zhang, S. Onishi, Y. Chen, W. Ruan, C. Ojeda-Aristizabal, H. Ryu, M. T. Edmonds, H.-Z. Tsai, A. Riss, S.-K. Mo, D. Lee, A. Zettl, Z. Hussain, Z.-X. Shen, and M. F. Crommie, *Nature Physics* **12**, 92 (2016).
- [38] Thomson Reuters ISI Web of Knowledge, <http://pcs.webofknowledge.com/?Func=Exit>.
- [39] S. Nagata, T. Aochi, T. Abe, S. Ebisu, T. Hagino, Y. Seki, and K. Tsutsumi, *Journal of Physics and Chemistry of Solids* **53**, 1259 (1992).
- [40] I. Guillaamón, H. Suderow, S. Vieira, L. Cario, P. Diener, and P. Rodière, *Physical Review Letters* **101**, 166407 (2008).
- [41] Z. Wang, D. Gresch, A. A. Soluyanov, W. Xie, S. Kushwaha, X. Dai, M. Troyer, R. J. Cava, and B. A. Bernevig, *Physical Review Letters* **117**, 056805 (2016).
- [42] A. A. Soluyanov, D. Gresch, Z. Wang, Q. Wu, M. Troyer, X. Dai, and B. A. Bernevig, *Nature* **527**, 495 (2015).
- [43] M. N. Ali, J. Xiong, S. Flynn, J. Tao, Q. D. Gibson, L. M. Schoop, T. Liang, N. Hal-dolaarachchige, M. Hirschberger, N. P. Ong, and R. J. Cava, *Nature* **514**, 205 (2014).
- [44] I. Pletikosić, M. N. Ali, A. V. Fedorov, R. J. Cava, and T. Valla, *Physical Review Letters* **113**, 216601 (2014).
- [45] D. Xiao, G.-B. Liu, W. Feng, X. Xu, and W. Yao, *Physical Review Letters* **108**, 196802 (2012).
- [46] D. Xiao, M.-C. Chang, and Q. Niu, *Reviews of Modern Physics* **82**, 1959 (2010).
- [47] K. F. Mak, K. L. McGill, J. Park, and P. L. McEuen, *Science* **344**, 1489 (2014).
- [48] X. Xu, W. Yao, D. Xiao, and T. F. Heinz, *Nature Physics* **10**, 343 (2014).

-
- [49] S. Wu, C. Huang, G. Aivazian, J. S. Ross, D. H. Cobden, and X. Xu, *ACS Nano* **7**, 2768 (2013).
- [50] D. Xiao, W. Yao, and Q. Niu, *Physical Review Letters* **99**, 236809 (2007).
- [51] G. Dresselhaus, *Physical Review* **100**, 580 (1955).
- [52] K. F. Mak, K. He, J. Shan, and T. F. Heinz, *Nature Nanotechnology* **7**, 494 (2012).
- [53] A. Kormányos, G. Burkard, M. Gmitra, J. Fabian, V. Zólyomi, N. D. Drummond, and V. Fal'ko, *2D Materials* **2**, 022001 (2015).
- [54] A. Kormányos, V. Zólyomi, N. D. Drummond, P. Rakyta, G. Burkard, and V. I. Fal'ko, *Physical Review B* **88**, 045416 (2013).
- [55] M. Mucha-Kruczyński, O. Tsypliyatyev, A. Grishin, E. McCann, V. I. Fal'ko, A. Bostwick, and E. Rotenberg, *Physical Review B* **77**, 195403 (2008).
- [56] A. Kormányos, V. Zólyomi, N. D. Drummond, and G. Burkard, *Physical Review X* **4**, 011034 (2014).
- [57] D. Ovchinnikov, A. Allain, Y.-S. Huang, D. Dumcenco, and A. Kis, *ACS Nano* **8**, 8174 (2014).
- [58] L. Liu, S. B. Kumar, Y. Ouyang, and J. Guo, *IEEE Transactions on Electron Devices* **58**, 3042 (2011).
- [59] T. Cheiwchanchamnangij and W. R. L. Lambrecht, *Physical Review B* **85**, 205302 (2012).
- [60] T.-R. T. Han, F. Zhou, C. D. Malliakas, P. M. Duxbury, S. D. Mahanti, M. G. Kanatzidis, and C.-Y. Ruan, *Science Advances* **1**, e1400173 (2015).
- [61] J. P. Tidman, O. Singh, A. E. Curzon, and R. F. Frindt, *Philosophical Magazine* **30**, 1191 (2006).
- [62] J. A. Wilson, F. J. Di Salvo, and S. Mahajan, *Physical Review Letters* **32**, 882 (1974).
- [63] M. Johannes, I. Mazin, and C. Howells, *Physical Review B* **73**, 205102 (2006).
- [64] T. M. Rice and G. K. Scott, *Physical Review Letters* **35**, 120 (1975).
- [65] B. Sipoš, A. F. Kusmartseva, A. Akrap, H. Berger, L. Forró, and E. Tutiš, *Nature Materials* **7**, 960 (2008).
- [66] H. Hertz, *Annalen der Physik* **267**, 983 (1887).
- [67] A. Einstein, *Annalen der Physik* **322**, 132 (1905).
- [68] S. Kevan, *Angle-resolved photoemission* (1992).
- [69] S. Hüfner, *Very high resolution photoelectron spectroscopy* (2007).
- [70] S. Hüfner, *Photoelectron spectroscopy* (2013).
- [71] A. Damascelli, *Physica Scripta* **2004**, 61 (2004).
- [72] G. Wertheim, F. Di Salvo, and S. Chiang, *Physics Letters A* **54**, 304 (1975).
- [73] S. Doniach and M. Šunjić, *Journal of Physics C: Solid State Physics* **3**, 285 (1970).
- [74] G. D. Mahan, *Physical Review B* **11**, 4814 (1975).
- [75] H. P. Hughes and J. A. Scarfe, *Physical Review Letters* **74**, 3069 (1995).
- [76] D. A. Shirley, *Physical Review B* **5**, 4709 (1972).
- [77] S. Tougaard, *Surface Science Letters* **139**, A125 (1984).
- [78] S. Hofmann, *Auger- and x-ray photoelectron spectroscopy in materials science* (2013).

- [79] S. Møller, N. Hertel, and J. Nielsen, IPAC12 Proceedings, 1605 (2012).
- [80] S. V. Hoffmann, C. Søndergaard, C. Schultz, Z. Li, and P. Hofmann, Nuclear Instruments and Methods in Physics Research, A **523**, 441 (2004).
- [81] ISA, <http://www.isa.au.dk>.
- [82] Marco Bianchi, <http://marcobianchi.weebly.com/education-projects.html>.
- [83] J. V. Lauritsen, *Atomic scale study of a hydrodesulfurization model catalyst* (2002).
- [84] J. V. Barth, H. Brune, G. Ertl, and R. J. Behm, Physical Review B **42**, 9307 (1990).
- [85] P. Heimann and H. Neddermeyer, Journal of Physics F: Metal Physics **7**, L37 (1977).
- [86] S. LaShell, B. A. McDougall, and E. Jensen, Physical Review Letters **77**, 3419 (1996).
- [87] J. Henk, A. Ernst, and P. Bruno, Physical Review B **68**, 165416 (2003).
- [88] M. Hoesch, M. Muntwiler, V. N. Petrov, M. Hengsberger, L. Patthey, M. Shi, M. Falub, T. Greber, and J. Osterwalder, Physical Review B **69**, 241401 (2004).
- [89] L. Petersen and P. Hedegård, Surface Science **459**, 49 (2000).
- [90] J. Kliewer, R. Berndt, E. V. Chulkov, V. M. Silkin, P. M. Echenique, and S. Crampin, Science **288**, 1399 (2000).
- [91] F. Reinert, G. Nicolay, S. Schmidt, D. Ehm, and S. Hüfner, Physical Review B **63**, 115415 (2001).
- [92] I. A. Nechaev, M. F. Jensen, E. D. L. Rienks, V. M. Silkin, P. M. Echenique, E. V. Chulkov, and P. Hofmann, Physical Review B **80**, 113402 (2009).
- [93] F. Reinert and G. Nicolay, Applied Physics A **78**, 817 (2004).
- [94] P. Borghetti, J. Lobo-Checa, E. Goiri, A. Mugarza, F. Schiller, J. Enrique Ortega, and E. E. Krasovskii, Journal of Physics: Condensed Matter **24**, 395006 (2012).
- [95] W. Chen, V. Madhavan, T. Jamneala, and M. F. Crommie, Physical Review Letters **80**, 1469 (1998).
- [96] L. Bürgi, H. Brune, and K. Kern, Physical Review Letters **89**, 176801 (2002).
- [97] N. Takeuchi, C. T. Chan, and K. M. Ho, Physical Review B **43**, 13899 (1991).
- [98] A. P. Seitsonen, Surface Science **643**, 150 (2016).
- [99] A. R. Sandy, S. G. J. Mochrie, D. M. Zehner, K. G. Huang, and D. Gibbs, Physical Review B **43**, 4667 (1991).
- [100] E. W. Plummer and W. Eberhardt, *Angle-resolved photoemission as a tool for the study of surfaces* (1982).
- [101] P. Zeller and S. Günther, New Journal of Physics **16**, 083028 (2014).
- [102] M. Van Hove, R. Koestner, P. Stair, J. Bibérian, L. Kesmodel, I. Bartoš, and G. Somorjai, Surface Science **103**, 189 (1981).
- [103] L. Bürgi, H. Brune, O. Jeandupeux, and K. Kern, Journal of Electron Spectroscopy and Related Phenomena **109**, 33 (2000).
- [104] L. Bürgi, L. Petersen, H. Brune, and K. Kern, Surface Science **447**, L157 (2000).
- [105] C. Tusche, A. Krasnyuk, and J. Kirschner, Ultramicroscopy **159**, 520 (2015).
- [106] M. H. Berntsen, P. Palmgren, M. Leandersson, A. Hahlin, J. Åhlund, B. Wannberg, M. Månsson, and O. Tjernberg, Review of Scientific Instruments **81**, 035104 (2010).

-
- [107] A. Takayama, *High-resolution spin-resolved photoemission spectrometer and the rashba effect in bismuth thin films* (2015).
- [108] H. Zeng, J. Dai, W. Yao, D. Xiao, and X. Cui, *Nature Nanotechnology* **7**, 490 (2012).
- [109] D. Dumcenco, D. Ovchinnikov, K. Marinov, P. Lazić, M. Gibertini, N. Marzari, O. L. Sanchez, Y.-C. Kung, D. Krasnozhan, M.-W. Chen, S. Bertolazzi, P. Gillet, A. Fontcuberta i Morral, A. Radenovic, and A. Kis, *ACS Nano* **9**, 4611 (2015).
- [110] S. Helveg, J. V. Lauritsen, E. Lægsgaard, I. Stensgaard, J. K. Nørskov, B. S. Clausen, H. Topsøe, and F. Besenbacher, *Physical Review Letters* **84**, 951 (2000).
- [111] S. S. Grønborg, S. Ulstrup, M. Bianchi, M. Dendzik, C. E. Sanders, J. V. Lauritsen, P. Hofmann, and J. A. Miwa, *Langmuir* **31**, 9700 (2015).
- [112] C. E. Sanders, M. Dendzik, A. S. Ngankeu, A. Eich, A. Bruix, M. Bianchi, J. A. Miwa, B. Hammer, A. A. Khajetoorians, and P. Hofmann, *Physical Review B* **94**, 081404 (2016).
- [113] M. Dendzik, M. Michiardi, C. Sanders, M. Bianchi, J. A. Miwa, S. S. Grønborg, J. V. Lauritsen, A. Bruix, B. Hammer, and P. Hofmann, *Physical Review B* **92**, 245442 (2015).
- [114] J. A. Miwa, M. Dendzik, S. S. Grønborg, M. Bianchi, J. V. Lauritsen, P. Hofmann, and S. Ulstrup, *ACS Nano* **9**, 6502 (2015).
- [115] M. M. Biener, J. Biener, R. Schalek, and C. M. Friend, *The Journal of Chemical Physics* **121**, 12010 (2004).
- [116] W. Ling, J. Hamilton, K. Thürmer, G. Thayer, J. de la Figuera, R. Hwang, C. Carter, N. Bartelt, and K. McCarty, *Surface Science* **600**, 1735 (2006).
- [117] A. D. Jewell, H. L. Tierney, and E. C. H. Sykes, *Physical Review B* **82**, 205401 (2010).
- [118] G. E. Poirier, *Chemical Reviews* **97**, 1117 (1997).
- [119] N. Krane, C. Lotze, J. M. Läger, G. Reece, and K. J. Franke, *Nano Letters* **16**, 5163 (2016).
- [120] A. Ramasubramaniam, D. Naveh, and E. Towe, *Physical Review B* **84**, 205325 (2011).
- [121] W. Zhou, X. Zou, S. Najmaei, Z. Liu, Y. Shi, J. Kong, J. Lou, P. M. Ajayan, B. I. Yakobson, and J.-C. Idrobo, *Nano Letters* **13**, 2615 (2013).
- [122] K. Kobayashi and J. Yamauchi, *Physical Review B* **51**, 17085 (1995).
- [123] J. Kibsgaard, Z. Chen, B. N. Reinecke, and T. F. Jaramillo, *Nature Materials* **11**, 963 (2012).
- [124] M. V. Bollinger, J. V. Lauritsen, K. W. Jacobsen, J. K. Nørskov, S. Helveg, and F. Besenbacher, *Physical Review Letters* **87**, 196803 (2001).
- [125] J. Yang, J. Deng, N. Chandrasekhar, and C. Joachim, *Journal of Vacuum Science and Technology B: Microelectronics and Nanometer Structures* **25**, 1694 (2007).
- [126] H.-P. Komsa and A. V. Krashennnikov, *Physical Review B* **86**, 241201 (2012).
- [127] B. Zhu, X. Chen, and X. Cui, *Scientific Reports* **5**, 9218 (2014).
- [128] Y. J. Hong and T. Fukui, *ACS Nano* **5**, 7576 (2011).
- [129] J. Kim, C. Bayram, H. Park, C.-W. Cheng, C. Dimitrakopoulos, J. A. Ott, K. B. Reuter, S. W. Bedell, and D. K. Sadana, *Nature Communications* **5**, 4836 (2014).
- [130] W. Dang, H. Peng, H. Li, P. Wang, and Z. Liu, *Nano Letters* **10**, 2870 (2010).
- [131] Y. Shi, W. Zhou, A.-Y. Lu, W. Fang, Y.-H. Lee, A. L. Hsu, S. M. Kim, K. K. Kim, H. Y. Yang, L.-J. Li, J.-C. Idrobo, and J. Kong, *Nano Letters* **12**, 2784 (2012).

- [132] M.-Y. Lin, C.-E. Chang, C.-H. Wang, C.-F. Su, C. Chen, S.-C. Lee, and S.-Y. Lin, *Applied Physics Letters* **105**, 073501 (2014).
- [133] K. M. McCreary, A. T. Hanbicki, J. T. Robinson, E. Cobas, J. C. Culbertson, A. L. Friedman, G. G. Jernigan, and B. T. Jonker, *Advanced Functional Materials* **24**, 6449 (2014).
- [134] Y.-C. Lin, N. Lu, N. Perea-Lopez, J. Li, Z. Lin, X. Peng, C. H. Lee, C. Sun, L. Calderin, P. N. Browning, M. S. Bresnehan, M. J. Kim, T. S. Mayer, M. Terrones, and J. A. Robinson, *ACS Nano* **8**, 3715 (2014).
- [135] Y.-C. Lin, C.-Y. S. Chang, R. K. Ghosh, J. Li, H. Zhu, R. Addou, B. Diaconescu, T. Ohta, X. Peng, N. Lu, M. J. Kim, J. T. Robinson, R. M. Wallace, T. S. Mayer, S. Datta, L.-J. Li, and J. A. Robinson, *Nano Letters* **14**, 6936 (2014).
- [136] I. Forbeaux, J.-M. Themlin, A. Charrier, F. Thibaudau, and J.-M. Debever, *Applied Surface Science* **162-163**, 406.
- [137] K. V. Emtsev, F. Speck, T. Seyller, L. Ley, and J. D. Riley, *Physical Review B* **77**, 155303 (2008).
- [138] S. L. Wong, H. Huang, Y. Wang, L. Cao, D. Qi, I. Santoso, W. Chen, and A. T. S. Wee, *ACS Nano* **5**, 7662 (2011).
- [139] J. Lauritsen, M. Bollinger, E. Lægsgaard, K. Jacobsen, J. Nørskov, B. Clausen, H. Topsøe, and F. Besenbacher, *Journal of Catalysis* **221**, 510 (2004).
- [140] J. Kibsgaard, J. V. Lauritsen, E. Lægsgaard, B. S. Clausen, H. Topsøe, and F. Besenbacher, *Journal of the American Chemical Society* **128**, 13950 (2006).
- [141] J. Kibsgaard, A. Tuxen, M. Levisen, E. Lægsgaard, S. Gemming, G. Seifert, J. V. Lauritsen, and F. Besenbacher, *Nano Letters* **8**, 3928 (2008).
- [142] D. Le, D. Sun, W. Lu, M. Aminpour, C. Wang, Q. Ma, T. S. Rahman, and L. Bartels, *Surface Science* **611**, 1 (2013).
- [143] Y. Zhang, T.-R. Chang, B. Zhou, Y.-T. Cui, H. Yan, Z. Liu, F. Schmitt, J. Lee, R. Moore, Y. Chen, H. Lin, H.-T. Jeng, S.-K. Mo, Z. Hussain, A. Bansil, and Z.-X. Shen, *Nature Nanotechnology* **9**, 111 (2014).
- [144] M. M. Ugeda, A. J. Bradley, S.-F. Shi, F. H. da Jornada, Y. Zhang, D. Y. Qiu, W. Ruan, S.-K. Mo, Z. Hussain, Z.-X. Shen, F. Wang, S. G. Louie, and M. F. Crommie, *Nature Materials* **13**, 1091 (2014).
- [145] H. G. Führtbauer, A. K. Tuxen, P. G. Moses, H. Topsøe, F. Besenbacher, and J. V. Lauritsen, *Physical Chemistry Chemical Physics* **15**, 15971 (2013).
- [146] W. Schutte, J. De Boer, and F. Jellinek, *Journal of Solid State Chemistry* **70**, 207 (1987).
- [147] R. G. Dickinson and L. Pauling, *Journal of the American Chemical Society* **45**, 1466 (1923).
- [148] G. Rovida and F. Pratesi, *Surface Science* **104**, 609 (1981).
- [149] K. Schwaha, N. Spencer, and R. Lambert, *Surface Science* **81**, 273 (1979).
- [150] M. Yu, D. P. Woodruff, C. J. Satterley, R. G. Jones, and V. R. Dhanak, *The Journal of Physical Chemistry C* **111**, 3152 (2007).
- [151] S. M. Russell, Y. Kim, D.-J. Liu, J. W. Evans, and P. A. Thiel, *The Journal of Chemical Physics* **138**, 071101 (2013).
- [152] M. Farmanbar and G. Brocks, *Physical Review B* **91**, 161304 (2015).

-
- [153] C. Gong, L. Colombo, R. M. Wallace, and K. Cho, *Nano Letters* **14**, 1714 (2014).
- [154] F. Rossel, M. Pivetta, F. Patthey, E. Čavar, A. P. Seitsonen, and W.-D. Schneider, *Physical Review B* **84**, 075426 (2011).
- [155] B. Amin, T. P. Kaloni, and U. Schwingenschlögl, *RSC Advances* **4**, 34561 (2014).
- [156] S. Ulstrup, M. Schüler, M. Bianchi, F. Fromm, C. Raidel, T. Seyller, T. Wehling, and P. Hofmann, *Physical Review B* **94**, 081403 (2016).
- [157] J. Wilson and A. Yoffe, *Advances in Physics* **18**, 193 (1969).
- [158] P. J. Rous, J. B. Pendry, D. K. Saldin, K. Heinz, K. Müller, and N. Bickel, *Physical Review Letters* **57**, 2951 (1986).
- [159] W. Jin, P.-C. Yeh, N. Zaki, D. Zhang, J. T. Sadowski, A. Al-Mahboob, A. M. van der Zande, D. A. Chenet, J. I. Dadap, I. P. Herman, P. Sutter, J. Hone, and R. M. Osgood, *Physical Review Letters* **111**, 106801 (2013).
- [160] N. Alidoust, G. Bian, S.-Y. Xu, R. Sankar, M. Neupane, C. Liu, I. Belopolski, D.-X. Qu, J. D. Denlinger, F.-C. Chou, and M. Z. Hasan, *Nature Communications* **5**, 4673 (2014).
- [161] S. LaShell, B. A. McDougall, and E. Jensen, *Physical Review Letters* **77**, 3419 (1996).
- [162] E. Cappelluti, R. Roldán, J. A. Silva-Guillén, P. Ordejón, and F. Guinea, *Physical Review B* **88**, 075409 (2013).
- [163] T. Böker, R. Severin, A. Müller, C. Janowitz, R. Manzke, D. Voß, P. Krüger, A. Mazur, and J. Pollmann, *Physical Review B* **64**, 235305 (2001).
- [164] I. Pletikosić, M. Kralj, P. Pervan, R. Brako, J. Coraux, A. T. N'Diaye, C. Busse, and T. Michely, *Physical Review Letters* **102**, 056808 (2009).
- [165] A. Bostwick, T. Ohta, T. Seyller, K. Horn, and E. Rotenberg, *Nature Physics* **3**, 36 (2006).
- [166] J. C. Y. Teo, L. Fu, and C. L. Kane, *Physical Review B* **78**, 045426 (2008).
- [167] L. Sun, J. Yan, D. Zhan, L. Liu, H. Hu, H. Li, B. K. Tay, J.-L. Kuo, C.-C. Huang, D. W. Hewak, P. S. Lee, and Z. X. Shen, *Physical Review Letters* **111**, 126801 (2013).
- [168] D. Y. Qiu, F. H. da Jornada, and S. G. Louie, *Physical Review Letters* **111**, 216805 (2013).
- [169] C. D. Spataru and F. Léonard, *Chemical Physics* **413**, 81 (2013).
- [170] Y. Liang and L. Yang, *Physical Review Letters* **114**, 063001 (2015).
- [171] A. Grubišić Čabo, J. A. Miwa, S. S. Grønberg, J. M. Riley, J. C. Johannsen, C. Cacho, O. Alexander, R. T. Chapman, E. Springate, M. Grioni, J. V. Lauritsen, P. D. C. King, P. Hofmann, and S. Ulstrup, *Nano Letters* **15**, 5883 (2015).
- [172] A. Bruix, J. A. Miwa, N. Hauptmann, D. Wegner, S. Ulstrup, S. S. Grønberg, C. E. Sanders, M. Dendzik, A. Grubišić Čabo, M. Bianchi, J. V. Lauritsen, A. A. Khajetoorians, B. Hammer, and P. Hofmann, *Physical Review B* **93**, 165422 (2016).
- [173] A. R. Beal, J. C. Knights, and W. Y. Liang, *Journal of Physics C: Solid State Physics* **5**, 3540 (1972).
- [174] A. R. Klots, A. K. M. Newaz, B. Wang, D. Prasai, H. Krzyzanowska, J. Lin, D. Caudel, N. J. Ghimire, J. Yan, B. L. Ivanov, K. A. Velizhanin, A. Burger, D. G. Mandrus, N. H. Tolk, S. T. Pantelides, and K. I. Bolotin, *Scientific Reports* **4**, 6608.
- [175] T.-C. Chiang, *Surface Science Reports* **39**, 181 (2000).
- [176] G. Kresse and J. Hafner, *Physical Review B* **47**, 558 (1993).

- [177] G. Kresse and J. Furthmüller, *Physical Review B* **54**, 11169 (1996).
- [178] G. Kresse and J. Furthmüller, *Computational Materials Science* **6**, 15 (1996).
- [179] P. E. Blöchl, *Physical Review B* **50**, 17953 (1994).
- [180] J. P. Perdew, K. Burke, and M. Ernzerhof, *Physical Review Letters* **77**, 3865 (1996).
- [181] S. G. Sørensen, H. G. Füchtbauer, A. K. Tuxen, A. S. Walton, and J. V. Lauritsen, *ACS Nano* **8**, 6788 (2014).
- [182] J. Kang, W. Liu, D. Sarkar, D. Jena, and K. Banerjee, *Physical Review X* **4**, 031005 (2014).
- [183] M. Endlich, A. Molina-Sánchez, L. Wirtz, and J. Kröger, *Physical Review B* **88**, 205403 (2013).
- [184] P. V. C. Medeiros, S. Stafström, and J. Björk, *Physical Review B* **89**, 041407 (2014).
- [185] P. V. C. Medeiros, S. S. Tsirkin, S. Stafström, and J. Björk, *Physical Review B* **91**, 041116 (2015).
- [186] F. Forster, A. Bendounan, F. Reinert, V. Grigoryan, and M. Springborg, *Surface Science* **601**, 5595 (2007).
- [187] F. Mazzola, J. W. Wells, R. Yakimova, S. Ulstrup, J. A. Miwa, R. Balog, M. Bianchi, M. Leandersson, J. Adell, P. Hofmann, and T. Balasubramanian, *Physical Review Letters* **111**, 216806 (2013).
- [188] X. Fan, D. J. Singh, and W. Zheng, *The Journal of Physical Chemistry Letters* **7**, 2175 (2016).
- [189] T. Komesu, D. Le, Q. Ma, E. F. Schwier, Y. Kojima, M. Zheng, H. Iwasawa, K. Shimada, M. Taniguchi, L. Bartels, T. S. Rahman, and P. A. Dowben, *Journal of Physics: Condensed Matter* **26**, 455501 (2014).
- [190] D. Pierucci, H. Henck, J. Avila, A. Balan, C. H. Naylor, G. Patriarche, Y. J. Dappe, M. G. Silly, F. Sirotti, A. T. C. Johnson, M. C. Asensio, and A. Ouerghi, *Nano Letters* **16**, 4054 (2016).
- [191] Q. H. Wang, K. Kalantar-Zadeh, A. Kis, J. N. Coleman, and M. S. Strano, *Nature Nanotechnology* **7**, 699 (2012).
- [192] T. Ohta, A. Bostwick, J. L. McChesney, T. Seyller, K. Horn, and E. Rotenberg, *Physical Review Letters* **98**, 206802 (2007).
- [193] P. Young, *Journal of Physics D: Applied Physics* **1**, 936 (1968).
- [194] A. Klein, S. Tiefenbacher, V. Eyert, C. Pettenkofer, and W. Jaegermann, *Physical Review B* **64**, 205416 (2001).
- [195] S. Tougaard, *Surface and Interface Analysis* **11**, 453 (1988).
- [196] P. Heimann, J. F. van der Veen, and D. E. Eastman, *Solid State Communications* **38**, 595 (1981).
- [197] A. P. Shpak, A. M. Korduban, L. M. Kulikov, T. V. Kryshchuk, N. B. Konig, and V. O. Kandyba, *Journal of Electron Spectroscopy and Related Phenomena* **181**, 234 (2010).
- [198] M. Cattelan, B. Markman, G. Lucchini, P. K. Das, I. Vobornik, J. A. Robinson, S. Agnoli, and G. Granozzi, *Chemistry of Materials* **27**, 4105 (2015).
- [199] A. Bruix, H. G. Füchtbauer, A. K. Tuxen, A. S. Walton, M. Andersen, S. Porsgaard, F. Besenbacher, B. Hammer, and J. V. Lauritsen, *ACS Nano* **9**, 9322 (2015).

-
- [200] A. Ramasubramaniam, *Physical Review B* **86**, 115409 (2012).
- [201] W. Zhao, Z. Ghorannevis, L. Chu, M. Toh, C. Kloc, P.-H. Tan, and G. Eda, *ACS Nano* **7**, 791 (2013).
- [202] D. Le, A. Barinov, E. Preciado, M. Isarraraz, I. Tanabe, T. Komesu, C. Troha, L. Bartels, T. S. Rahman, and P. A. Dowben, *Journal of Physics: Condensed Matter* **27**, 182201 (2015).
- [203] E. L. Shirley, L. J. Terminello, A. Santoni, and F. J. Himpsel, *Physical Review B* **51**, 13614 (1995).
- [204] M. Mucha-Kruczyński, O. Tsyplyatyev, A. Grishin, E. McCann, V. I. Fal'ko, A. Bostwick, and E. Rotenberg, *Physical Review B* **77**, 195403 (2008).
- [205] H. Liu, A. T. Neal, and P. D. Ye, *ACS Nano* **6**, 8563 (2012).
- [206] S. Ulstrup, A. G. Čabo, D. Biswas, J. M. Riley, M. Dendzik, C. E. Sanders, M. Bianchi, C. Cacho, D. Matselyukh, R. T. Chapman, E. Springate, P. D. C. King, J. A. Miwa, and P. Hofmann, arXiv:1608.06023 (2016).
- [207] V. Heine, *Physical Review* **138**, A1689 (1965).
- [208] S. G. Louie and M. L. Cohen, *Physical Review Letters* **35**, 866 (1975).
- [209] H. P. Hughes and J. A. Scarfe, *Journal of Physics: Condensed Matter* **8**, 1421 (1996).
- [210] H. P. Hughes and J. A. Scarfe, *Journal of Physics: Condensed Matter* **8**, 1439 (1996).
- [211] K. Rossnagel, *Journal of Physics: Condensed Matter* **23**, 213001 (2011).
- [212] P. Chen, Y. H. Chan, X. Y. Fang, Y. Zhang, M. Y. Chou, S. K. Mo, Z. Hussain, A. V. Fedorov, and T. C. Chiang, *Nature Communications* **6**, 8943 (2015).
- [213] K. Sugawara, Y. Nakata, R. Shimizu, P. Han, T. Hitosugi, T. Sato, and T. Takahashi, *ACS Nano* **10**, 1341 (2016).
- [214] X. Xi, L. Zhao, Z. Wang, H. Berger, L. Forró, J. Shan, and K. F. Mak, *Nature Nanotechnology* **10**, 765 (2015).
- [215] R. L. Barnett, A. Polkovnikov, E. Demler, W.-G. Yin, and W. Ku, *Physical Review Letters* **96**, 026406 (2006).
- [216] P. Garoche, P. Manuel, J. J. Veyssié, and P. Molinié, *Journal of Low Temperature Physics* **30**, 323 (1978).
- [217] I. Guillamón, H. Suderow, J. G. Rodrigo, S. Vieira, P. Rodière, L. Cario, E. Navarro-Moratalla, C. Martí-Gastaldo, and E. Coronado, *New Journal of Physics* **13**, 103020 (2011).
- [218] E. Navarro-Moratalla, J. O. Island, S. Mañas-Valero, E. Pinilla-Cienfuegos, A. Castellanos-Gomez, J. Quereda, G. Rubio-Bollinger, L. Chirolli, J. A. Silva-Guillén, N. Agraït, G. A. Steele, F. Guinea, H. S. J. van der Zant, and E. Coronado, *Nature Communications* **7**, 11043 (2016).
- [219] J. A. Galvis, L. Chirolli, I. Guillamón, S. Vieira, E. Navarro-Moratalla, E. Coronado, H. Suderow, and F. Guinea, *Physical Review B* **89**, 224512 (2014).
- [220] M. Calandra, I. I. Mazin, and F. Mauri, *Physical Review B* **80**, 241108 (2009).
- [221] A. H. Castro Neto, *Physical Review Letters* **86**, 4382 (2001).
- [222] K. Rossnagel, O. Seifarth, L. Kipp, M. Skibowski, D. Voß, P. Krüger, A. Mazur, and J. Pollmann, *Physical Review B* **64**, 235119 (2001).

-
- [223] R. Friend and A. Yoffe, *Advances in Physics* **36**, 1 (1987).
- [224] T. O. Wehling, arXiv:1609.00220 (2016).
- [225] A. Soumyanarayanan, M. M. Yee, Y. He, J. van Wezel, D. J. Rahn, K. Rossnagel, E. W. Hudson, M. R. Norman, and J. E. Hoffman, *Proceedings of the National Academy of Sciences* **110**, 1623 (2013).
- [226] Y. Ge and A. Y. Liu, *Physical Review B* **86**, 104101 (2012).